Cell Stem Cell

Organoid modeling of Zika and Herpes Simplex virus 1 infections reveals virus-specific responses leading to microcephaly

--Manuscript Draft--

Manuscript Number:	CELL-STEM-CELL-D-20-00372R3
Full Title:	Organoid modeling of Zika and Herpes Simplex virus 1 infections reveals virus-specific responses leading to microcephaly
Article Type:	Research Article
Keywords:	brain organoids, microcephaly, human neural progenitors, Zika virus, Herpes Simplex Virus, interferon, interferon stimulated genes (ISG), innate immune response
Corresponding Author:	Juergen Knoblich IMBA Vienna, AUSTRIA
First Author:	Veronica Krenn
Order of Authors:	Veronica Krenn
	Camilla Bosone
	Thomas Rainer Burkard
	Julia Spanier
	Ulrich Kalinke
	Arianna Calistri
	Cristiano Salata
	Raissa Rilo Christoff
	Patricia Pestana Garcez
	Ali Mirazimi
	Juergen Knoblich
Abstract:	Viral infections in early pregnancy are a major cause of microcephaly. However, how distinct viruses impair human brain development remains poorly understood. Here we use human brain organoids to study the mechanisms underlying microcephaly caused by Zika Virus (ZIKV) and Herpes Simplex Virus (HSV-1). We find that both viruses efficiently replicate in brain organoids and attenuate their growth by causing cell death. However, transcriptional profiling reveals that ZIKV and HSV-1 elicit distinct cellular responses and HSV-1 uniquely impairs neuroepithelial identity. Furthermore, we demonstrate that while both viruses fail to potently induce the type I interferon system, the organoid defects caused by their infection can be rescued by distinct type I interferons. These phenotypes are not seen in 2D cultures, highlighting the superiority of brain organoids in modelling viral infections. Together, these results uncover virus-specific mechanisms and complex cellular immune defenses associated with virus-induced microcephaly.
Additional Information:	
Question	**Response**
Datasets Does your manuscript report new large-scale datasets?	Yes
To evaluate your manuscript, reviewers must have free access to your large-scale datasets without compromising their anonymity. Please provide access	Access information had been already provided to the reviewers during the revision process. Datasets will become publicly available upon acceptance of the manuscript.

Organoid modeling of Zika and Herpes Simplex virus 1 infections reveals virus-specific responses leading to microcephaly

Veronica Krenn[1], Camilla Bosone[1], Thomas Rainer Burkard[1], Julia Spanier[2], Ulrich Kalinke[2,3], Arianna Calistri[4], Cristiano Salata[4], Raissa Rilo Christoff[5], Patricia Pestana Garcez[5], Ali Mirazimi[6,7] and Jürgen Arthur Knoblich[1,8,9] *

[1]Institute of Molecular Biotechnology (IMBA), Vienna BioCenter (VBC) Vienna, 1030, Austria
[2]Institute for Experimental Infection Research, TWINCORE, Centre for Experimental and Clinical Infection Research, a joint venture between the Helmholtz Centre for Infection Research, Braunschweig, and the Hanover Medical School, Hanover, 30625, Germany
[3]Cluster of Excellence - Resolving Infection Susceptibility (RESIST), Hanover Medical School, 30625 Hanover, Germany
[4]Department of Molecular Medicine, University of Padua, Padua, 35121, Italy
[5]Institute of Biomedical Sciences, Federal University of Rio de Janeiro, Rio de Janeiro, 21941-901, Brazil
[6]Department of Laboratory Medicine (LABMED), Karolinska Institute, Stockholm, 17177, Sweden
[7]National Veterinary Institute, Uppsala, 75189, Sweden
[8] Medical University of Vienna, Vienna BioCenter (VBC), 1030 Vienna, Austria
[9] Lead contact
*Correspondence to: juergen.knoblich@imba.oeaw.ac.at

SUMMARY

Viral infections in early pregnancy are a major cause of microcephaly. However, how distinct viruses impair human brain development remains poorly understood. Here we use human brain organoids to study the mechanisms underlying microcephaly caused by Zika Virus (ZIKV) and Herpes Simplex Virus (HSV-1). We find that both viruses efficiently replicate in brain organoids and attenuate their growth by causing cell death. However, transcriptional profiling reveals that ZIKV and HSV-1 elicit distinct cellular responses and HSV-1 uniquely impairs neuroepithelial identity. Furthermore, we demonstrate that while both viruses fail to potently induce the type I interferon system, the organoid defects caused by their infection can be rescued by distinct type I interferons. These phenotypes are not seen in 2D cultures, highlighting the superiority of brain organoids in modeling viral infections. Together, these results uncover virus-specific mechanisms and complex cellular immune defenses associated with virus-induced microcephaly.

INTRODUCTION

Viral infections during pregnancy are a major cause of fetal brain malformations. The transmission of infectious agents from mother to fetus can be devastating for fetal brain development (Bale and Murph, 1992; Brasil et al., 2016; Marquez et al., 2011). Infections account for up to 50% of cases of congenital microcephaly (Herber et al., 2019; Mlakar et al., 2016) and those occurring in the first trimester of pregnancy are typically associated with more severe outcomes (Coyne and Lazear, 2016). Despite these overlapping phenotypes, congenital infections are caused by distinct pathogens collectively referred to as TORCH and include *T*oxoplasma gondii, *O*ther, *R*ubella, Human *C*ytomegalovirus (HCMV), *H*erpes Simplex Viruses 1 and 2 (HSV-1 and HSV-2), and Zika virus (ZIKV) (Schwartz, 2017). HCMV and HSV are the more common causes of newborn morbidity worldwide (Looker et al., 2017; Marsico and Kimberlin, 2017) and the newly emerged ZIKV remains a threat for pregnant women ("Zika: the continuing threat.," 2019).

Yet, whether TORCH pathogens alter fetal brain development via similar mechanisms is unclear. Mechanistic understanding has been hampered by the lack of accurate models for individual TORCH infections. Although rodents can model in part microcephaly caused by ZIKV and CMV (C. Li et al., 2016; R. Y. Li and Tsutsui, 2000), they are not the natural hosts and do not faithfully recapitulate TORCH neuropathology (Cheeran et al., 2009; Ming et al., 2016). Human brain organoid systems derived from human pluripotent stem cell (hPSC) are emerging as human three-dimensional (3D) culture platforms for the study of viral infections and their impact on human neurodevelopment (J. Kim et al., 2019). Brain organoids recapitulate the cell composition and the 3D environment of the embryonic human brain (Di Lullo and Kriegstein, 2017; Lancaster et al., 2013), thus overcoming a major limitation of human two-dimensional (2D) culture systems (Baker and Chen, 2012; Duval et al., 2017). Organoid models are widely used to recapitulate the structural defects, cell depletion and molecular signatures associated with ZIKV-induced microcephaly (Cugola et al., 2016; Gabriel et al., 2017; Garcez et al., 2016; Qian et al., 2016; M. Watanabe et al., 2017) as well as to model part of the neuropathological defects caused by HCMV and HSV-1 (Brown et al., 2019; Qiao et al., 2020; Sison et al., 2019; Sun et al., 2020). However, a comparative analysis of organoid models of TORCH-induced microcephaly is lacking.

One potential common underlying mechanisms of TORCH-induced microcephaly is the activation of innate immune response and its detrimental effects on fetal brain development (Gottfried et al., 2015; Y. Watanabe et al., 2010). In particular, the activation of cytokines called type I interferons (IFN-I), which include several α species (IFNα) and one β species (IFNβ), upon infection is required to induce an array of antiviral effectors referred to as interferon-stimulated

genes (ISGs) that can restrict viral spreading but also promote cell death (Schneider et al., 2014). Several studies using human 2D and 3D neural cultures have reported the upregulation of IFN-I, ISGs and immune signatures in response to ZIKV infection (Dang et al., 2016; Ferraris et al., 2019; Hanners et al., 2016; C. Li et al., 2017; Lima et al., 2019; Liu et al., 2019; Simonin et al., 2016; M. Watanabe et al., 2017; Zhang et al., 2016). However, the magnitude of this response varies substantially across studies. Furthermore, the function of this response in the pathogenesis of ZIKV infection remains debated, as evidence supporting both a neuroprotective function of IFN-I (C. Li et al., 2017; Lin et al., 2019) and a detrimental neuroinflammatory effect (Dang et al., 2016; Liu et al., 2019) exist. While these discrepancies are in part due to changes in cell differentiation stages and viral strains (Ferraris et al., 2019; Simonin et al., 2016), whether differences between 2D vs 3D culture systems and/or changes in cell type composition contribute to the magnitude and the function of the innate immune response remains unclear. Finally, little is known about the activation of the antiviral response in other human models of TORCH-induced microcephaly and thus a unifying view of the role of the innate immune response is missing.

Here we used human brain organoids to reproduce the microcephaly-like phenotype caused by multiple TORCH viruses, including ZIKV, HCMV and HSV-1, which differ in their viral genome structure, size and mode of replication (Table S1). We show that these organoid models exhibit major differences in their structure, transcriptional profiles, the engagement of the IFN-I system and sensitivity to IFN-I. These results argue for the existence of unique pathogenic mechanisms and a neuroprotective role of IFN-I responses underlying virus-induced microcephaly.

RESULTS

ZIKV and HSV-1 infections impair the growth of early-stage brain organoids

To compare the effects of distinct TORCH viruses on the early stages of human brain development, we generated brain organoids using our previously established protocol (Lancaster et al., 2013) and exposed them to a virus inoculum for 24 hours. We focused on day 10 organoids, an early organoid stage that expresses the neuroectodermal markers Nestin and Pax6 (Figure S1A-B) and is highly susceptible to viral infection (Dang et al., 2016; Gabriel et al., 2017).

We first exposed brain organoids to ZIKV and after inoculum removal, organoids were examined at 4, 8 and 12 days post-infection (dpi). While MOCK-treated organoids grew over time, ZIKV-exposed organoids exhibited a time-dependent growth attenuation and were significantly smaller at 12 dpi (Figure 1A-B, Table S2). Concomitantly, we observed increasing expression of

ZIKV viral RNA (vRNA) and the release of infectious ZIKV particles at 4 dpi and 12 dpi (Figure 1C-D), indicating a productive infection. Staining for the Zika virus antigen (ZIKVA) and the human neural progenitor cell (hNPC) marker Sox1 revealed foci of infection at 4 dpi (Figure 1E), confirming hNPCs as the main cellular targets of ZIKV infection. As a microcephaly phenotype can be described at the tissue level by a cell depletion phenotype, we analyzed hNPC abundance by measuring the area of ventricular zone (VZ)-like structures where hNPCs reside. At 12 dpi, while MOCK-treated organoids showed the typical organization of VZ-like structures, ZIKV-infected organoids contained fewer and smaller VZ-like regions (Figure 1F-G). Furthermore, analysis of apoptosis at 12 dpi by staining for the apoptotic marker cleaved caspase 3 (CC3) showed an increase in ZIKV-infected cultures, both in ZIKVA-positive and negative cells (Figure S1C-E). As hNPC depletion can result in lumen size changes, we also measured the lumen area and found it reduced in ZIKV-infected organoids (Figure S1F). These findings are in line with the ability of ZIKV to attenuate organoid growth and cause hNPC depletion (Cugola et al., 2016; Gabriel et al., 2017; Garcez et al., 2016; Qian et al., 2016; M. Watanabe et al., 2017) and thus validate our infection paradigm for the study of virus-induced microcephaly.

To study the effects of other TORCH viruses, we exposed organoids to HCMV virus expressing the mNeonGreen fluorescent reporter (HCMV-mNG, (Kasmapour et al., 2018) and to another Herpesvirus, HSV-1. We observed mNeonGreen fluorescence in HCMV-exposed organoids at 4 dpi and in a minority of Sox1+ cells after immunostaining (Figure S1G-I). However, HCMV infection remained limited to small clusters of cells at 12 dpi and did not attenuate organoid growth (Figure S1G-K). These observations indicate that HCMV does not replicate efficiently and does not cause a microcephaly-like phenotype in early-stage organoids. In contrast to this, organoids exposed to HSV-1 disintegrated at 8 dpi (Figure S1L-M), uncovering the destructive nature of HSV-1 infection. Organoids exposed to a lower dose of HSV-1 still showed impaired growth at 8 dpi (Figure 1H-I, Table S2) but preserved tissue integrity to a certain extent. We observed productive HSV-1 infection at this lower dose, as evidenced by time-dependent expression of the HSV-1 thymidine kinase (TK) gene and the production of infectious HSV-1 particles (Figure 1J-K). As TK expression at 4 dpi was low and variable, HSV-1 tropism at 4 dpi was analyzed in organoids exposed to the higher HSV-1 dose. This revealed infection of Sox1+ hNPCs and the typical chromatin marginalization to the nuclear periphery caused by HSV-1 replication (Aho et al., 2017) (Figure 1L-M). Immunostaining of tissues infected with low HSV-1 dose revealed a disrupted cytoarchitecture characterized by fewer and smaller VZ-like regions at 8 dpi (Figure 1N-O). Moreover, analysis of the fraction of apoptotic cells showed an increase in HSV-1-infected cultures at 8 dpi compared to MOCK-treated organoids and their accumulation in

the lumen (Figure S1N-O). Unlike ZIKV, lumens of HSV-1-infected organoids appeared enlarged (Figure S1P), likely as a result of accumulation of apoptotic cells. Most apoptotic cells (92%) were negative for the expression of the immediate-early viral protein ICP4 (Figure S1Q-R), suggesting induction of apoptosis in bystander cells and/or abortively infected cells (Drayman et al., 2019). Together, these results indicate that ZIKV and HSV-1, but not HCMV, efficiently infect early-stage brain organoids and reduce their growth, thus mimicking ZIKV- and HSV-1-associated microcephaly.

ZIKV and HSV-1 infections elicit different transcriptional signatures

To investigate the molecular signatures underlying the different organoid growth defects, we analyzed the transcriptional profiles of ZIKV- and HSV-1-infected cultures by RNA-sequencing. We confirmed high expression of neural progenitor genes in these datasets (Figure S2A) and focused on the transcriptional changes at the late time points, as very few genes were deregulated at 4 dpi (Figure 2A-B), an early infection stage that is not associated with major structural defects (Figure 1). We identified 531 and 423 differentially expressed genes (DEGs) in ZIKV- and HSV-1-infected cultures in respect of their MOCK counterparts. Many DEGs in ZIKV-infected cultures were downregulated and involved in cell cycle and cell division (Figure 2C), while almost all DEGs found in HSV-1-infected cultures were upregulated (Figure 2B). Overlap between the two datasets was limited, since only 4.6% of DEGs were shared (Figure 2D).

GO-term analysis on genes upregulated in ZIKV-infected cultures revealed enrichment for antiviral defense pathways, response to interferon (IFN), stress or stimuli (Figure 2E). Furthermore, promoters of upregulated genes were enriched in binding sites for transcription factors involved in immune responses (IRF7/9 and STAT1/2) and in the unfolded protein response (UPR, *DDIT3* and *ATF3)* (Figure 2F). Genes implicated in antiviral defense (Schneider et al., 2014) and UPR were the most upregulated at 12 dpi (Figure 2G, Table S3) and some were found upregulated already at 4 dpi (Figure S2B), confirming the activation of immune and stress-related signatures in ZIKV-infected cultures. In contrast, GO-term analysis on HSV-1-infected signatures revealed enrichment in the regulation of developmental and cellular processes, as well as cell death-related pathways (Figure 2H). Promoters of HSV-1-upregulated genes were enriched in binding sites of key regulators of proliferation, differentiation, apoptosis and transformation, including members of the transcription factor complex AP-1 (*FOS*, *FOSB*, *JUN* and *JUNB*) (Hess et al., 2004), *NR4A3* and *NFIL3* (Herring et al., 2019; Keniry et al., 2014), the neural crest regulator *CSRNP1* (Simões-Costa and Bronner, 2015), the epithelial-mesenchymal transition (EMT) inducer *SNAI1* (Carver et al., 2001) and stress response genes (*DDIT3* and *ATF3)* (Figure

2I). Consistent with this, regulators of cell proliferation, apoptosis and stress response were upregulated in HSV-1-infected cultures (Figure 2J, Table S3). The most upregulated genes also included genes implicated in neural, neural crest and mesenchymal development and key regulators of lymphocyte and erythrocyte function (Figure 2J, Table S3). We confirmed increased expression of the EMT regulator Snai1 in HSV-1-infected cultures by immunostaining (Figure S2C). These results point towards the activation of multiple non-neural pathways in HSV-1-infected cultures.

We hypothesized that this could compromise the neural identity of brain organoids. Thus, we examined neuroepithelial polarity in infected organoids by immunostaining for N-cadherin, which is typically enriched at the apical side in cells surrounding the lumen in MOCK-treated organoids (Figure 2K-L) (Kadowaki et al., 2007). Strikingly, N-cadherin accumulation was lost in HSV-1-infected cultures but not in ZIKV-infected organoids (Figure 2K-L). Apical accumulation of N-cadherin was reduced in HSV-1-infected hNPCs (Figure 2M), suggesting a cell-autonomous effect. Loss of N-cadherin mainly reflected changes in its localization or protein expression, as its mRNA abundance was not severely reduced in infected organoids (Figure S2D). Furthermore, we observed decreased Sox1 protein intensity in HSV-1-infected organoids (Figure S2E), confirming impaired hNPC identity. We observed similar defects also in later-stage organoids infected with HSV-1 (Figure S2F-N), demonstrating the ability of HSV-1 to alter differentiation in more fate-restricted cells. Together, these results indicate that HSV-1 specifically activates alternative non-neural developmental programs and disrupts the neuroepithelial integrity of brain organoids, while ZIKV infection triggers antiviral and stress-related signatures but maintains cytoarchitecture.

ZIKV and HSV-1 infections differentially engage the IFN-I system

We next explored the mechanisms underlying the differential engagement of antiviral defense pathways by ZIKV and HSV-1 by examining the upregulated signatures from the RNA-sequencing data. Cluster analysis of genes upregulated in ZIKV-infected cultures revealed the presence of a highly connected cluster of genes enriched in the interferon-sensitive responsive element (ISRE) in their promoters (Figure 3A-B) and thus mapped to the ISG family (Schneider et al., 2014), in line with a previous study (Liu et al., 2019). Such a signature was not prominent in HSV-1-infected cultures (Figure 3C) and we confirmed the poor activation of ISGs by HSV-1 also at early time points by RT-qPCR analysis (Figure S3A-B). As ISGs are potently induced by IFN-I (Schneider et al., 2014), we measured production of all IFNα species and IFNβ in supernatants from ZIKV and HSV-1-infected organoids by ELISA assay. We detected a modest

(but non-significant) increase of IFNβ specifically in the supernatants from ZIKV-infected cultures, while IFNα abundance was unchanged (Figure 3D-E). This analysis indicates the differential activation of ISGs and IFN-I in ZIKV and HSV-1-infected cultures.

To simultaneously measure IFN-I and ISG expression at single-cell level and with spatial resolution in infected brain organoids, we built a dual fluorescent reporter system. We engineered hPSCs to carry a GFP cassette driven by the *IFNB1* promoter (*IFN>GFP*) and a tdTomato cassette driven by the ISRE motif (*ISRE>tdT*) (Figure 3F). Immunostaining and flow cytometry analysis confirmed low basal expression of both reporters in control organoids and high *ISRE>tdT* expression in response to exogenous IFN-I (Figure S3C-D). To test the functionality of these reporters, we analyzed GFP and tdTomato expression by immunostaining in organoids stimulated with poly(I:C), a synthetic analog of double-stranded RNA (dsRNA) that acts as a potent IFN-I inducer in human NPCs (Lin et al., 2019). Consistent with induction, we detected high IFN>GFP signals and high *ISRE>tdT* expression (Figure 3G-J). However, this occurred only in 0.14% and 46% of the cells respectively, fractions that were smaller to those measured in human lung epithelial A549 cells engineered with the same reporter system (3.6% and 91% respectively; Figure S3E-G). These results validate the functionality the dual reporter systems and reveal a high degree of stochasticity of *IFNB1* expression (Zhao et al., 2012) in brain organoids. We next analyzed reporter expression in response to viral infections by immunostaining. In tissues infected with ZIKV, we detected high *IFN>GFP* signals in very few cells (0.11%), indicating *IFNB1* expression in a rare population of cells, and high *ISRE>tdT* expression in 30% of the cells (Figure 3K-N), consistent with ISG induction. Spatial analysis of reporter expression in ZIKV-infected organoids revealed that *ISRE>tdT*-expressing cells, which co-expressed the neural progenitor marker Sox1 (Figure S3H-I), appeared in clusters (Figure 3K and S3H) and located in areas far from high *IFN>GFP*-expressing cells (Figure 3N). These observations point towards ISG expression in the absence of high IFN-I production, in line with an IFN-independent ISG induction model (Liu et al., 2019; Schneider et al., 2014). Furthermore, the fraction of *ISRE>tdT*-expressing cells located far from or close to high *IFN>GFP*-expressing cells in ZIKV-infected organoids was similar, in contrast to the distribution observed in organoids stimulated with poly(I:C) (Figure 3N and J), suggesting viral inhibition of paracrine IFN-I signaling. Consistent with this, expression of the IFN-I signaling transducer Stat2, which is targeted for degradation by ZIKV (Grant et al., 2016; Kumar et al., 2016), was reduced in ZIKV-infected regions compared to non-infected areas (Figure S3J). These observations suggest an heterogenous and overall modest activation of the IFN-I response in ZIKV-infected organoids. In contrast to this, in HSV-1-infected organoids we found high *IFN>GFP* and *ISRE>tdT* signals only in a very small fraction of cells (0.03% and 0.7%,

Figure 3O-R), indicating the lack of IFN-I and ISG induction in most cells. Altogether, these results reveal the differential induction of the IFN-I system in organoids infected by ZIKV and HSV-1.

IFN-I response in brain organoids is more attenuated than in 2D cultures

Our finding that IFN-I induction is modest in infected brain organoids was surprising given the strong IFN-I production measured in 2D hNPC cultures (Ferraris et al., 2019; Lima et al., 2019; Simonin et al., 2016; Zhang et al., 2016) and non-neural cultures (Hamel et al., 2015; C. Li et al., 2017). To test whether the magnitude of the IFN-I response is influenced by the culture system or by the cell type composition, we compared the organoid response to the one of 2D cultures obtained from the dissociation of brain organoids (called disOrganoids, Figure S4A) and 2D cultures of non-neural cells such as A549. ZIKV and HSV-1 efficiently replicated in both 2D cultures and these infections proceeded faster than in brain organoids (Figure S4B-E). RT-qPCR analysis at time points that showed similar ZIKV and HSV-1 infection levels across cultures revealed a more prominent induction of *IFNA* and *IFNB1* in disOrganoids and A549 cells compared to the one measured in intact organoids (Figure 4A-D). The only exception was the induction of *IFNA* upon ZIKV infection, which was minimal in all culture systems tested (Figure 4A). Moreover, we analyzed the localization of Irf3, the major transcription factor that drives IFN-I transcription after nuclear translocation (Honda and Taniguchi, 2006) and found that the fraction of cells showing nuclear Irf3 accumulation was larger in disOrganoids and A549 cells compared to brain organoids (Figure 4E-H and S4F). These results confirm a more attenuated activation of the IFN-I response in brain organoids compared to 2D cultures.

Efficient nuclear translocation of Irf3 relies on high expression of pattern recognition receptors (PRRs) mediating cytosolic viral sensing (Zhao et al., 2012). We found low expression of PRRs in early-stage organoids compared to later-stage organoids (Figure S4G), similar to the time-dependent expression timeline seen *in vivo* (Figure S4H). However, PRR expression in early-stage organoids was comparable to the one measured in disOrganoids as well as in 2D cultures of NPCs, and the levels were lower than those measured in A549 cells (Figure 4I). All neural cultures (organoids, disOrganoids and NPCs) also showed similar efficacy of Irf3 nuclear translocation upon poly(I:C) treatment and this was lower than that of A549 cells (Figure 4I-K and S4I). These results suggest cell type-specific modulation of viral sensing and argue against major changes in viral sensing between brain organoids and 2D neural cultures.

IFNβ treatment prevents ZIKV-induced organoid defects

The low levels of IFN-I measured in infected brain organoids could be responsible for their high susceptibility to ZIKV and HSV-1, despite some evidence suggesting that high IFN-I activity might exacerbate damage (Dang et al., 2016; Liu et al., 2019). Consistent with this, *ISRE>tdT* reporter expression correlated with lower levels of apoptosis in ZIKV-infected organoids (Figure S4J). To further demonstrate the neuroprotective effect of the IFN-I system in our infection models, we resorted to the administration of exogenous IFN-I, which inhibit ZIKV and HSV-1 replication in monolayer cultures (Contreras and Arumugaswami, 2016; Härle et al., 2002; Lafaille et al., 2012; Hamel et al., 2015; Lin et al., 2019; Gobillot et al., 2020). We confirmed the ability of two IFN-I subtypes, IFNα2 and IFNβ, to restrict ZIKV and HSV-1 infections in 2D disOrganoid cultures (Figure S5A-D), in line with their similar signaling downstream of the IFN-I receptor (Ivashkiv and Donlin, 2014). Given the major differences in viral kinetics and in the strength of innate immune signaling observed in brain organoids and in 2D cultures, we investigated whether IFN-I treatment could be efficacious also in brain organoid models.

We first applied IFN-I treatments to organoids that had been exposed to ZIKV and found that they both significantly ameliorated ZIKV-induced growth defects (Figure 5A-C). IFN-I treatments were well tolerated, since they did not compromise the growth of MOCK-treated organoids nor they induced large-scale apoptosis (Figure S5E-I). Strikingly, immunohistochemical analysis revealed that IFNβ treatment increased the area of VZ-like regions and reduced ZIKV infection, while IFNα2 showed much lower efficacy (Figure 5D-E). Poor efficacy of the IFNα2 treatment was unlikely due to a lower biological activity, since treatment with a higher dose of IFNα2 failed to further improve the rescue of ZIKV-infected cultures compared to the lower dose (Figure S5J). Also, neuroprotective activity was specific to IFN-I signaling, as treatment with type III IFNs did not ameliorate the growth phenotype nor it induced ISG expression (Figure S5J-K). We then performed RNA-sequencing on ZIKV-infected organoids treated with IFN-I. Principal component analysis (PCA) and differential gene expression data revealed that IFNβ treatment completely reverted the transcriptional changes caused by ZIKV, while IFNα2 treatment rescued gene expression only partially (Figure 5F-G and S5L), in line with our immunohistochemical data. Moreover, IFNβ treatment reduced ZIKV vRNA expression levels already at 4 dpi and even more dramatically at 12 dpi, while IFNα2 treatment failed to do so (Figure 5H). Together, these results reveal the neuroprotective function of the IFN-I system and the superiority of IFNβ over IFNα2 in ameliorating ZIKV-induced organoid defects.

IFNβ treatment fails to prevent HSV-1-induced organoid defects

We next tested the antiviral actions of IFNα2 and IFNβ against HSV-1 by comparing their ability to prevent growth and neuroepithelial defects in organoids that had been previously exposed to HSV-1 (Figure 6A). In contrast to the results obtained with ZIKV-infected organoids and HSV-1-infected 2D cultures, we found that only IFNα2 treatment ameliorated HSV-1-induced organoid growth defects (Figure 6B-C). Consistent with this, IFNα2 treatment improved organoid architecture, suppressed HSV-1 infection and rescued Sox1 expression as well as N-cadherin localization, while IFNβ treatment failed to do so (Figure 6D-G). Furthermore, transcriptional profiling of HSV-1-exposed cultures treated with IFN-I confirmed the inability of IFNβ treatment to rescue the transcriptional changes caused by HSV-1 (Figure 6H-I, S6A). Moreover, analysis of HSV-1 transcripts abundance measured by RNA sequencing confirmed that the IFNα2 treatment efficiently suppressed HSV-1 transcription at 8 dpi and that IFNβ exerted a minor effect (Figure 6J). Together, these results reveal the inability of IFNβ to perform its potent antiviral action against HSV-1, thus supporting differential functions of IFN-I subtypes in brain organoid models.

HSV-1 selectively inhibits IFNβ activity

The poor antiviral activity of IFNβ against HSV-1 could be due to its inability to induce a subset of ISGs counteracting HSV-1 compared to IFNα2. To identify such a subset of ISGs, we analyzed the differential expression signatures of (uninfected) organoids treated with IFNα2 or IFNβ compared to untreated samples. These were enriched in genes implicated in defense response to virus and in response to IFN-I (Figure S6B-D). In contrast with our hypothesis, we found that all DEGs induced by IFNα2 were also found in the IFNβ dataset and that the pattern of differential expression was remarkably similar, with the exception that IFNβ showed higher potency (Figure S6E-F). Even at later time points, the DEGs induced by IFNα2 largely overlapped with those upregulated in the IFNβ dataset. Noticeably though, differences in ISG levels and a time-dependent ISG downregulation specific to IFNα2-treated cultures and reminiscent of the IFNα desensitization (Sandler et al., 2014) became prominent (Figure S6G-H). These data argue against the existence of a set of ISGs uniquely induced by IFNα2, thus ruling out our hypothesis.

An alternative possibility is that HSV-1 might specifically block the activity of IFNβ through the action of one or multiple viral proteins (Danastas et al., 2020). Such an infection-dependent effect is supported by the observation that IFNβ showed potent antiviral activity against HSV-1 when administered to organoids before (but not after) viral exposure (Figure S7A-B), and by the diminished IFNβ-dependent ISG expression in HSV-1-infected cultures compared to MOCK-treated conditions (Figure S7C). We noticed that one of the affected ISGs was the protein kinase

R (PKR), an antiviral effector that inhibits translation of viral mRNAs by phosphorylating eIF2a (Schneider et al., 2014) and whose activity is counteracted by the HSV-1 protein ICP34.5 (Chou et al., 1995). This observation led us to hypothesize that the HSV-1 protein ICP34.5 may counteract IFNβ activity via targeting the PKR pathway. This model predicts that loss of ICP34.5 would render HSV-1 sensitive to IFNβ. We thus performed infections with an HSV-1 mutant strain that carries the deletion of both copies of ICP34.5 genes and referred to as R3616 (Figure S7D) (Chou et al., 1990). ICP34.5-null mutants replicate well in cell culture but they are attenuated in the brains of mice and humans (Bolovan et al., 1994; Chou et al., 1990; Kaur et al., 2012; Leib et al., 1999). Consistent with *in vivo* neuroattenuation, the ICP34.5-null strain R3616 reduced organoid growth less efficiently than wild type (wt) HSV-1 especially at the low inoculum dose and exhibited limited viral spreading and viral particle release compared to wt HSV-1 (Figure 7A-I). Importantly, when R3616 showed prominent infection, its replication was efficiently blocked by IFNβ (Figure 7J-M), consistent with our prediction. R3616 infection did not change the expression levels of ISGs similar to wt HSV-1, ruling out a direct role of ICP34.5 in ISG induction (Figure S7E). Together, these results indicate that HSV-1 selectively inhibits IFNβ action in part via ICP34.5.

DISCUSSION

Here we establish human brain organoid models for two distinct TORCH viruses, ZIKV and HSV-1. We show that these two models share features of microcephaly but exhibit major differences in the underlying structural defects and transcriptional profiles, as well as in the engagement of the antiviral system and sensitivity to IFN-I. These results argue for the existence of unique pathogenic mechanisms underlying virus-induced microcephaly and the use of tailored antiviral strategies against TORCH pathogens.

Both ZIKV and HSV-1 infect hNPCs leading to productive infection and causing reduced organoid size and cell depletion. These data implicate hNPC infection in TORCH neuropathogenesis and are consistent with other organoid models of ZIKV and HSV-1 infection (Cugola et al., 2016; Gabriel et al., 2017; Garcez et al., 2016; Qian et al., 2016; Qiao et al., 2020; M. Watanabe et al., 2017) as well as with the clinical findings associated with viral exposure in the first and second trimesters of pregnancy (Honein et al., 2017; Marquez et al., 2011). HSV-1 infection in organoids appears more destructive than that caused by ZIKV, in line with the high severity of *in utero* HSV infections (Marquez et al., 2011). In contrast to this, HCMV shows limited tropism for primitive hNPCs and poor replication in early-stage organoids. This phenotype is likely due to the lack of intermediate progenitors (Kanton et al., 2019), a population of hNPCs recently

identified as the major cellular target of HCMV in a 45-days-old organoid model of microcephaly (Sun et al., 2020). These data suggest different neurotropism of TORCH viruses in the human fetal brain.

Mechanistically, we show that both ZIKV and HSV-1 infections trigger apoptosis, as previously reported (Cairns et al., 2020; Cugola et al., 2016; Hanners et al., 2016; Qian et al., 2016; Souza et al., 2016; M. Watanabe et al., 2017). Apoptosis likely represents a general cellular defense against viral spreading that could explain the neurotoxicity of congenital TORCH infections. Yet, our analysis of apoptosis and lumen size suggests that different mechanisms of tissue damage may be involved. Whereas ZIKV infection likely reduces the lumen size by basal delamination of apoptotic cells from the neuroepithelium, HSV-1 infection results in enlarged lumens possibly through apical extrusion of apoptotic cells. Furthermore, our data suggest that HSV-1 is unique in its ability to cause neuropathology by impairing neuroepithelial integrity, in line with the key roles of cell adhesion in controlling NPC proliferation and maintenance during brain development (Chenn and Walsh, 2002; Hatakeyama et al., 2014; Kadowaki et al., 2007; Rousso et al., 2012). HSV-1 may perturb neuroepithelial polarity either by promoting N-cadherin cleavage (Reiss et al., 2005) or by disrupting adherens junctions via binding to the cell adhesion molecule Nectin1 (Krummenacher et al., 2003; Richart et al., 2003; Simpson et al., 2005). Remarkably, these cytoarchitectural changes seen in organoids are distinct from the large multicellular structures observed in 2D neural cultures (this study and (Cairns et al., 2020)). These discrepancies are likely due to major changes in cell adhesion and polarity of NPCs grown in monolayer and 3D organoid cultures (Scuderi et al., 2021), confirming the superiority of brain organoids in mimicking the neuropathological features associated with HSV-1 infection.

The structural and cellular differences of ZIKV and HSV-1 organoid models are also reflected in their transcriptional profiles. While cell death is concomitant with the activation of cellular stress- and virus defense-related pathways in ZIKV-infected cultures in agreement with previous studies (Gladwyn-Ng et al., 2018; Liu et al., 2019; M. Watanabe et al., 2017), apoptosis is linked to the upregulation of ATF and Jun/Fos families of transcription factors and the activation of non-neural developmental pathways in HSV-1-infected cultures. In the case of HSV-1, it is possible that this transcriptional activation is required to ensure efficient replication, as HSV-1 induces similar profiles in other cells (Drayman et al., 2019; Hensel et al., 2019; Hu et al., 2016). Another option is that the deregulation of non-neural genes caused by HSV-1 could contribute to the loss of neuroepithelial identity. Indeed, the altered hNPC morphology, reduced apical N-cadherin localization and the disintegration of infected organoids are reminiscent of the

morphological changes, lowered cadherin levels and weakened adhesion of mesenchymal cells (Thiery et al., 2009).

Our work highlights major differences in the cellular innate response against ZIKV and HSV-1 and their sensitivity to IFN-I. While these disparities are perhaps not surprising given the great diversity of the two viruses, these phenotypes are unique to brain organoids. We show that both ZIKV and HSV-1 infections of organoids attenuate IFN-I responses much strongly as compared to 2D cultures, helping resolve a discrepancy in the field on the magnitude of the antiviral response between 2D and 3D culture systems (C. Li et al., 2017; Lima et al., 2019; Liu et al., 2019; Simonin et al., 2016; Zhang et al., 2016). The attenuated IFN-I response of organoids is consistent with the low immune reactions described in the microcephalic brains of ZIKV-infected patients (Lima et al., 2019) and with the generally low IFN-I activity of the brain (Sorgeloos et al., 2013). Changes in the modulation of innate immune reactions between 3D and 2D culture systems may result from differences in infectivity levels and/or viral spreading, since we observed lower initial infection levels and much slower kinetics of viral replication in 3D compared to 2D culture. A slow kinetics often reflects a small fraction of infected cells and could thus explain the rare activation of IFNβ transcription measured by our reporter assay. These discrepancies could result from inefficient cell targeting due to limited cell surface accessibility and/or from reduced local spreading due to stronger cell-to-cell contacts in 3D as compared to 2D culture.

Moreover, our work reveals that ZIKV and HSV-1 replication in organoid cultures is differentially sensitive to the action of distinct IFN-I subtypes. These results lend support to the neuroprotective function of the IFN-I system against viral infections (Gorman et al., 2018; Leib et al., 1999; C. Li et al., 2017; Lin et al., 2019; Sorgeloos et al., 2013; J. P. Wang et al., 2012) and to the view that distinct IFN subtypes can mediate different biological outcomes (Ng et al., 2016). Nevertheless, it is surprising that distinct IFN-dependent viral phenotypes are detectable in 3D, while remaining indistinguishable in 2D cultures (this study and (Contreras and Arumugaswami, 2016; Härle et al., 2002; Lafaille et al., 2012)). A contributing factor could be the duration of the IFN-I treatment, since the pattern of ISG expression induced by IFNα/β starts to differ after repeated administrations. Viral phenotypes in 3D might also be strongly influenced by viral immune evasion mechanisms (Chou et al., 1990; Danastas et al., 2020; Gorman et al., 2018; Grant et al., 2016; Kumar et al., 2016). The reduced efficacy of IFN-I against ZIKV in 3D vs 2D, the neuroattenuation of the ICP34.5-null HSV-1 mutant and the poor IFNβ activity against HSV-1 in brain organoids are compatible with this possibility.

Finally, our work uncovers the existence of previously unappreciated differences in IFN-I activities. The superior antiviral activity of IFNβ over IFNα2 against ZIKV infection likely reflects

the longer-lasting and more potent ISG induction by IFNβ over IFNα2, in line with the higher potency of IFNβ (Bolen et al., 2014; Gobillot et al., 2020). More intriguing is the poor antiviral activity of IFNβ against HSV-1 since this effect could be specific to the brain. In fact, IFNβ potently inhibits HSV-1 replication in other cells and in mice (Arao et al., 1997; Carr et al., 2003; Giraldo et al., 2020; Härle et al., 2001). Our pre and post-treatment IFNβ experiments with wt and ICP34.5-null HSV-1 viruses indicate that HSV-1 selectively neutralizes IFNβ action, in line with the well-described ability of HSV-1 to evade IFN-I signaling (Danastas et al., 2020). This mechanism may represent an efficient strategy to target the most potent IFN type in the brain when both IFNα species and IFNβ are produced (Sorgeloos et al., 2013). Our results suggest that such evasion mechanism is in part mediated by the viral protein ICP34.5, which possibly counteracts ISG induction and PKR activity downstream of IFN-I signaling (Chou et al., 1995; He et al., 1997). However, since PKR is induced and likely activated also in IFNα2-treated organoids, future work is needed to characterize the mechanisms determining the selectivity against IFNβ.

In conclusion, the organoid infection models described in this work have a great utility for evaluating therapeutics against ZIKV and HSV-1 and can serve as experimental platforms for better characterizing the activity of human IFNs. Although our results support the therapeutic use of specific IFN-I against ZIKV and HSV-1 infections, our understanding of IFN activities in humans is limited, as reflected in the toxicity and efficacy issues of IFN-based therapies (Fritz-French and Tyor, 2012; S.-F. Li et al., 2018). Mechanistic studies on ISG functions in these organoid infection systems will help guide the design of more efficacious IFN-I modulatory compounds. Furthermore, our infection models for HSV-1 could serve as platforms for further characterization of HSV-1 evasion mechanisms and for testing of HSV-1 mutants. This work will help improve the design of oncolytic HSV-1 vectors that could overcome the limited efficacy of current HSV-1 viruses in glioblastoma therapy (Kaur et al., 2012). More broadly, our work calls for a paradigm shift to human 3D systems for the study of viral mechanisms that will be instrumental for the development of more effective antiviral compounds for the treatment of neurological complications.

Limitation of the study

Our analysis of antiviral signaling is limited by the small number of antiviral genes analyzed and by the lack of time-resolved tissue dynamics of viral and host proteins expression. Such analyses in large 3D tissue-like brain organoids are technically challenging and the application of emerging techniques, such as spatial transcriptomics (Burgess, 2019) and live 3D tissue fluorescent imaging (Rios and Clevers, 2018) in an appropriate bio-safety setting, will allow greater insights into the tissue dynamics of viral spreading and antiviral signaling. Another limitation of the organoid models used in this study is their low cellular complexity, which does not

recapitulate the full repertoire of neural cells seen in late-stage organoid cultures (Kanton et al., 2019), and their lack of the microglia, a limitation of current organoid models (Amin and Paşca, 2018). The development of co-culture systems of late-stage organoid cultures and microglia will be instrumental to better recapitulate fetal neuroimmune interactions that could be relevant for viral pathogenesis.

ACKNOWLEDGEMENTS

We thank all members of the Knoblich laboratory for technical expertise and feedback. We thank the Organoid research unit, Lena Schwarz and Paul Möseneder for technical support, the IMBA/IMP BioOptics facility for flow cytometry and microscopy services, IMP/IMBA Bioinformatics for sequencing analysis, A. Kavirayani and the VBCF HistoPathology facility (www.viennabiocenter.org/facilities) for histological support and consultation, A. Sommer and VBCF Sequencing unit (www.viennabiocenter.org/facilities) for sequencing. We also thank the EVAg project, Anna Obenauf (IMP, Austria) and Luka Cicin-Sain (Helmholtz Centre for Infection Research, Germany) for providing reagents. V.K. received funding from an EMBO Fellowship (ALTF 1312-2015) and from the European Union's Horizon 2020 research and innovation programme under the Marie Skłodowska-Curie grant agreement No. 703112. C.B. is a member of the VBC doctoral programme. Work in U.K's laboratory is supported by the Helmholtz Zukunftthema "Immunology & Inflammation" (ZT-0027). Work in A.M's laboratory is supported by the Swedish Research Council (2018-05766). Work in J.A.K.'s laboratory is supported by the Austrian Federal Ministry of Education, Science and Research, the Austrian Academy of Sciences, the City of Vienna, the Austrian Science Fund (Special research program F78 Stem Cell, F 7803-B, and SFB-F78 P04) and a European Research Council Advanced Grant under the European Union's Horizon 2020 program (No. 695642).

AUTHOR CONTRIBUTIONS

V.K. and J.A.K conceived the project and wrote the manuscript with input from all authors. V.K performed experiments, collected and analyzed the data with help from C.B. T.R.B. performed bioinformatic analysis. J.S. and U.K. contributed to the conceptualization of the project, provided reagents and technical expertise. A.C., C.S. and A.M. contributed reagents and technical expertise. R.R.C. and P.P.G. helped with experimental design and data interpretation. J.A.K. acquired funding.

DECLARATION OF INTERESTS

J.A.K is inventor on a patent describing cerebral organoid technology and co-founder and scientific advisory board member of a:head bio AG.

MAIN FIGURE TITLES AND LEGENDS

Figure 1. ZIKV and HSV-1 infections impair organoid growth

A-B) Images (scale bars 200 μm) and area measurements of organoids exposed to ZIKV or MOCK-treated. Values are mean ± SD and represent individual organoids (p=0.7886 4 dpi; p=0.3190 8 dpi; **** is p<0.0001; Mann-Whitney test). $TCID_{50}$, mean tissue culture infectious dose.

C) RT-qPCR analysis of ZIKV viral RNA (vRNA) in organoids exposed to ZIKV. Values are mean ± SEM (p=0.1 1 dpi; p=0.0022 4 dpi; p=0.0286 12 dpi; Mann-Whitney test over age-matched MOCK-treated).

D) Immunostaining of Vero cells (scale bars 100 μm) incubated with supernatants (sup) of ZIKV-infected organoids. ZIKVA, ZIKA Virus Antigen.

E-G) Immunostaining (scale bars are 100 μm) of organoids exposed to ZIKV or MOCK-treated. Dashed lines indicate organoid contour based on DAPI signal (not shown). Insets in F (scale bars 50 μm) show a magnified view of the ventricular zone (VZ)-like structures (dashed lines) and their lumens (dotted lines). Violin plots indicate median and quartiles (n=129 regions from 11 MOCK, n=109 from 13 ZIKV organoids from 3 experiments; **** is p<0.0001; Mann-Whitney test).

H-I) Images (scale bars 200 μm) and area measurements of organoids exposed to HSV-1 (10^2 PFU) or MOCK-treated. Values are mean ± SD and represent individual organoids (p=0.6625 4 dpi; **** is p<0.0001; Mann-Whitney test).

J) RT-qPCR analysis of HSV-1 gene Thymidine Kinase (TK) in organoids exposed to HSV-1 (10^2 PFU). Values are mean ± SEM (p>0.9999 1 dpi; p=0.4004 4 dpi; p=0.0079 8 dpi; Mann-Whitney test over age-matched MOCK-treated).

K) Immunostaining of Vero cells (scale bars 100 μm) incubated with supernatants (sup) from HSV-1-infected organoids (10^2 PFU).

L-M) Immunostaining (scale bars 100 μm in L, 20 μm in M) of organoids exposed to HSV-1 (10^3 PFU) and analyzed at 4 dpi. Arrows indicate chromatin localization (marked by DAPI) at the nuclear periphery.

N-O) Immunostaining (scale bars 100 μm) of organoids exposed to HSV-1 (10^2 PFU) or MOCK-treated. Dashed lines indicate organoid contour based on DAPI signal (not shown). Insets (scale bars 50 μm) show a magnified view of ventricular zone (VZ)-like structures (dashed lines) around lumens (dotted lines). Inset from HSV-1 samples underwent a 180° rotation. Violin plots indicate median and quartiles (n=146 regions from 15 MOCK, n=69 from 16 HSV organoids from 3 experiments; **** is p<0.0001, Mann-Whitney test).

ns, non-significant; dpi, days post-infection. See also Figure S1, Table S1 and S2.

Figure 2. ZIKV and HSV-1 infections elicit distinct transcriptional responses

A-B) Graphs showing the number of differentially expressed genes (DEGs) in virus-infected organoids.

C) Top 10 Gene Ontology (GO)-terms of downregulated genes (log2FoldChange <1) in ZIKV vs. MOCK-exposed organoids (12 dpi).

D) Venn diagram showing limited overlap between the two datasets.

E and H) Top 10 GO-terms of upregulated genes (log2FoldChange >2) in virus-infected organoids (12 dpi in E, 8 dpi in H).

F and I) Top 10 results of ChEA3 transcription factor (TF) analysis performed on upregulated genes.

G and J) Expression of the top 25 upregulated genes in ZIKV-infected organoids (12 dpi, in G) or in HSV-1-infected organoids (8 dpi, in J). FC, fold change.

K-M) Immunostaining (scale bars 50 μm in K-L, 20 μm in M) of infected and MOCK-treated organoids. Dashed lines and asterisks indicate organoid surface based on DAPI signal (not shown) and lumen respectively.

dpi, days post-infection. See also Figure S2 and Table S3.

Figure 3. ZIKV and HSV-1 infections differentially engage the IFN-I system

A-B) Cluster of densely connected genes among genes upregulated in ZIKV-infected organoids at 12 dpi (in A) and their HOMER *de novo* motif analysis (in B).

C) Expression analysis of genes from A in infected organoids compared to their MOCK controls.

D-E) Quantification of IFNα and IFNβ levels measured by ELISA assay. Values represent mean ± SEM (Mann-Whitney tests).

F) Schematic diagram of *IFNB1>GFP (IFN>GFP)* and *ISRE>tdTomato (ISRE>tdT)* reporters.

G-R) Immunostaining (scale bars 100 μm) of organoids generated from reporter cells and analyzed one day after stimulation with poly(I:C) in G, or after ZIKV or HSV-1 exposure (in K and O). Dashed lines indicate organoid contour based on DAPI (not shown). Insets (scale bars 50 μm) represent a magnified view of the area close to one single *IFN>GFP*+ cell (arrows). Arrowheads indicate *ISRE>tdT*+ cells. Graphs are Tukey plots (n≥3; p=0.0211 in H, p=0.0007 in I, p=0.0068 in J, p=0.0273 in L, p=0.0091 in M, p=0.3175 in N, p=0.0857 in P, p=0.6820 in Q, p=0.5994 in R, Mann-Whitney tests). Ctrl, control transfection. ns, non-significant.

dpi, days post-infection; See also Figure S3.

Figure 4. The IFN-I response in brain organoids is more attenuated than in 2D cultures

A-D) Quantification of *IFNA* and *IFNB1* expression by RT-qPCR in cultures exposed to ZIKV (in A-B) or HSV-1 (in C-D). Dotted lines indicate the value of 1. Values are mean ± SEM (n=3 for A549, n=4 for disOrg, n=7 for ZIKV organoids, n=3 for HSV-1 organoids; ZIKV *IFNA*: p=0.8985 A549 1 dpi; p=0.0823 A549 4 dpi; p=0.6069 disOrg 2 dpi; p=0.9784 disOrg 4 dpi; p=0.7633 Org 4 dpi; p=0.0057 Org 12 dpi; ZIKV *IFNB1*: p=0.0005 A549 1 dpi; p=0.0015 A549 4 dpi; p=0.7036 disOrg 2 dpi; p=0.0008 disOrg 4 dpi; p=0.2135 Org 4 dpi; p=0.0333 Org 12 dpi; HSV-1 *IFNA*: p=0.5876 A549 1 dpi; p=0.0105 A549 4 dpi; p=0.1457 disOrg 2 dpi; p=0.0183 disOrg 4 dpi; p=0.2903 Org 4 dpi; p<0.0001 Org 8 dpi; HSV-1 *IFNB1*: p=0.0794 A549 1 dpi; p=0.1054 A549 4 dpi; p=0.3126 disOrg 2 dpi; p=0.0056 disOrg 4 dpi; p=0.4055 Org 4 dpi; p=0.2250 Org 8 dpi; Mann-Whitney test comparisons of infected samples vs age-matched MOCK samples).

E-H) Immunostaining (scale bars 100 μm) and quantification of Irf3 nuclear localization. A549 and disOrganoids were analyzed at 4 dpi, organoids at 12 dpi (in E) or 8 dpi (in F). ZIKVA, Zika virus Antigen; ICP4, infected cell polypeptide 4 protein of HSV-1. Color code as in A. Values are mean ± SEM (p=0.0007 in G; p<0.0001 in H; one-way ANOVA).

I) Expression of nucleic acid sensors measured by RT-qPCR. Values are mean ± SEM (n=3, p=0.3387 RIG-I; p=0.0063 DHX58; p=0.0432 TLR7; **** is p<0.0001; one-way ANOVA).

J-K) Immunostaining (scale bars 20 μm) and quantification of Irf3 nuclear accumulation after poly(I:C) treatment. Values are mean ± SEM (n=3; p<0.0001, one-way ANOVA).

ns, non-significant; dpi, days post-infection. See also Figure S4.

Figure 5. IFN*β* treatment prevents ZIKV-induced organoid defects

A) Timeline of interferons (IFN-I) treatment. Organoids were analyzed at 12 dpi.

B-C) Images (scale bars 200 μm) of organoids treated as in A and area quantification. Values are mean ± SD and represent individual organoids (**** is p<0.0001, p=0.0063 ZIKV+IFNα2 vs ZIKV, p=0.0021 ZIKV+IFNβ vs ZIKV, p>0.9999 ZIKV+IFNα2 vs ZIKV+IFNβ, p=0.0015 ZIKV+IFNα2 vs MOCK, p=0.0117 ZIKV+IFNβ vs MOCK, Kruskal-Wallis test).

D-E) Immunostaining (scale bars 200 μm) of organoids and area quantification of ventricular zone (VZ)-like regions. Violin plots show median and quartiles (n=114 regions from 6 MOCK organoids, n=55 from 7 ZIKV organoids, n=73 from 7 ZIKV+IFNα2 organoids, n=106 from 7 ZIKV+IFNβ organoids; p=0.0026 ZIKV+IFNα2 vs MOCK; p>0.9999 ZIKV+IFNβ vs MOCK; **** is p<0.0001; Kruskal-Wallis test).

F-G) Principal Component Analysis (PCA) and expression (in scaled variance stabilizing transformation or VST) of differentially expressed genes.

H) Quantification of ZIKV viral RNA (vRNA) expression measured by RT-qPCR in organoids treated as in A. Values are mean ± SEM (4dpi: p=0.0017 ZIKV+IFNα2 vs ZIKV, p=0.0005 ZIKV+IFNβ vs ZIKV; **** is p<0.0001; one-way ANOVA Tukey's multiple comparisons test).
dpi, days post-infection; ns, non-significant. See also Figure S5 and Table S2.

Figure 6. IFN*β* treatment fails to prevent HSV-1-induced organoid defects

A) Timeline of IFN-I administration. Organoids were analyzed at 8 dpi.
B-C) Images (scale bars 200 μm) and area quantification of organoids treated as in A. Values are mean ± SD (**** is p<0.0001; p=0.0043 HSV+IFNα2 vs HSV; p>0.9999 HSV+IFNβ vs HSV; p=0.0587 HSV+IFNα2 vs HSV+IFNβ; p>0.9999 HSV+IFNα2 vs MOCK; p=0.0007 HSV+IFNβ vs MOCK; Kruskal-Wallis test).
D and F) Immunostaining (scale bars 200 μm) of organoids. Dashed lines indicate organoid contour.
E) Quantification of Sox1 mean intensity per cell. Violin plots show median and quartiles (n>3000 cells from at least 3 organoids per condition, **** is p<0.0001, Kruskal-Wallis test).
G) Quantification of the ventricular zone (VZ)-like regions marked by N-Cadherin (N-Cad) apical accumulation. Data are mean ± SEM (n=3 experiments; **** is p<0.0001, ns is p>0.9999; Kruskal-Wallis test).
H-I) Principal Component Analysis (PCA) and expression (in scaled variance stabilizing transformation or VST) of genes differentially expressed in HSV-1-infected organoids.
J) Percentage of RNA-sequencing reads aligned to the HSV-1 genomic sequence. Values are mean ± SEM (for 4 dpi: p=0.8613 MOCK vs HSV, p=0.9975 HSV+IFNα2 vs HSV, p=0.8447 HSV+IFNβ vs HSV; for 8 dpi: p=0.003 MOCK vs HSV, p=0.0003 HSV+IFNα2 vs HSV, p=0.2943 HSV+IFNβ vs HSV, one-way ANOVA Tukey's multiple comparisons test).
dpi, days post-infection; ns, non-significant. See also Figure S6 and Table S2.

Figure 7. HSV-1 selectively counteracts IFN*β* activity

A-F) Images (scale bars 200 μm) and area quantifications of organoids exposed to HSV-1 wild type (WT), R3616 mutant or MOCK-treated and analyzed at 8 dpi. Values are mean ± SD and represent individual organoids (in B: for wt, p=0.0066 and p=0.0021; for R3616 p=0.0008 and p=0.7802; in E: for wt p=0.0002, p=0.02, p=0.0232 and p=0.1606; for R3616, p=0.8148, p=0.5701, p=0.7394; **** is p<0.0001; Mann-Whitney test comparisons to MOCK counterparts).

Outcomes of infection experiments shown in C and F are based on statistical significance (strong if $p<0.005$, mild if $0.005<p<0.05$ or none if $p>0.05$).

G-H) Immunostaining (scale bars 200 μm) and quantification of infected organoid area at 8 dpi. Dashed lines indicate organoid contour. Data are mean ± SD (n=6 organoids for WT, n=7 for R3616).

I) Immunostaining (scale bars 100 μm) of Vero cells incubated with supernatants (Sup) from HSV-1 WT- or R3616-infected organoids at 8 dpi.

J-M) Images, immunostaining (scale bars 200 μm) and quantification of organoid infected area at 8 dpi. Refer to Figure 6 for comparison to wt HSV-1. Values in K are mean ± SD (n=6 untreated organoids, n=7 organoids for IFNα2 and IFNβ; **** is $p<0.0001$; ns is p $p>0.9999$; $p=0.0020$ R3616+IFNα2 vs R3616; Kruskal-Wallis test).

dpi, days post-infection; ns, non-significant. See also Figure S7, Table S1 and S2.

STAR METHODS

RESOURCE AVAILABILITY

Lead Contact

Information and requests regarding reagents and biological materials should be addressed to the Lead Contact, Dr. Jürgen Knoblich (juergen.knoblich@imba.oeaw.ac.at).

Materials availability

All unique reagents and biological materials generated in this study are available from the Lead Contact, Dr. Jürgen Knoblich (juergen.knoblich@imba.oeaw.ac.at), in compliance with Material Transfer Agreements (MTA).

Data and Code availability

RNA-seq data generated in this study have been deposited at NCBI Gene Expression Omnibus (GEO) under the accession numbers GSE123816 and GSE145496. The data that support the findings of this study are available from the Lead contact Dr. Jürgen Knoblich (juergen.knoblich@imba.oeaw.ac.at) upon reasonable request.

EXPERIMENTAL MODEL AND SUBJECT DETAILS

Human embryonic stem cells and cell lines

Human embryonic stem cells (hESC) H9 were obtained from WiCell. Human lung epithelial carcinoma A549 cells and African green monkey kidney Vero cells were obtained from ATCC and maintained in regular Dulbecco's minimal essential medium (DMEM) supplemented with 10% fetal bovine serum (FBS) and 2 mM L-Glutamine. All cells were authenticated using a short tandem repeat (STR) assay. All cells were maintained in a 5% CO_2 incubator at 37°C and routinely tested for mycoplasma.

Viruses

The French Polynesian ZIKA virus strain (ZIKV, H/PF/2013) was propagated in Vero cells. Briefly, Vero cells were infected with ZIKV at multiplicity of infection (MOI) 0.1 and incubated at 37°C in a 5% CO_2 incubator. At 3 days post-infection, cell supernatants from infected cells were harvested and purified by centrifugation at 1500 rpm for 10 min to remove cellular debris. The viral titre was determined by tissue culture infective dose (TCID) assay performed on Vero cells. Briefly, confluent Vero cells plated in 96-well plates were infected with serially diluted ZIKV stocks and

incubated at 37°C in a 5% CO_2 incubator. The assay was carried out in eight parallels wells for each dilution with the last column of 96-well plate as control cells without virus. At 5 days post-infection, the appearance of cytopathic effect (CPE) was examined by microscopy. The $TCID_{50}$ was calculated from the CPE induced in the cell culture. The wild type Herpes Simplex virus 1 (wt HSV-1, strain F) and the R3616 mutant HSV-1 virus (HSV-1 R3616, strain F) were generated previously (Chou et al., 1990) and kindly provided by B. Roizman (University of Chicago, Chicago, IL). HSV-1 viruses were grown and subjected to titer determination by plaque assay on Vero cell monolayers as previously described (Calistri et al., 2003). Human Cytomegalovirus (HCMV, strain TB40/E) expressing mNeonGreen fluorescence protein under the control of the endogenous HCMV major immediate-early (MIE) promoter of UL122/123 genes (HCMV-UL122/123-mNeonGreen) was generated and kindly provided by L. Cicin-Sain (Helmholtz Centre of Infection Research, (Kasmapour et al., 2018). Note that this modified virus shows similar growth kinetics to the parental strain (Kasmapour et al., 2018). Viral stocks were aliquoted and stored at -80°C. Supernatants from uninfected Vero cells were prepared as performed during viral propagation and used as MOCK controls. Infection experiments were conducted under Biosafety Level 2 Plus containment.

METHOD DETAILS

Maintenance of hESCs

H9 cells were cultured under feeder-free or feeder-dependent conditions. Feeder-free H9 cells were seeded onto 6-well plates coated with hES-qualified matrigel and maintained in mTeSR1 medium. Cells were fed daily and passaged every 3-4 days using 0.5 mM EDTA solution treatment and mechanical dissociation. Feeder-dependent H9 cells were cultured on CF-1-γ-irradiated mouse embryonic fibroblasts seeded one day in advance onto gelatin-coated [0.1% (wt/vol) gelatin] 6-well plates. Cells were fed daily with stem cell medium containing DMEM-F12 supplemented with 20% KnockOut Serum Replacement, 3% FBS, 1X GlutaMAX, 1X minimum essential medium amino acids (MEM-NEAA), 0.1 mM beta-mercaptoethanol (BME), 20 ng/ml bFGF as previously described (Lancaster and Knoblich, 2014). Cells were passaged every 5-7 days following treatment with collagenase IV (0.1% wt/vol) for 15 minutes and mechanical dissociation.

Generation of interferon reporter lines

The reporter constructs were inserted into the AAVS1 safe-harbor locus of feeder-free H9 cells or A549 cells using TALEN technology as described before (Bagley et al., 2017). Donor plasmids were constructed to insert the following cassettes: (i) 2APuro-2xCHS4-IFNB1>eGFP-

WPRE-SV40-2xCHS4 and (ii) 2ANeo-2xCHS4-ISRE>tdTomato-WPRE-SV40-2xCHS4. Fragments spanning -1425 base pairs (bp) downstream and 40 bp upstream of the transcription start site of the human *IFNB1* gene and 353 bp downstream and 74 bp upstream of the transcription start site of the human *ISG15* gene (Hummer et al., 2001) were used as promoters. All donor plasmids were verified by sequencing. For reporter integration in H9 cells, 10^6 single cells prepared using accutase were nucleofected with the Amaxa nucleofector (Lonza) and Human Stem Cell Nucleofector Kit 1 solutions containing 0.5 μg of each of the TALEN plasmids and 1 μg of each of the two donor plasmids following manufacturer's guidelines. Nucleofected cells were grown for four days and then selected with 0.5 μg/ml puromycin and 100 μg/ml G418. For reporter integration in A549 cells, 1.2 x10^6 cells were seeded and one day later transfected with Lipofectamine 3000 and 1 μg of each of the TALEN plasmids and 1.5 μg of each donor plasmid following manufacturer's instructions. One day later, the medium was replaced and A549 cells were selected with 0.5 μg/ml puromycin and 750 μg/ml G418 starting from day 2. Surviving colonies of H9 and A549 were picked manually, transferred into 24-well plates and further expanded for genotyping and cryopreservation. For genotyping, DNA was extracted using the QuickExtract DNA Extraction Solution and a PCR assay was performed to identify correctly targeted AAVS1 insertions and loss of wild-type alleles in multiple clones. For *ISRE>tdTomato* expression analysis performed by flow cytometry (Figure S3C), organoids generated from reporter cells (12-days-old) were incubated with recombinant interferons or vehicle. One day later, organoids were manually dissociated into single cells after 5 minutes of incubation with an accutase:trypsin (2:1 v/v) mix at room temperature. Single cell suspensions were diluted into 300 μl of culture medium and tdTomato expression was analyzed by flow cytometry performed on a LSRFortessa cell analyzer (BD Biosciences) using BD FACSDIVA software. Data were analyzed using FlowJo.

Generation of cerebral organoids

Cerebral organoids were generated as previously described (Lancaster et al., 2013; Lancaster and Knoblich, 2014). Briefly, on day 0 hESCs were dissociated into single cells by accutase treatment (feeder-free cells) or by collagenase IV/dispase treatment followed by a short treatment with trypsin (feeder-dependent cells). Cells were transferred to an ultra-low binding 96-well plate (9000 cells/well) containing stem cell medium supplemented with 4 ng/ml bFGF and 50 μM Rho-associated protein kinase (ROCK) inhibitor. On day 3, the medium was replaced with fresh stem cell medium. From day 5 or 6, the medium was replaced daily with Neural Induction Medium containing DMEM-F12 supplemented with 1X N2 supplement, 1ug/ml heparin solution, 1X GlutaMAX and 1X MEM-NEAA. On Day 10 or 11, organoids with visible neuroepithelia were

762 embedded into droplets of Matrigel and transferred into 6-cm dishes in Expansion Medium
763 consisting of 50% DMEM-F12, 50% Neurobasal medium, 1X N2, 1X B27 – Vitamin A, 2.5 μg/ml
764 Insulin, 0.05 mM BME, 1X GlutaMAX, 1X MEM-NEAA and 1X Penicillin/Streptomycin. On day 15,
765 media was replaced with Differentiation Medium consisting of 50% DMEM-F12, 50% Neurobasal
766 medium, 1X N2, 1X B27, 2.5 μg/ml Insulin, 0.05mM BME, 1X GlutaMAX, 1X MEM-NEAA, 1X
767 Penicillin/Streptomycin and organoids were cultures on an orbital shaker under 57 rpm rotating
768 speed. The medium was changed every 2-3 days. From day 40 onwards, organoids were fed with
769 Differentiation Medium supplemented with 1% (v/v) matrigel basement membrane. From day 65
770 onwards, organoids were fed with Differentiation Medium supplemented with BDNF (20 ng/ml),
771 GDNF (20 ng/ml) and db-cAMP (1 mM). Organoids that passed the quality control criteria
772 (Lancaster and Knoblich, 2014) were used. Criteria included visible surface brightening before
773 embedding (as a proxy for an organized neuroepithelium) and formation of neural tube-like
774 structures in matrigel.
775 *Generation of 2D neural cultures*
776 To generate dissociated 2D cultures of organoids (disOrganoids), 10-days-old organoids were
777 plated onto matrigel-coated dishes in Neural Induction Medium. Three days later, plated
778 organoids were incubated with accutase for 15 min at 37°C and manually dissociated into a single
779 cell suspension. After a washing step, cells were resuspended in Neural Induction Medium
780 supplemented with 10 μM ROCK inhibitor and plated as single cells onto matrigel-coated plates.
781 One day later, the medium was replaced with Expansion Medium. Two days later (day 16), cells
782 were dissociated again with accutase and plated onto matrigel-coated surfaces for further
783 analysis. An outline of this protocol is presented in Figure S4A. To differentiate hESCs into hNPCs
784 directly in 2D, we adapted a previously published protocol (Qi et al., 2017). Briefly, cells were
785 dissociated with accutase and plated onto matrigel-coated plates at the density of 200,000
786 cells/cm^2 in mTeSR1 supplemented with 10 μM ROCK inhibitor. Differentiation was started the
787 next day using E6 medium. Inhibitors used in LSB+X induction in E6 included LDN193189 (100
788 nM), SB431542 (10 μM) and XAV939 (2 μM) for treatment of 3 days. Then starting from day 3,
789 LDN193189 (50 nM), SB431542 (5 μM), XAV939 (1 μM), SU5402 (2 μM) and DAPT (5 μM) were
790 added to E6. On day 6, cells were dissociated by incubation with accutase at 37°C for 15 minutes,
791 resuspended in E6 medium supplemented with 10 μM ROCK inhibitor and plated onto poly-L-
792 ornithine (50 μg/ml) and laminin (5 μg/ml)-coated surfaces for further analysis. An outline of this
793 protocol is shown in Figure S4I.

Infection of cerebral organoids

Organoid infection experiments were performed by adapting previous ZIKV infection paradigms (Dang et al., 2016; Gabriel et al., 2017). On day 10 or 11, organoids were incubated with a virus inoculum diluted in 200 µl of Neural induction Medium in ultra-low binding 96-well plates. An equivalent volume of MOCK medium was used for uninfected controls. Plates were incubated at 37°C in a 5% CO_2 incubator. One day later, organoids were embedded in Matrigel, transferred to 6-cm dishes in Expansion medium and cultured as described above. Details on the number of virus particles used in this study are provided in Table S1 and S2. For infection at later stages, 40-days-old organoids were exposed to 600 PFU of HSV-1 diluted in Differentiation medium. One day later, the medium was replaced with fresh Differentiation medium containing 1% (v/v) matrigel basement membrane and cultured as described above. Supernatants were collected at 4, 8 or 12 dpi and frozen at -80°C. 125 µl of each supernatant was used to infect Vero cells in 12-well plates. Cells were fixed 24 hours post-infection and the level of infection was assessed by viral antigen expression using immunostaining.

Infection of 2D cultures

disOrganoids (day 17) were seeded onto glass coverslips in 12-well plates at a seeding density of 150000 cells/well. One day later, cells were incubated with 150000 $TCID_{50}$ units of ZIKV or with 187.5 PFU of HSV-1 for one day. For infection in A549 cells, 80000 cells were seeded onto a glass coverslip in 12-well plates. One day later, cells were incubated with 80000 $TCID_{50}$ units of ZIKV or with 50 PFU of HSV-1 for one day to match the infection doses used in organoids. An equivalent volume of MOCK medium was used for control conditions.

Interferon and poly(I:C) treatments

Recombinant human interferons were reconstituted at 10 µg/ml according to the manufacturer's instructions. Interferons were used at 10 ng/ml dose unless differently specified. Based on the biological activities provided by the manufacturer, 10 ng/ml dose of IFN$\alpha 2$ and IFNβ corresponds to activities of 1800 U/ml and 100 U/ml respectively. BSA solution (0.1%) was used as a vehicle for untreated conditions. For multiple-dose treatments, interferons or vehicle were freshly diluted into culture medium at 2, 4, 6 and 8 dpi. For poly(I:C) experiments, organoids (10-12 days-old) were transfected with 1 µg poly(I:C) diluted in 200 µl of Neural Induction Medium [corresponding to 5 µg/ml poly(I:C)] using Lipofectamine 3000 following manufacturer's instructions and incubated at 37°C in a 5% CO_2 humidified atmosphere for one day. For poly(I:C) treatment in 2D culture, cells were seeded onto glass coverslips in 12-well plates. One day later, cells were transfected with 25 ng/ml poly(I:C) using Lipofectamine 3000 Transfection Reagent. The medium

was replaced after 6 hours and cells were further cultured at 37°C in a 5% CO_2 incubator for additional 18 hours. poly(I:C) was replaced with water in control transfections.

Cryo-sectioning, immunostaining and imaging

Organoids were fixed in 4% paraformaldehyde (PFA) overnight at 4°C. After extensive washes with PBS, organoids were immersed in 30% sucrose solution overnight, embedded in 10% gelatin solution and frozen. Samples were sectioned at 20 μm thickness using a cryostat (Leica). Organoid cryo-sections were fixed with 4% PFA for 10 minutes. After extensive washing with PBS, cryo-sections were permeabilized and blocked with blocking solution [10% normal donkey serum (NDS) containing 0.5% Triton X-100] for 45 min at room temperature. Sections were then incubated with primary antibodies diluted in antibody solution [10% normal donkey serum containing 0.1% Triton X-100] overnight at 4°C. After three washes of 10 min with PBS, both sections were incubated with secondary antibodies diluted in antibody solution at room temperature for two hours and with DAPI solution (2 μg/ml) for 10 minutes. For immunostaining of 2D cultures, cells seeded on coverslips were fixed with 4% PFA for 30 minutes and washed extensively with PBS. Cells were permeabilized with PBS supplemented with 0.2% Triton X-100 for 5 min, washed with PBS and blocked with 10% NDS for one hour. Coverslips were then incubated with primary antibodies diluted in antibody solution for 2 hours at room temperature. Coverslips were washed with PBS and incubated with secondary antibodies for 45 minutes at room temperature, followed by incubation with DAPI solution for 3 minutes. Finally, both organoid sections and coverslips were washed three times with PBS containing 0.05% Triton X-100 and then mounted in fluorescent mounting medium. Primary antibodies used in this study and their dilutions are summarized in the Key Resource Table. Secondary antibodies AlexaFluor 488, 568 or 647 -conjugated donkey antibodies (Invitrogen) were used at 1:500 dilution. Immunostaining images were captured with Axio Imager confocal microscopes LSM700, 780 and 880 (Zeiss GmbH), using the “tile” and “stitching” functions in the Zen software when imaging large organoid areas. Immunostaining images of organoids in Figure 7 were acquired with an Axio Imager.Z2 microscope (Zeiss GmbH) equipped with an ORCA-Flash 4.0 V3 Digital CMOS Camera (Hamamatsu). Bright-field imaging of intact organoids was performed on a widefield microscope (AxioVert.A1, Zeiss GmbH) with a SONY Chameleon®3 CM3-U3-31S4M CMOS camera (Zeiss GmbH). Post-acquisition image adjustments and quantifications were done in Fiji.

Quantification of cytokine levels by ELISA

Levels of all IFNα species and IFNβ in organoid supernatants were measured using ELISA Kits according to manufacturer’s instruction. Briefly, frozen supernatants from MOCK- and infected-organoids were thawed on ice and centrifuged at 13,000 rpm for 10 min to eliminate debris.

Supernatants (3 ml for each sample) from three different experiments were concentrated using Centrifugal Filter Unit with Ultracel-3 membranes (UFC900308 Merck Millipore). For each sample (50 μl) absorbance at 450 nm and 540 nm were measured in duplicate using a microplate reader (Synergy H1 BioTek). Absorbance at 540 nm was subtracted from absorbance at 450 nm to correct for non-specific signals. Mean values of absorbance were multiplied for the concentration factor and used to estimate cytokine amounts (pg/ml) according to a standard curve of recombinant Human IFNα (0-125 pg/ml) or recombinant Human IFNβ (0-150 pg/ml).

RNA extraction and RT-qPCR analysis

For each condition and time point, 4–10 organoids were pooled into RNAse-free tubes and chilled on ice. Organoids were washed with PρBS and incubated with 1 ml of chilled Cell Recovery Solution for 1 hour on ice. Dissolved Matrigel was removed by rinsing twice in cold DEPC-treated PBS and samples were lysed in RLT buffer. RNA was extracted using the RNeasy Micro Kit and on-column DNAse digestion was performed using RNAse-Free DNAse I following the manufacturer's protocol. cDNA synthesis was performed with SuperScript III and Random Hexamers using 500 ηg- 1 μg of total RNA according to the manufacturer's instructions. qPCR reactions were performed using GoTaq qPCR master mix on 384-well (CXF384) or 96-well (CXF96) BioRad machines using the following reaction protocol: (i) 95 °C for 3 min, (ii) 95°C for 10 s, (iii) 62°C for 10 s, (iv) 72°C for 40 s, (v) go to 2, 40 cycles, (vi) 95°C for 1 min, and (vii) 50°C for 10 s. Quantification was performed in Excel by calculating the ΔCt value using TBP as a reference gene and the ΔΔCt value using age-matched untreated samples as calibrators. ACTIN was used as a reference gene in HSV-1 experiments. Data are presented as expression ($2^{-\Delta Ct}$) or fold change ($2^{-\Delta\Delta Ct}$). Primers used for RT-qPCR are provided in Table S4.

RNA-sequencing and analysis

For the ZIKV experiment, 3 replicates were used per condition and time point (4 and 12 dpi). For the HSV-1 experiment, 3 replicates were used per each condition and time point (4 and 8 days post-infection). Sample collection and RNA isolation were performed as described above. RNA concentration and quality were assessed with an RNA 6000 Nano Chip (Agilent Technologies). mRNA isolation was performed with NEBNext Poly(A) mRNA Magnetic Isolation Module. Barcoded samples were multiplexed and sequenced 50 bp single-end on a HighSeq 2500 (Illumina). mRNA sample isolation, library preparation, and sequencing were done at the VBCF NGS Unit (https://www.vbcf.ac.at). Reads were screened for ribosomal RNA by aligning with BWA (v0.7.12) (H. Li and Durbin, 2009) against known rRNA sequences (RefSeq). rRNA-subtracted reads were aligned with TopHat (D. Kim et al., 2013) against the Homo sapiens genome (hg38).

Microexon-search was enabled. Additionally, a gene model was provided as GTF (UCSC, 2015_01, hg38). rRNA loci were masked on the genome for downstream analysis. Aligned reads were counted with HTSeq (v0.6.1; intersection-nonempty) (Anders et al., 2015). The samples were subjected to differential expression analysis with DESeq2 (v1.16.1) (Love et al., 2014). Furthermore, reads were subjected to TPM estimation with Kallisto (v0.43.0) (Bray et al., 2016). Unless differently specified, analysis was performed on the DESeq2 datasets filtered for TPM values >10, log2 Fold change absolute value of ≥1 and adjusted p-value < 0.05. Gene Ontology (GO) enrichment analysis was performed with Gene Ontology Consortium using the PANTHER classification system (Mi et al., 2013). Highly connected clusters were identified with ClusterONE plug-in for Cytoscape (Nepusz et al., 2012). Transcription factor enrichment analysis was performed with ChEA3 (Keenan et al., 2019). Motif analysis was performed with HOMER Software v4.10 on promoter sequences of input genes from 500 bp upstream and 100 bp downstream of the transcription start site (Heinz et al., 2010). For the analysis shown in Figure 6J, reads were aligned to the HSV-1 strain F complete genome (GeneBank GU734771) with Bowtie2 (v2.2.9) (Langmead and Salzberg, 2012) and further processed as described above. For heatmaps shown in Figure 5-6, only the late time points were included in the analysis and processed for DESeq2 analysis as described above. Principal component analysis on these samples was carried out with the top 1000 variable genes based on VST. Uncertainty of hierarchical clustering on the DESeq2 datasets was assessed with pvclust (Suzuki and Shimodaira, 2006). For data shown in Figure S6H, the comparison of ZIKV and HSV datasets (each a separate experiment = batch) was performed by DESeq2 with batch correction (~batch+condition). Variance-stabilizing transformations (VSTs) were batch corrected by limma with the design (~batch+condition) (Ritchie et al., 2015) and analysis was performed on genes with abs(log2FC)>1.

Quantification of apoptosis

To calculate the percentage of apoptotic cells, organoid cryosections immunostained with cleaved-caspase-3 (CC3) and DAPI were imaged under a confocal microscope. Random cortical structures on the surface of organoids were selected for quantification. The number of cells positive for CC3 in single z-plane images was counted manually using Fiji software. The total number of cells labeled by DAPI was estimated using the Fiji Plug-In GranFilter (using radius value set to 3 and step value set to 2) and watershed filter. The percentage of apoptosis is represented by the number of CC3+ cells divided by the total cell number labeled by DAPI.

Quantification of Sox1 levels

Organoid cryo-sections immunostained with Sox1 were imaged under a confocal microscope. Entire organoid sections were acquired using the "tile" and "stitching" functions in the Zen software (Zeiss). Single z-plane 8-bit images were used for quantification. Intensity (as mean gray value) of Sox1+ nuclei was measured using Fiji.

Quantification of IFN>GFP and ISRE>tdTomato positive cells

Organoid cryo-sections were immunostained with GFP and tdTomato antibodies and imaged under a confocal microscope using the "tile" and "stitching" functions in the Zen software (Zeiss). The total number of cells labeled by DAPI was estimated using the Fiji Plug-In GranFilter (using radius value set to 3 and step value set to 2) and watershed filter. Cells with high GFP signal were manually scored as IFN>GFP positive. Intensity (as mean gray value) of tdTomato signals was measured using Fiji and cells with tdTomato signal higher than the background intensity were scored as positive. Cells were scored to be within or outside the communication domain (200 μm in size) of a given IFN>GFP+ cell, a domain size compatible with paracrine signaling (Francis and Palsson, 1997).

PCR on viral nucleic acids

Viral nucleic acids were isolated from viral stocks using Purelink Viral RNA/DNA Mini Kit. PCR primer sequences are provided in the Key Resource Table. PCR amplification for TK was performed with GoTaq polymerase using the following program: 40 cycles of 30 sec at 95°C, 30 sec at 60°C, 1 min and 30 sec at 72°C, with an additional incubation of 5 min at 72°C. Due to the high GC content of the ICP34.5 target sequence and the failure of amplification by GoTaq polymerase-based approaches, PCR amplification of ICP34.5 was performed with KOD Xtreme Hot Start DNA polymerase. The program consisted of 2 min at 94°C, followed by 30 cycles of 30 sec at 98°C, 1 min at 60°C and 1 min at 68°C. PCR reactions were resolved on 1.25% agarose gels.

QUANTIFICATION AND STATISTICAL ANALYSIS

Statistical analysis was carried out with Prism software using unpaired *t*-test for comparison of two groups and ANOVA for comparisons of multiple groups. For non-normal distributions, non-parametric tests were used. The threshold for statistical significance was $p<0.05$. All details on sample size, the number of replicates, statistical tests and *p* values for each experiment are provided in the relevant figure, its legend or in Table S2. Unless differently specified in the figure legend, n refers to the number of replicates. Sample sizes of organoid experiments were estimated empirically based on previous experience. Organoids from the same batch were

962 randomly allocated to different treatment groups during the first day of the experiment. Analyses
963 were not performed blindly because of the substantial visual difference among groups.
964

REFERENCES

Aho, V., Myllys, M., Ruokolainen, V., Hakanen, S., Mäntylä, E., Virtanen, J., Hukkanen, V., Kühn, T., Timonen, J., Mattila, K., Larabell, C.A., Vihinen-Ranta, M., 2017. Chromatin organization regulates viral egress dynamics. Sci Rep 7, 3692.

Amin, N.D., Paşca, S.P., 2018. Building Models of Brain Disorders with Three-Dimensional Organoids. Neuron 100, 389–405.

Anders, S., Pyl, P.T., Huber, W., 2015. HTSeq--a Python framework to work with high-throughput sequencing data. Bioinformatics 31, 166–169.

Arao, Y., Ando, Y., Narita, M., Kurata, T., 1997. Unexpected correlation in the sensitivity of 19 herpes simplex virus strains to types I and II interferons. Journal of Interferon & Cytokine Research 17, 537–541.

Bagley, J.A., Reumann, D., Bian, S., Lévi-Strauss, J., Knoblich, J.A., 2017. Fused cerebral organoids model interactions between brain regions. Nat Meth 14, 743–751.

Baker, B.M., Chen, C.S., 2012. Deconstructing the third dimension: how 3D culture microenvironments alter cellular cues. Journal of Cell Science 125, 3015–3024.

Bale, J.F., Murph, J.R., 1992. Congenital Infections and the Nervous System. Pediatric Neurology 39, 669–690.

Bolen, C.R., Ding, S., Robek, M.D., Kleinstein, S.H., 2014. Dynamic expression profiling of type I and type III interferon-stimulated hepatocytes reveals a stable hierarchy of gene expression. Hepatology 59, 1262–1272.

Bolovan, C.A., Sawtell, N.M., Thompson, R.L., 1994. ICP34.5 mutants of herpes simplex virus type 1 strain 17syn+ are attenuated for neurovirulence in mice and for replication in confluent primary mouse embryo cell cultures. J. Virol. 68, 48–55.

Bower, J.R., Mao, H., Durishin, C., Rozenbom, E., Detwiler, M., Rempinski, D., Karban, T.L., Rosenthal, K.S., 1999. Intrastrain variants of herpes simplex virus type 1 isolated from a neonate with fatal disseminated infection differ in the ICP34.5 gene, glycoprotein processing, and neuroinvasiveness. J. Virol. 73, 3843–3853.

Brasil, P., Pereira, J.P., Raja Gabaglia, C., Damasceno, L., Wakimoto, M., Ribeiro Nogueira, R.M., Carvalho de Sequeira, P., Machado Siqueira, A., Abreu de Carvalho, L.M., Cotrim da Cunha, D., Calvet, G.A., Neves, E.S., Moreira, M.E., Rodrigues Baião, A.E., Nassar de Carvalho, P.R., Janzen, C., Valderramos, S.G., Cherry, J.D., Bispo de Filippis, A.M., Nielsen-Saines, K., 2016. Zika Virus Infection in Pregnant Women in Rio de Janeiro - Preliminary Report. N. Engl. J. Med. NEJMoa1602412.

Bray, N.L., Pimentel, H., Melsted, P., Pachter, L., 2016. Near-optimal probabilistic RNA-seq quantification. Nat. Biotechnol. 34, 525–527.

Brown, R.M., Rana, P.S.J.B., Jaeger, H.K., O'Dowd, J.M., Balemba, O.B., Fortunato, E.A., 2019. Human Cytomegalovirus Compromises Development of Cerebral Organoids. J. Virol. JVI.00957–19.

Burgess, D.J., 2019. Spatial transcriptomics coming of age. Nat. Rev. Genet. 20, 317–317.

Cairns, D.M., Rouleau, N., Parker, R.N., Walsh, K.G., Gehrke, L., Kaplan, D.L., 2020. A 3D human brain-like tissue model of herpes-induced Alzheimer's disease. Sci Adv 6, eaay8828.

Calistri, A., Parolin, C., Palù, G., 2003. Herpes simplex virus type 1 can either suppress or enhance human immunodeficiency virus type 1 replication in CD4-positive T lymphocytes. J. Med. Virol. 70, 163–170.

Carr, D.J.J., Al-khatib, K., James, C.M., Silverman, R., 2003. Interferon-beta suppresses herpes simplex virus type 1 replication in trigeminal ganglion cells through an RNase L-dependent pathway. J. Neuroimmunol. 141, 40–46.

Carver, E.A., Jiang, R., Lan, Y., Oram, K.F., Gridley, T., 2001. The mouse snail gene encodes a key regulator of the epithelial-mesenchymal transition. Mol. Cell. Biol. 21, 8184–8188.

Cheeran, M.C.-J., Lokensgard, J.R., Schleiss, M.R., 2009. Neuropathogenesis of congenital cytomegalovirus infection: disease mechanisms and prospects for intervention. Clin. Microbiol. Rev. 22, 99–126– Table of Contents.

Chenn, A., Walsh, C.A., 2002. Regulation of cerebral cortical size by control of cell cycle exit in neural precursors. Science 297, 365–369.

Chou, J., Chen, J.J., Gross, M., Roizman, B., 1995. Association of a M(r) 90,000 phosphoprotein with protein kinase PKR in cells exhibiting enhanced phosphorylation of translation initiation factor eIF-2 alpha and premature shutoff of protein synthesis after infection with gamma 134.5- mutants of herpes simplex virus 1. Proc Natl Acad Sci USA 92, 10516–10520.

Chou, J., Kern, E.R., Whitley, R.J., Roizman, B., 1990. Mapping of herpes simplex virus-1 neurovirulence to gamma 134.5, a gene nonessential for growth in culture. Science 250, 1262–1266.
Chucair-Elliott, A.J., Conrady, C., Zheng, M., Kroll, C.M., Lane, T.E., Carr, D.J.J., 2014. Microglia-induced IL-6 protects against neuronal loss following HSV-1 infection of neural progenitor cells. Glia 62, 1418–1434.
Contreras, D., Arumugaswami, V., 2016. Zika Virus Infectious Cell Culture System and the In Vitro Prophylactic Effect of Interferons. J Vis Exp.
Coyne, C.B., Lazear, H.M., 2016. Zika virus - reigniting the TORCH. Nat. Rev. Microbiol. 14, 707–715.
Cugola, F.R., Fernandes, I.R., Russo, F.B., Freitas, B.C., Dias, J.L.M., Guimarães, K.P., Benazzato, C., Almeida, N., Pignatari, G.C., Romero, S., Polonio, C.M., Cunha, I., Freitas, C.L., Brandão, W.N., Rossato, C., Andrade, D.G., de P Faria, D., Garcez, A.T., Buchpigel, C.A., Braconi, C.T., Mendes, E., Sall, A.A., de A Zanotto, P.M., Peron, J.P.S., Muotri, A.R., Beltrão-Braga, P.C.B., 2016. The Brazilian Zika virus strain causes birth defects in experimental models. Nature 1–15.
Danastas, K., Miranda-Saksena, M., Cunningham, A.L., 2020. Herpes Simplex Virus Type 1 Interactions with the Interferon System. Int J Mol Sci 21, 5150.
Dang, J., Tiwari, S.K., Lichinchi, G., Qin, Y., Patil, V.S., Eroshkin, A.M., Rana, T.M., 2016. Zika Virus Depletes Neural Progenitors in Human Cerebral Organoids through Activation of the Innate Immune Receptor TLR3. Cell Stem Cell.
Di Lullo, E., Kriegstein, A.R., 2017. The use of brain organoids to investigate neural development and disease. Nat Rev Neurosci 18, 573–584.
Drayman, N., Patel, P., Vistain, L., Tay, S., 2019. HSV-1 single-cell analysis reveals the activation of anti-viral and developmental programs in distinct sub-populations. Elife 8, 2503.
Duval, K., Grover, H., Han, L.-H., Mou, Y., Pegoraro, A.F., Fredberg, J., Chen, Z., 2017. Modeling Physiological Events in 2D vs. 3D Cell Culture. Physiology (Bethesda) 32, 266–277.
Ferenczy, M.W., DeLuca, N.A., 2009. Epigenetic modulation of gene expression from quiescent herpes simplex virus genomes. J. Virol. 83, 8514–8524.
Ferraris, P., Cochet, M., Hamel, R., Gladwyn-Ng, I., Alfano, C., Diop, F., Garcia, D., Talignani, L., Montero-Menei, C.N., Nougairède, A., Yssel, H., Nguyen, L., Coulpier, M., Missé, D., 2019. Zika virus differentially infects human neural progenitor cells according to their state of differentiation and dysregulates neurogenesis through the Notch pathway. Emerg Microbes Infect 8, 1003–1016.
Francis, K., Palsson, B.O., 1997. Effective intercellular communication distances are determined by the relative time constants for cyto/chemokine secretion and diffusion. Proc Natl Acad Sci USA 94, 12258–12262.
Fritz-French, C., Tyor, W., 2012. Interferon-α (IFNα) neurotoxicity. Cytokine Growth Factor Rev. 23, 7–14.
Gabriel, E., Ramani, A., Karow, U., Gottardo, M., Natarajan, K., Gooi, L.M., Goranci-Buzhala, G., Krut, O., Peters, F., Nikolic, M., Kuivanen, S., Korhonen, E., Smura, T., Vapalahti, O., Papantonis, A., Schmidt-Chanasit, J., Riparbelli, M., Callaini, G., Krönke, M., Utermöhlen, O., Gopalakrishnan, J., 2017. Recent Zika Virus Isolates Induce Premature Differentiation of Neural Progenitors in Human Brain Organoids. Cell Stem Cell.
Garcez, P.P., Loiola, E.C., Madeiro da Costa, R., Higa, L.M., Trindade, P., Delvecchio, R., Nascimento, J.M., Brindeiro, R., Tanuri, A., Rehen, S.K., 2016. Zika virus impairs growth in human neurospheres and brain organoids. Science 352, 816–818.
Giraldo, D., Wilcox, D.R., Longnecker, R., 2020. The Innate Immune Response to Herpes Simplex Virus 1 Infection Is Dampened in the Newborn Brain and Can Be Modulated by Exogenous Interferon Beta To Improve Survival. mBio 11.
Gladwyn-Ng, I., Cordón-Barris, L., Alfano, C., Creppe, C., Couderc, T., Morelli, G., Thelen, N., America, M., Bessières, B., Encha-Razavi, F., Bonnière, M., Suzuki, I.K., Flamand, M., Vanderhaeghen, P., Thiry, M., Lecuit, M., Nguyen, L., 2018. Stress-induced unfolded protein response contributes to Zika virus-associated microcephaly. Nat Neurosci 21, 63–71.
Gobillot, T.A., Humes, D., Sharma, A., Kikawa, C., Overbaugh, J., 2020. The Robust Restriction of Zika Virus by Type-I Interferon in A549 Cells Varies by Viral Lineage and Is Not Determined by IFITM3. Viruses 12, 503.
Gorman, M.J., Caine, E.A., Zaitsev, K., Begley, M.C., Weger-Lucarelli, J., Uccellini, M.B., Tripathi, S., Morrison, J., Yount, B.L., Dinnon, K.H., Rückert, C., Young, M.C., Zhu, Z., Robertson, S.J., McNally, K.L., Ye, J., Cao, B., Mysorekar, I.U., Ebel, G.D., Baric, R.S., Best, S.M., Artyomov, M.N., García-

Sastre, A., Diamond, M.S., 2018. An Immunocompetent Mouse Model of Zika Virus Infection. Cell Host Microbe 23, 672–685.e6.
Gottfried, C., Bambini-Junior, V., Francis, F., Riesgo, R., Savino, W., 2015. The Impact of Neuroimmune Alterations in Autism Spectrum Disorder. Front Psychiatry 6, 121.
Grant, A., Ponia, S.S., Tripathi, S., Balasubramaniam, V., Miorin, L., Sourisseau, M., Schwarz, M.C., Sánchez-Seco, M.P., Evans, M.J., Best, S.M., García-Sastre, A., 2016. Zika Virus Targets Human STAT2 to Inhibit Type I Interferon Signaling. Cell Host Microbe 19, 882–890.
Hamel, R., Dejarnac, O., Wichit, S., Ekchariyawat, P., Neyret, A., Luplertlop, N., Perera-Lecoin, M., Surasombatpattana, P., Talignani, L., Thomas, F., Cao-Lormeau, V.-M., Choumet, V., Briant, L., Desprès, P., Amara, A., Yssel, H., Missé, D., 2015. Biology of Zika Virus Infection in Human Skin Cells. J. Virol. 89, 8880–8896.
Hanners, N.W., Eitson, J.L., Usui, N., Richardson, R.B., Wexler, E.M., Konopka, G., Schoggins, J.W., 2016. Western Zika Virus in Human Fetal Neural Progenitors Persists Long Term with Partial Cytopathic and Limited Immunogenic Effects. CellReports 15, 2315–2322.
Hatakeyama, J., Wakamatsu, Y., Nagafuchi, A., Kageyama, R., Shigemoto, R., Shimamura, K., 2014. Cadherin-based adhesions in the apical endfoot are required for active Notch signaling to control neurogenesis in vertebrates. Development 141, 1671–1682.
Härle, P., Cull, V., Guo, L., Papin, J., Lawson, C., Carr, D.J.J., 2002. Transient transfection of mouse fibroblasts with type I interferon transgenes provides various degrees of protection against herpes simplex virus infection. Antiviral Res. 56, 39–49.
Härle, P., Lauret, E., Pitha, P.M., De Maeyer, E., Carr, D.J., 2001. Expression of human and macaque type I IFN transgenes interferes with HSV-1 replication at the transcriptional and translational levels: IFN-beta is more potent than IFN-alpha 2. Virology 290, 237–248.
He, B., Gross, M., Roizman, B., 1997. The gamma(1)34.5 protein of herpes simplex virus 1 complexes with protein phosphatase 1alpha to dephosphorylate the alpha subunit of the eukaryotic translation initiation factor 2 and preclude the shutoff of protein synthesis by double-stranded RNA-activated protein kinase. Proc Natl Acad Sci USA 94, 843–848.
Heinz, S., Benner, C., Spann, N., Bertolino, E., Lin, Y.C., Laslo, P., Cheng, J.X., Murre, C., Singh, H., Glass, C.K., 2010. Simple combinations of lineage-determining transcription factors prime cis-regulatory elements required for macrophage and B cell identities. Molecular Cell 38, 576–589.
Hensel, N., Raker, V., Förthmann, B., Detering, N.T., Kubinski, S., Buch, A., Katzilieris-Petras, G., Spanier, J., Gudi, V., Wagenknecht, S., Kopfnagel, V., Werfel, T.A., Stangel, M., Beineke, A., Kalinke, U., Paludan, S.R., Sodeik, B., Claus, P., 2019. HSV-1 triggers paracrine fibroblast growth factor response from cortical brain cells via immediate-early protein ICP0. Journal of Neuroinflammation 16, 248–15.
Herber, S., Silva, A.A., Sanseverino, M.T.V., Friedrich, L., Ranieri, T.M.S., Favreto, C., Fraga, L.R., Terra, A.P., Schwartz, I.V.D., Schuler-Faccini, L., 2019. Prevalence and causes of congenital microcephaly in the absence of a Zika virus outbreak in southern Brazil. J Pediatr (Rio J) 95, 600–606.
Herring, J.A., Elison, W.S., Tessem, J.S., 2019. Function of Nr4a Orphan Nuclear Receptors in Proliferation, Apoptosis and Fuel Utilization Across Tissues. Cells 8, 1373.
Hess, J., Angel, P., Schorpp-Kistner, M., 2004. AP-1 subunits: quarrel and harmony among siblings. Journal of Cell Science 117, 5965–5973.
Honda, K., Taniguchi, T., 2006. IRFs: master regulators of signalling by Toll-like receptors and cytosolic pattern-recognition receptors. Nat. Rev. Immunol. 6, 644–658.
Honein, M.A., Dawson, A.L., Petersen, E.E., Jones, A.M., Lee, E.H., Yazdy, M.M., Ahmad, N., Macdonald, J., Evert, N., Bingham, A., Ellington, S.R., Shapiro-Mendoza, C.K., Oduyebo, T., Fine, A.D., Brown, C.M., Sommer, J.N., Gupta, J., Cavicchia, P., Slavinski, S., White, J.L., Owen, S.M., Petersen, L.R., Boyle, C., Meaney-Delman, D., Jamieson, D.J., US Zika Pregnancy Registry Collaboration, 2017. Birth Defects Among Fetuses and Infants of US Women With Evidence of Possible Zika Virus Infection During Pregnancy. JAMA 317, 59–68.
Hu, B., Li, X., Huo, Y., Yu, Y., Zhang, Q., Chen, G., Zhang, Y., Fraser, N.W., Wu, D., Zhou, J., 2016. Cellular responses to HSV-1 infection are linked to specific types of alterations in the host transcriptome. Sci Rep 6, 28075–14.
Hummer, B.T., Li, X.L., Hassel, B.A., 2001. Role for p53 in gene induction by double-stranded RNA. J. Virol. 75, 7774–7777.
Ivashkiv, L.B., Donlin, L.T., 2014. Regulation of type I interferon responses. Nat. Rev. Immunol. 14, 36–49.

Kadowaki, M., Nakamura, S., Machon, O., Krauss, S., Radice, G.L., Takeichi, M., 2007. N-cadherin mediates cortical organization in the mouse brain. Dev. Biol. 304, 22–33.
Kanton, S., Boyle, M.J., He, Z., Santel, M., Weigert, A., Sanchís-Calleja, F., Guijarro, P., Sidow, L., Fleck, J.S., Han, D., Qian, Z., Heide, M., Huttner, W.B., Khaitovich, P., Pääbo, S., Treutlein, B., Camp, J.G., 2019. Organoid single-cell genomic atlas uncovers human-specific features of brain development. Nature 574, 418–422.
Kasmapour, B., Kubsch, T., Rand, U., Eiz-Vesper, B., Messerle, M., Vondran, F.W.R., Wiegmann, B., Haverich, A., Cicin-Sain, L., 2018. Myeloid Dendritic Cells Repress Human Cytomegalovirus Gene Expression and Spread by Releasing Interferon-Unrelated Soluble Antiviral Factors. J. Virol. 92, 795.
Kaur, B., Chiocca, E.A., Cripe, T.P., 2012. Oncolytic HSV-1 virotherapy: clinical experience and opportunities for progress. Curr Pharm Biotechnol 13, 1842–1851.
Keenan, A.B., Torre, D., Lachmann, A., Leong, A.K., Wojciechowicz, M.L., Utti, V., Jagodnik, K.M., Kropiwnicki, E., Wang, Z., Ma'ayan, A., 2019. ChEA3: transcription factor enrichment analysis by orthogonal omics integration. Nucleic Acids Res. 47, W212–W224.
Keniry, M., Dearth, R.K., Persans, M., Parsons, R., 2014. New Frontiers for the NFIL3 bZIP Transcription Factor in Cancer, Metabolism and Beyond. Discoveries (Craiova) 2, e15.
Kim, D., Pertea, G., Trapnell, C., Pimentel, H., Kelley, R., Salzberg, S.L., 2013. TopHat2: accurate alignment of transcriptomes in the presence of insertions, deletions and gene fusions. Genome Biol. 14, R36.
Kim, J., Koo, B.-K., Yoon, K.-J., 2019. Modeling Host-Virus Interactions in Viral Infectious Diseases Using Stem-Cell-Derived Systems and CRISPR/Cas9 Technology. Viruses 11, 124.
Krummenacher, C., Baribaud, I., Eisenberg, R.J., Cohen, G.H., 2003. Cellular localization of nectin-1 and glycoprotein D during herpes simplex virus infection. J. Virol. 77, 8985–8999.
Kumar, A., Hou, S., Airo, A.M., Limonta, D., Mancinelli, V., Branton, W., Power, C., Hobman, T.C., 2016. Zika virus inhibits type-I interferon production and downstream signaling. EMBO Rep. 17, 1766–1775.
Lafaille, F.G., Pessach, I.M., Zhang, S.-Y., Ciancanelli, M.J., Herman, M., Abhyankar, A., Ying, S.-W., Keros, S., Goldstein, P.A., Mostoslavsky, G., Ordovas-Montanes, J., Jouanguy, E., Plancoulaine, S., Tu, E., Elkabetz, Y., Al-Muhsen, S., Tardieu, M., Schlaeger, T.M., Daley, G.Q., Abel, L., Casanova, J.-L., Studer, L., Notarangelo, L.D., 2012. Impaired intrinsic immunity to HSV-1 in human iPSC-derived TLR3-deficient CNS cells. Nature 491, 769–773.
Lancaster, M.A., Knoblich, J.A., 2014. Generation of cerebral organoids from human pluripotent stem cells. Nat Protoc 9, 2329–2340.
Lancaster, M.A., Renner, M., Martin, C.-A., Wenzel, D., Bicknell, L.S., Hurles, M.E., Homfray, T., Penninger, J.M., Jackson, A.P., Knoblich, J.A., 2013. Cerebral organoids model human brain development and microcephaly. Nature 501, 373–379.
Lanciotti, R.S., Kosoy, O.L., Laven, J.J., Velez, J.O., Lambert, A.J., Johnson, A.J., Stanfield, S.M., Duffy, M.R., 2008. Genetic and serologic properties of Zika virus associated with an epidemic, Yap State, Micronesia, 2007. Emerging Infect. Dis. 14, 1232–1239.
Langmead, B., Salzberg, S.L., 2012. Fast gapped-read alignment with Bowtie 2. Nat Meth 9, 357–359.
Leib, D.A., Harrison, T.E., Laslo, K.M., Machalek, M.A., Moorman, N.J., Virgin, H.W., 1999. Interferons regulate the phenotype of wild-type and mutant herpes simplex viruses in vivo. J. Exp. Med. 189, 663–672.
Li, C., Deng, Y.-Q., Wang, S., Ma, F., Aliyari, R., Huang, X.-Y., Zhang, N.-N., Watanabe, M., Dong, H.-L., Liu, P., Li, X.-F., Ye, Q., Tian, M., Hong, S., Fan, J., Zhao, H., Li, L., Vishlaghi, N., Buth, J.E., Au, C., Liu, Y., Lu, N., Du, P., Qin, F.X.-F., Zhang, B., Gong, D., Dai, X., Sun, R., Novitch, B.G., Xu, Z., Qin, C.-F., Cheng, G., 2017. 25-Hydroxycholesterol Protects Host against Zika Virus Infection and Its Associated Microcephaly in a Mouse Model. Immunity 46, 446–456.
Li, C., Xu, D., Ye, Q., Hong, S., Jiang, Y., Liu, X., Zhang, N., Shi, L., Qin, C.-F., Xu, Z., 2016. Zika Virus Disrupts Neural Progenitor Development and Leads to Microcephaly in Mice. Cell Stem Cell 19, 120–126.
Li, H., Durbin, R., 2009. Fast and accurate short read alignment with Burrows-Wheeler transform. Bioinformatics 25, 1754–1760.
Li, R.Y., Tsutsui, Y., 2000. Growth retardation and microcephaly induced in mice by placental infection with murine cytomegalovirus. Teratology 62, 79–85.

Li, S.-F., Gong, M.-J., Zhao, F.-R., Shao, J.-J., Xie, Y.-L., Zhang, Y.-G., Chang, H.-Y., 2018. Type I Interferons: Distinct Biological Activities and Current Applications for Viral Infection. Cell. Physiol. Biochem. 51, 2377–2396.

Lima, M.C., de Mendonça, L.R., Rezende, A.M., Carrera, R.M., Aníbal-Silva, C.E., Demers, M., D'Aiuto, L., Wood, J., Chowdari, K.V., Griffiths, M., Lucena-Araujo, A.R., Barral-Netto, M., Azevedo, E.A.N., Alves, R.W., Farias, P.C.S., Marques, E.T.A., Castanha, P.M.S., Donald, C.L., Kohl, A., Nimgaonkar, V.L., Franca, R.F.O., 2019. The Transcriptional and Protein Profile From Human Infected Neuroprogenitor Cells Is Strongly Correlated to Zika Virus Microcephaly Cytokines Phenotype Evidencing a Persistent Inflammation in the CNS. Front. Immunol. 10, 1928.

Lin, J.-Y., Kuo, R.-L., Huang, H.-I., 2019. Activation of type I interferon antiviral response in human neural stem cells. Stem Cell Res Ther 10, 387–17.

Liu, L., Chen, Z., Zhang, X., Li, S., Hui, Y., Feng, H., Du, Y., Jin, G., Zhou, X., Zhang, X., 2019. Protection of ZIKV infection-induced neuropathy by abrogation of acute antiviral response in human neural progenitors. Cell Death Differ. 16, e119.

Looker, K.J., Magaret, A.S., May, M.T., Turner, K.M.E., Vickerman, P., Newman, L.M., Gottlieb, S.L., 2017. First estimates of the global and regional incidence of neonatal herpes infection. The Lancet Global Health 5, e300–e309.

Love, M.I., Huber, W., Anders, S., 2014. Moderated estimation of fold change and dispersion for RNA-seq data with DESeq2. Genome Biol. 15, 550.

Marquez, L., Levy, M.L., Munoz, F.M., Palazzi, D.L., 2011. A report of three cases and review of intrauterine herpes simplex virus infection. Pediatr. Infect. Dis. J. 30, 153–157.

Marsico, C., Kimberlin, D.W., 2017. Congenital Cytomegalovirus infection: advances and challenges in diagnosis, prevention and treatment. Ital J Pediatr 43, 38–8.

Mi, H., Muruganujan, A., Casagrande, J.T., Thomas, P.D., 2013. Large-scale gene function analysis with the PANTHER classification system. Nat Protoc 8, 1551–1566.

Miller, J.A., Ding, S.-L., Sunkin, S.M., Smith, K.A., Ng, L., Szafer, A., Ebbert, A., Riley, Z.L., Royall, J.J., Aiona, K., Arnold, J.M., Bennet, C., Bertagnolli, D., Brouner, K., Butler, S., Caldejon, S., Carey, A., Cuhaciyan, C., Dalley, R.A., Dee, N., Dolbeare, T.A., Facer, B.A.C., Feng, D., Fliss, T.P., Gee, G., Goldy, J., Gourley, L., Gregor, B.W., Gu, G., Howard, R.E., Jochim, J.M., Kuan, C.L., Lau, C., Lee, C.-K., Lee, F., Lemon, T.A., Lesnar, P., McMurray, B., Mastan, N., Mosqueda, N., Naluai-Cecchini, T., Ngo, N.-K., Nyhus, J., Oldre, A., Olson, E., Parente, J., Parker, P.D., Parry, S.E., Stevens, A., Pletikos, M., Reding, M., Roll, K., Sandman, D., Sarreal, M., Shapouri, S., Shapovalova, N.V., Shen, E.H., Sjoquist, N., Slaughterbeck, C.R., Smith, M., Sodt, A.J., Williams, D., Zöllei, L., Fischl, B., Gerstein, M.B., Geschwind, D.H., Glass, I.A., Hawrylycz, M.J., Hevner, R.F., Huang, H., Jones, A.R., Knowles, J.A., Levitt, P., Phillips, J.W., Sestan, N., Wohnoutka, P., Dang, C., Bernard, A., Hohmann, J.G., Lein, E.S., 2014. Transcriptional landscape of the prenatal human brain. Nature 508, 199–206.

Ming, G.-L., Tang, H., Song, H., 2016. Advances in Zika Virus Research: Stem Cell Models, Challenges, and Opportunities. Cell Stem Cell 19, 690–702.

Mlakar, J., Korva, M., Tul, N., Popović, M., Poljšak-Prijatelj, M., Mraz, J., Kolenc, M., Resman Rus, K., Vesnaver Vipotnik, T., Fabjan Vodušek, V., Vizjak, A., Pižem, J., Petrovec, M., Avšič Županc, T., 2016. Zika Virus Associated with Microcephaly. N. Engl. J. Med. 160210140106006.

Nepusz, T., Yu, H., Paccanaro, A., 2012. Detecting overlapping protein complexes in protein-protein interaction networks. Nat Meth 9, 471–472.

Ng, C.T., Mendoza, J.L., Garcia, K.C., Oldstone, M.B.A., 2016. Alpha and Beta Type 1 Interferon Signaling: Passage for Diverse Biologic Outcomes. CELL 164, 349–352.

Paijo, J., Döring, M., Spanier, J., Grabski, E., Nooruzzaman, M., Schmidt, T., Witte, G., Messerle, M., Hornung, V., Kaever, V., Kalinke, U., 2016. cGAS Senses Human Cytomegalovirus and Induces Type I Interferon Responses in Human Monocyte-Derived Cells. PLoS Pathog. 12, e1005546.

Qi, Y., Zhang, X.-J., Renier, N., Wu, Z., Atkin, T., Sun, Z., Ozair, M.Z., Tchieu, J., Zimmer, B., Fattahi, F., Ganat, Y., Azevedo, R., Zeltner, N., Brivanlou, A.H., Karayiorgou, M., Gogos, J., Tomishima, M., Tessier-Lavigne, M., Shi, S.-H., Studer, L., 2017. Combined small-molecule inhibition accelerates the derivation of functional cortical neurons from human pluripotent stem cells. Nat. Biotechnol. 35, 154–163.

Qian, X., Nguyen, H.N., Song, M.M., Hadiono, C., Ogden, S.C., Hammack, C., Yao, B., Hamersky, G.R., Jacob, F., Zhong, C., Yoon, K.-J., Jeang, W., Lin, L., Li, Y., Thakor, J., Berg, D.A., Zhang, C., Kang, E., Chickering, M., Nauen, D., Ho, C.-Y., Wen, Z., Christian, K.M., Shi, P.-Y., Maher, B.J., Wu, H., Jin,

P., Tang, H., Song, H., Ming, G.-L., 2016. Brain-Region-Specific Organoids Using Mini- bioreactors for Modeling ZIKV Exposure. CELL 1–39.
Qiao, H., Guo, M., Shang, J., Zhao, W., Wang, Z., Liu, N., Li, B., Zhou, Y., Wu, Y., Chen, P., 2020. Herpes simplex virus type 1 infection leads to neurodevelopmental disorder-associated neuropathological changes. PLoS Pathog. 16, e1008899.
Reiss, K., Maretzky, T., Ludwig, A., Tousseyn, T., de Strooper, B., Hartmann, D., Saftig, P., 2005. ADAM10 cleavage of N-cadherin and regulation of cell-cell adhesion and beta-catenin nuclear signalling. EMBO J. 24, 742–752.
Richart, S.M., Simpson, S.A., Krummenacher, C., Whitbeck, J.C., Pizer, L.I., Cohen, G.H., Eisenberg, R.J., Wilcox, C.L., 2003. Entry of herpes simplex virus type 1 into primary sensory neurons in vitro is mediated by Nectin-1/HveC. J. Virol. 77, 3307–3311.
Rios, A.C., Clevers, H., 2018. Imaging organoids: a bright future ahead. Nat Meth 15, 24–26.
Ritchie, M.E., Phipson, B., Wu, D., Hu, Y., Law, C.W., Shi, W., Smyth, G.K., 2015. limma powers differential expression analyses for RNA-sequencing and microarray studies. Nucleic Acids Res. 43, e47–e47.
Rousso, D.L., Pearson, C.A., Gaber, Z.B., Miquelajauregui, A., Li, S., Portera-Cailliau, C., Morrisey, E.E., Novitch, B.G., 2012. Foxp-mediated suppression of N-cadherin regulates neuroepithelial character and progenitor maintenance in the CNS. Neuron 74, 314–330.
Sandler, N.G., Bosinger, S.E., Estes, J.D., Zhu, R.T.R., Tharp, G.K., Boritz, E., Levin, D., Wijeyesinghe, S., Makamdop, K.N., del Prete, G.Q., Hill, B.J., Timmer, J.K., Reiss, E., Yarden, G., Darko, S., Contijoch, E., Todd, J.P., Silvestri, G., Nason, M., Norgren, R.B., Keele, B.F., Rao, S., Langer, J.A., Lifson, J.D., Schreiber, G., Douek, D.C., 2014. Type I interferon responses in rhesus macaques prevent SIV infection and slow disease progression. Nature 511, 601–605.
Schneider, W.M., Chevillotte, M.D., Rice, C.M., 2014. Interferon-Stimulated Genes: A Complex Web of Host Defenses. Annu. Rev. Immunol. 32, 513–545.
Schwartz, D.A., 2017. The Origins and Emergence of Zika Virus, the Newest TORCH Infection: What's Old Is New Again. Arch. Pathol. Lab. Med. 141, 18–25.
Scuderi, S., Altobelli, G.G., Cimini, V., Coppola, G., Vaccarino, F.M., 2021. Cell-to-Cell Adhesion and Neurogenesis in Human Cortical Development: A Study Comparing 2D Monolayers with 3D Organoid Cultures. Stem Cell Reports 13, 265.
Simonin, Y., Loustalot, F., Desmetz, C., Foulongne, V., Constant, O., Fournier-Wirth, C., Leon, F., Molès, J.-P., Goubaud, A., Lemaitre, J.-M., Maquart, M., Leparc-Goffart, I., Briant, L., Nagot, N., Van de Perre, P., Salinas, S., 2016. Zika Virus Strains Potentially Display Different Infectious Profiles in Human Neural Cells. EBIOM 12, 161–169.
Simões-Costa, M., Bronner, M.E., 2015. Establishing neural crest identity: a gene regulatory recipe. Development 142, 242–257.
Simpson, S.A., Manchak, M.D., Hager, E.J., Krummenacher, C., Whitbeck, J.C., Levin, M.J., Freed, C.R., Wilcox, C.L., Cohen, G.H., Eisenberg, R.J., Pizer, L.I., 2005. Nectin-1/HveC Mediates herpes simplex virus type 1 entry into primary human sensory neurons and fibroblasts. J. Neurovirol. 11, 208–218.
Sison, S.L., O'Brien, B.S., Johnson, A.J., Seminary, E.R., Terhune, S.S., Ebert, A.D., 2019. Human Cytomegalovirus Disruption of Calcium Signaling in Neural Progenitor Cells and Organoids. J. Virol. JVI.00954–19.
Sorgeloos, F., Kreit, M., Hermant, P., Lardinois, C., Michiels, T., 2013. Antiviral type I and type III interferon responses in the central nervous system. Viruses 5, 834–857.
Souza, B.S.F., Sampaio, G.L.A., Pereira, C.S., Campos, G.S., Sardi, S.I., Freitas, L.A.R., Figueira, C.P., Paredes, B.D., Nonaka, C.K.V., Azevedo, C.M., Vinicius P. C. Rocha, Bandeira, A.C., Mendez-Otero, R., Santos, dos, R.R., Soares, M.B.P., 2016. Zika virus infection induces mitosis abnormalities and apoptotic cell death of human neural progenitor cells 1–13.
Sun, G., Chiuppesi, F., Chen, X., Wang, C., Tian, E., Nguyen, J., Kha, M., Trinh, D., Zhang, H., Marchetto, M.C., Song, H., Ming, G.-L., Gage, F.H., Diamond, D.J., Wussow, F., Shi, Y., 2020. Modeling Human Cytomegalovirus-Induced Microcephaly in Human iPSC-Derived Brain Organoids. Cell Reports Medicine 100002.
Suzuki, R., Shimodaira, H., 2006. Pvclust: an R package for assessing the uncertainty in hierarchical clustering. Bioinformatics 22, 1540–1542.
Thiery, J.P., Acloque, H., Huang, R.Y.J., Nieto, M.A., 2009. Epithelial-mesenchymal transitions in development and disease. CELL 139, 871–890.

Wang, J.P., Bowen, G.N., Zhou, S., Cerny, A., Zacharia, A., Knipe, D.M., Finberg, R.W., Kurt-Jones, E.A., 2012. Role of Specific Innate Immune Responses in Herpes Simplex Virus Infection of the Central Nervous System. J. Virol. 86, 2273–2281.

Wang, K., Mahalingam, G., Hoover, S.E., Mont, E.K., Holland, S.M., Cohen, J.I., Straus, S.E., 2007. Diverse herpes simplex virus type 1 thymidine kinase mutants in individual human neurons and Ganglia. J. Virol. 81, 6817–6826.

Watanabe, M., Buth, J.E., Vishlaghi, N., la Torre-Ubieta, de, L., Taxidis, J., Khakh, B.S., Coppola, G., Pearson, C.A., Yamauchi, K., Gong, D., Dai, X., Damoiseaux, R., Aliyari, R., Liebscher, S., Schenke-Layland, K., Caneda, C., Huang, E.J., Zhang, Y., Cheng, G., Geschwind, D.H., Golshani, P., Sun, R., Novitch, B.G., 2017. Self-Organized Cerebral Organoids with Human- Specific Features Predict Effective Drugs to Combat Zika Virus Infection. CellReports 21, 517–532.

Watanabe, Y., Someya, T., Nawa, H., 2010. Cytokine hypothesis of schizophrenia pathogenesis: evidence from human studies and animal models. Psychiatry Clin Neurosci 64, 217–230.

Zhang, F., Hammack, C., Ogden, S.C., Cheng, Y., Lee, E.M., Wen, Z., Qian, X., Nguyen, H.N., Li, Y., Yao, B., Xu, M., Xu, T., Chen, L., Wang, Z., Feng, H., Huang, W.-K., Yoon, K.-J., Shan, C., Huang, L., Qin, Z., Christian, K.M., Shi, P.-Y., Xu, M., Xia, M., Zheng, W., Wu, H., Song, H., Tang, H., Ming, G.-L., Jin, P., 2016. Molecular signatures associated with ZIKV exposure in human cortical neural progenitors. Nucleic Acids Res. 44, 8610–8620.

Zhao, M., Zhang, J., Phatnani, H., Scheu, S., Maniatis, T., 2012. Stochastic expression of the interferon-β gene. PLoS Biol. 10, e1001249.

Zika: the continuing threat, 2019. Zika: the continuing threat. Bull World Health Organ 97, 6–7.

KEY RESOURCES TABLE

REAGENT or RESOURCE	SOURCE	IDENTIFIER
Antibodies		
mouse anti-Flavivirus D1-4G2-4-15 (ZIKVA, 1:600)	Merck Millipore	Cat#MAB10216; RRID: AB_827205
rabbit anti-ZIKA virus Envelope protein (ZIKVE, 1:250)	Genetex	Cat#GTX133314; RRID: AB_2747413
rabbit anti-cleavedCaspase3 (1:500)	Cell Signaling	Cat#9661S; RRID: AB_2341188
goat anti-Sox1 (1:200)	R&D Systems	Cat#AF3369; RRID: AB_2239879
rabbit anti-Sox2 (1:1000)	Abcam	Cat#Ab97959; RRID: AB_2341193
goat anti-Sox2 (1:200)	R&D systems	Cat#AF2018; RRID: AB_355110
mouse anti-HSV1 ICP4 10F1 (1:500)	Abcam	Cat#ab6514; RRID: AB_305537
rabbit anti-HSV1 (1:500)	Abcam	Cat#ab9533; RRID: AB_307320
rabbit anti-IRF3 (D6I4C) XP (1:500)	Cell Signaling	Cat#11904; RRID: AB_2722521
mouse anti-STAT2 (1:100)	Santa Cruz Biotechnology	Cat#sc-1668; RRID: AB_628291
chicken anti-GFP (1:1000)	Aves laboratory	Cat#GFP-1020; RRID: AB_10000240
rabbit anti-tdTomato (1:500)	Clontech	Cat#632496; RRID: AB_10013483
goat anti-tdTomato (1:200)	Sicgen	Cat#AB8181-200; RRID: AB_2722750
mouse anti-N-Cadherin (1:200)	BD	Cat#610920; RRID: AB_2077527
rabbit anti-Nestin (1:1000)	Abcam	Cat#ab10538; RRID: AB_297279
sheep anti-Pax6 (1:200)	R&D systems	Cat#AF8150; RRID: AB_2827378
goat anti-SNAI1 (1:500)	Abcam	Cat#ab53519; RRID: AB_881666
rabbit anti-Beta 3 tubulin (1:750)	Covance	Cat#PRB-435P; RRID: AB_291637
mouse anti-mNeonGreen (1:200)	ChromoTek	Cat#32f6-100; RRID: AB_2827566
Bacterial and Virus Strains		
French Polynesian ZIKA virus, strain H/PF/2013, clinical isolate	EVAg project	Cat#001v-EVA1545
Herpes Simplex Virus (HSV-1), strain F	(Calistri et al., 2003)	N/A
Herpes Simplex Virus (HSV-1) R3616, strain F	(Chou et al., 1990)	N/A
Human Cytomegalovirus (HMCV) UL122/123-mNeonGreen, strain TB40/E	(Kasmapour et al., 2018)	N/A
Chemicals, Peptides, and Recombinant Proteins		
mTeSR1 complete Kit	Stem Cell Technologies	Cat#85875
Gelatin	Sigma-Aldrich	Cat#G1890; CAS: 9000-70-8

CF-1-γ-irradiated mouse embryonic fibroblasts	Global Stem	Cat#GSC-6001G
Matrigel® Basement Membrane Matrix	Corning	Cat#356235
hESC-qualified Matrigel	Corning	Cat#354277
bFGF	Peprotech	Cat#100-18B
Y-27632 Rock Inhibitor	Selleck Chemicals	Cat#S1049; CAS: 129830-38-2
Ultra-low attachment 96-well plates	Corning	Cat#COR7007
N2 supplement	Thermo Fischer Scientific	Cat#17502048;CAS: 17502-048
B27 supplement – Vitamin A	Thermo Fischer Scientific	Cat#12587010; CAS: 12587010
B27 supplement	Thermo Fischer Scientific	Cat#17504044; CAS: 17504-044
Beta-mercaptoethanol (BME)	Merck Millipore	Cat#805740; CAS: 60-24-2
Human Insulin solution	Sigma-Aldrich	Cat#I9278; CAS: 11061-68-0
Heparin sodium salt	Sigma-Aldrich	Cat#H3149; CAS: 9041-08-1
Accutase	Sigma-Aldrich	Cat#A6964
Collagenase type IV	Life Technologies	Cat#17104019 ; CAS: 17-104-019
Dispase	Invitrogen	Cat#17105-041; CAS: 42613-33-2
KnockOut Serum Replacement (KOSR)	Thermo Fisher Scientific	Cat#10828028; CAS: 10828-028
0.05% Trypsin/EDTA solution	Thermo Fisher Scientific	Cat#15400054; CAS: 15-400-054
GlutaMAX 100X	Thermo Fisher Scientific	Cat#35050-038
MEM-NEEA Solution 100X	Sigma-Aldrich	Cat#M7145
DMEM-F12	Gibco	Cat#11330-057
Neurobasal medium	Gibco	Cat#21103049
BDNF	Stem Cell Technologies	Cat#78005.3; CAS: 78005
GDNF	Stem Cell Technologies	Cat#78058.3; CAS: 78058
db-cAMP	MedChem Express	Cat#HY-B0764; CAS: 16980-89-5
Essential 6 medium	Thermo Fisher Scientific	Cat#A1516401
Poly-L-ornithine hydrobromide	Sigma-Aldrich	Cat#P3655; CAS: 27378-49-0
Laminin	Sigma-Aldrich	Cat#L2020; CAS: 114956-81-9
LDN193189	Sigma-Aldrich	Cat#SML0559; CAS: 1062368-24-4
SB431542	Stemgent	Cat#04-0010-10 CAS:381836-41-9
XAV939	Abcam	Cat#ab120897; CAS: 284028-89-3
SU5402	Sigma-Aldrich	Cat#SML0443 CAS: 215543-92-3

DAPT	Tocris	Cat#2634; CAS: 208255-80
DPBS, no calcium, no magnesium	Gibco	Cat#14190-169
DPBS, calcium, magnesium	Thermo Fischer Scientific	Cat#14040-174
Penicillin/Streptomycin	Sigma-Aldrich	Cat#P0781; CAS: 4744-08-5
EDTA solution	Sigma-Aldrich	Cat#E8008; CAS: 60-00-4
Puromycin	Jena Bioscience	Cat#NU-931-5; CAS: 1416561-90-4
G418	Invivogen	Cat#ant-gn-1; CAS: 108321-42-2
QuickExtract DNA Extraction Solution	EpiCentre	Cat#QE09050
Cell Recovery Solution	Corning	Cat#354253
SuperScript III	ThermoFisher	Cat#18080051; CAS: 18080-051
Human Recombinant IFNα2	Peprotech	Cat#300-02AA
Human Recombinant IFNβ	Peprotech	Cat#300-02BC
Human Recombinant IFNλ1	Peprotech	Cat#300-02K
Human Recombinant IFNλ2	Peprotech	Cat#300-02L
Bovine Serum Albumin (BSA)	Sigma-Aldrich	Cat#A7030; CAS: 9048-46-8
poly(I:C)-LMW	Invivogen	Cat#tlrl-picw; CAS: 31852-29-6
Lipofectamine 3000 Transfection reagent	Thermo Fisher Scientific	Cat#L3000001; CAS: L3000-001
Sucrose	Sigma-Aldrich	Cat#84097; CAS: 57-50-1
Normal Donkey Serum	EMD Millipore	Cat#S30-M
Paraformaldehyde	Sigma-Aldrich	Cat#441244; CAS: 30525-89-4
DAPI	Sigma-Aldrich	Cat#D9542; CAS: 28718-90-3
Fluorescent mounting medium	Dako	Cat#S3023
Random Hexamers	Thermo Fisher Scientific	Cat#N8080127
Critical Commercial Assays		
Rneasy Micro Kit	Qiagen	Cat#74004
Rnase-Free Dnase set	Qiagen	Cat#79254
NEBNext Poly(A) mRNA Magnetic Isolation Module	New England Biolabs	Cat#E7490L
GoTaq qPCR master mix	Promega	Cat#A6002
Stem Cell Nucleofector Kit 1	Lonza	Cat#VPH-5012
Purelink Viral RNA/DNA Mini Kit	Thermo Fisher Scientific	Cat#12280050
GoTaq polymerase	Promega	Cat#M7823
KOD Xtreme Hot Start DNA polymerase	Merck Millipore	Cat#US171975-3
VeriKine-HS Human IFN-α All Subtype TCM ELISA Kit	PBL Assay Science	Cat#41135-1
VeriKine-HS Human IFN Beta TCM ELISA, High Sensitivity	PBL Assay Science	Cat#41435-1
Deposited Data		

RNA-seq data of MOCK- and ZIKV- infected brain organoids and upon interferon treatment	This study	GEO:GSE123816
RNA-seq data of MOCK- and HSV- infected brain organoids and upon interferon treatment	This study	GEO:GSE145496
Experimental Models: Cell Lines		
Human: WT hESCs H9	WiCell	W0A9
Human: hESCs H9 carrying *IFNB1>GFP* and *ISRE>tdTomato* cassettes in the AAVS1 locus	This study	N/A
Human: A549 cells	ATCC	CCL-185
Monkey: Vero cells	ATCC	CCL-81
Oligonucleotides		
Primers for RT-qPCR, see Table S4	This study	N/A
Primer ICP34.5 Forward 5->3: CTGCACGCACATGCTTGCCT	(Bower et al., 1999)	N/A
Primer ICP34.5 Reverse 5->3: CTCGGGTGTAACGTTAGACC	(Bower et al., 1999)	N/A
Primer TK Forward 5->3 tkF51: GAAACTCCCGCACCTCTTCGG	(K. Wang et al., 2007)	N/A
Primer TK Reverse 5->3 tkR61: GGTTCCTTCCGGTATTGTCTCC	(K. Wang et al., 2007)	N/A
Recombinant DNA		
AASV1 SA2APuro-2xCHS4-IFNB1>eGFP-WPRE-SV40pA-2xCHS4 plasmid donor	This study	N/A
AAVS1 SA2ANeo-2xCHS4-ISRE>tdTomato-WPRE-SV40pA-2xCHS4 plasmid donor	This study	N/A
Software and Algorithms		
Zeiss Zen (Blue edition)	Zeiss	https://www.zeiss.com/microscopy/int/products/microscope-software/zen-lite.html
ImageJ Fiji (2.0.0)	NIH	https://imagej.net/Fiji
GraphPad Prism 8.0	GraphPad	https://www.graphpad.com/scientific-software/prism/
Microsoft Excel	Microsoft	https://www.microsoft.com/de-at/microsoft-365/excel
Adobe Illustrator	Adobe	https://www.adobe.com/at/products/illustrator.html
TopHat (v2.1.1)	Johns Hopkins University	https://ccb.jhu.edu/software/tophat/index.shtml
Cytoscape	The Cytoscape Consortium	https://cytoscape.org/
FlowJo	BD Life Sciences	https://www.flowjo.com/

Figure 1

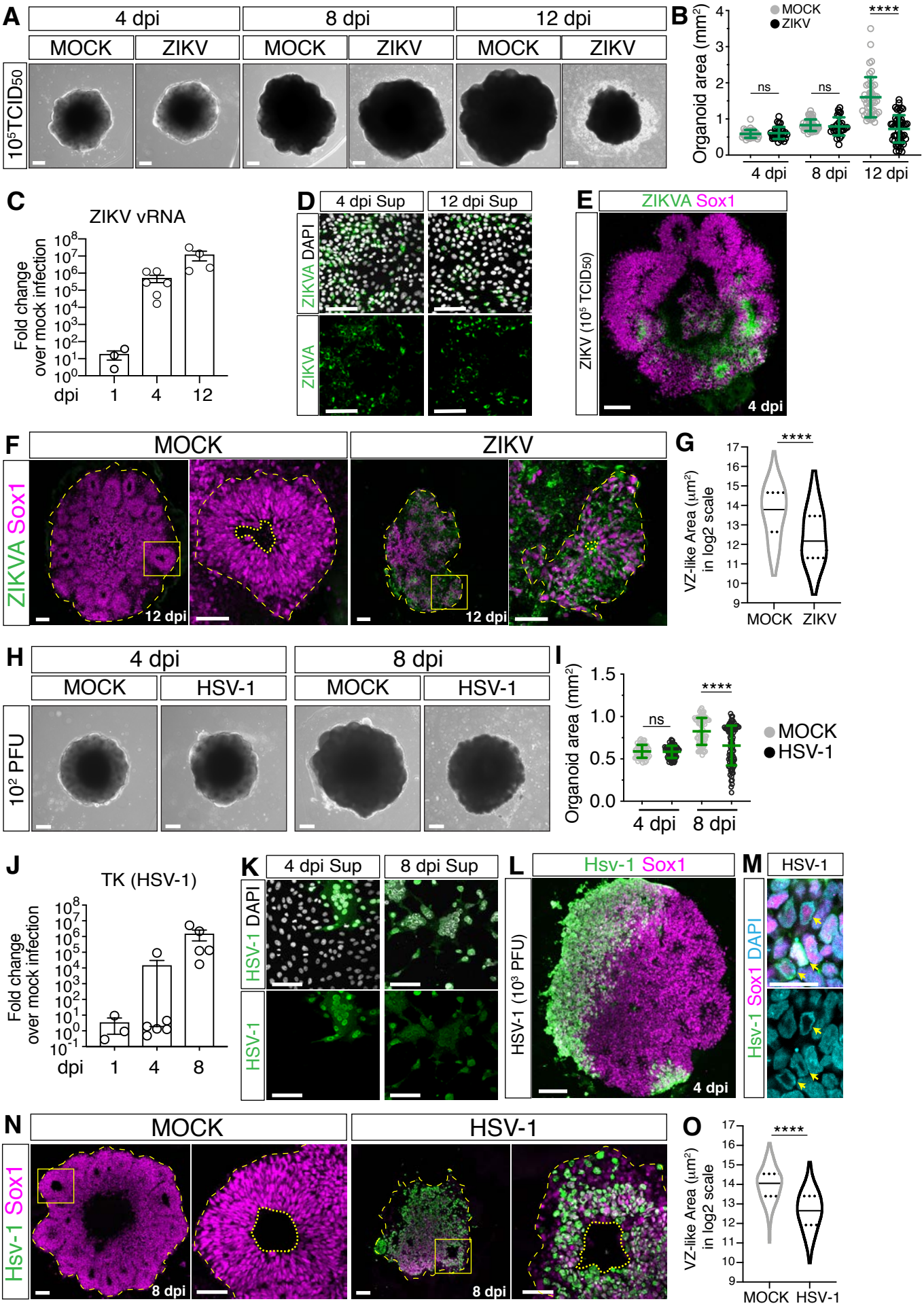
A
4 dpi
8 dpi
12 dpi
MOCK
ZIKV
MOCK
ZIKV
MOCK
ZIKV
10⁵TCID50
B
MOCK
ZIKV
****
Organoid area (mm²)
ns
ns
4 dpi
8 dpi
12 dpi
C
ZIKV vRNA
Fold change over mock infection
dpi
1
4
12
D
4 dpi Sup
12 dpi Sup
ZIKVA DAPI
ZIKVA
E
ZIKVA Sox1
ZIKV (10⁵ TCID50)
4 dpi
F
MOCK
ZIKV
ZIKVA Sox1
12 dpi
12 dpi
G
****
VZ-like Area (µm²) in log2 scale
MOCK
ZIKV
H
4 dpi
8 dpi
MOCK
HSV-1
MOCK
HSV-1
10² PFU
I
****
ns
Organoid area (mm²)
MOCK
HSV-1
4 dpi
8 dpi
J
TK (HSV-1)
Fold change over mock infection
dpi
1
4
8
K
4 dpi Sup
8 dpi Sup
HSV-1 DAPI
HSV-1
L
Hsv-1 Sox1
HSV-1 (10³ PFU)
4 dpi
M
HSV-1
Hsv-1 Sox1 DAPI
N
MOCK
HSV-1
Hsv-1 Sox1
8 dpi
8 dpi
O
****
VZ-like Area (µm²) in log2 scale
MOCK
HSV-1

Figure 2

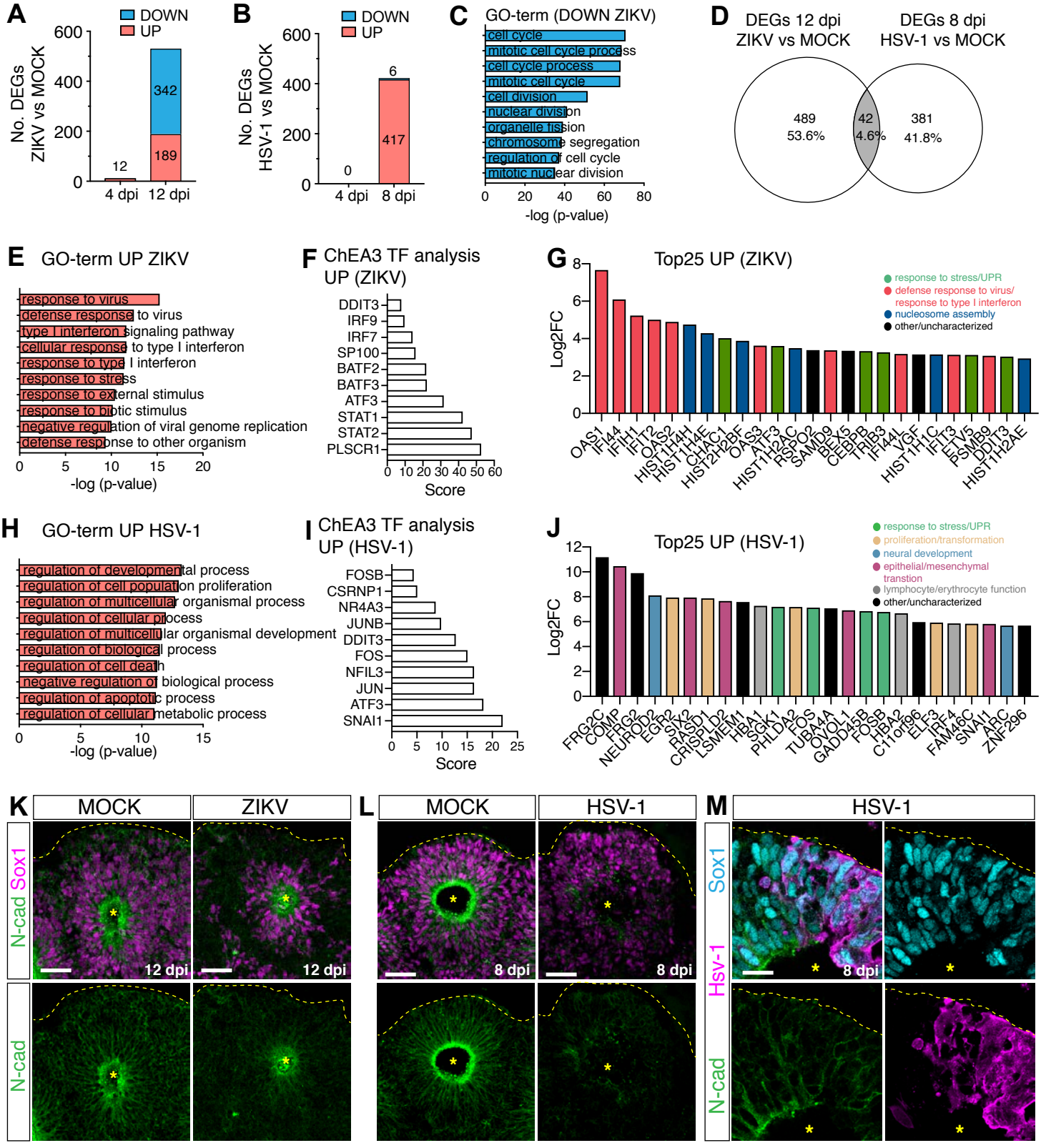
A
DOWN
UP
No. DEGs ZIKV vs MOCK
600
400
200
0
342
189
12
4 dpi
12 dpi
B
DOWN
UP
No. DEGs HSV-1 vs MOCK
600
400
200
0
6
417
0
4 dpi
8 dpi
C
GO-term (DOWN ZIKV)
cell cycle
mitotic cell cycle process
cell cycle process
mitotic cell cycle
cell division
nuclear division
organelle fission
chromosome segregation
regulation of cell cycle
mitotic nuclear division
0
20
40
60
80
-log (p-value)
D
DEGs 12 dpi ZIKV vs MOCK
DEGs 8 dpi HSV-1 vs MOCK
489
53.6%
42
4.6%
381
41.8%
E
GO-term UP ZIKV
response to virus
defense response to virus
type I interferon signaling pathway
cellular response to type I interferon
response to type I interferon
response to stress
response to external stimulus
response to biotic stimulus
negative regulation of viral genome replication
defense response to other organism
0
5
10
15
20
-log (p-value)
F
ChEA3 TF analysis UP (ZIKV)
DDIT3
IRF9
IRF7
SP100
BATF2
BATF3
ATF3
STAT1
STAT2
PLSCR1
0
10
20
30
40
50
60
Score
G
Top25 UP (ZIKV)
response to stress/UPR
defense response to virus/ response to type I interferon
nucleosome assembly
other/uncharacterized
Log2FC
8
6
4
2
0
OAS1
IFI44
IFIH1
IFIT2
OAS2
HIST1H4H
HIST1H4E
CHAC1
HIST2H2BF
OAS3
ATF3
HIST1H2AC
RSPO2
SAMD9
BEX5
CEBPB
TRIB3
IFI44L
VGF
HIST1H1C
IFIT3
ETV5
PSMB9
DDIT3
HIST1H2AE
H
GO-term UP HSV-1
regulation of developmental process
regulation of cell population proliferation
regulation of multicellular organismal process
regulation of cellular process
regulation of multicellular organismal development
regulation of biological process
regulation of cell death
negative regulation of biological process
regulation of apoptotic process
regulation of cellular metabolic process
0
5
10
15
-log (p-value)
I
ChEA3 TF analysis UP (HSV-1)
FOSB
CSRNP1
NR4A3
JUNB
DDIT3
FOS
NFIL3
JUN
ATF3
SNAI1
0
5
10
15
20
25
Score
J
Top25 UP (HSV-1)
response to stress/UPR
proliferation/transformation
neural development
epithelial/mesenchymal transtion
lymphocyte/erythrocyte function
other/uncharacterized
Log2FC
12
10
8
6
4
2
0
FRG2C
COMP
FRG2
NEUROD2
EGR2
SIX2
RASD1
CRISPLD2
LSMEM1
HBA1
SGK1
PHLDA2
FOS
TUBA4A
OVOL1
GADD45B
FOSB
HBA2
C11orf96
ELF3
IRF4
FAM46C
SNAI1
ARC
ZNF296
K
MOCK
ZIKV
N-cad Sox1
N-cad
12 dpi
12 dpi
L
MOCK
HSV-1
8 dpi
8 dpi
M
HSV-1
Sox1
Hsv-1
N-cad
8 dpi

Figure 3

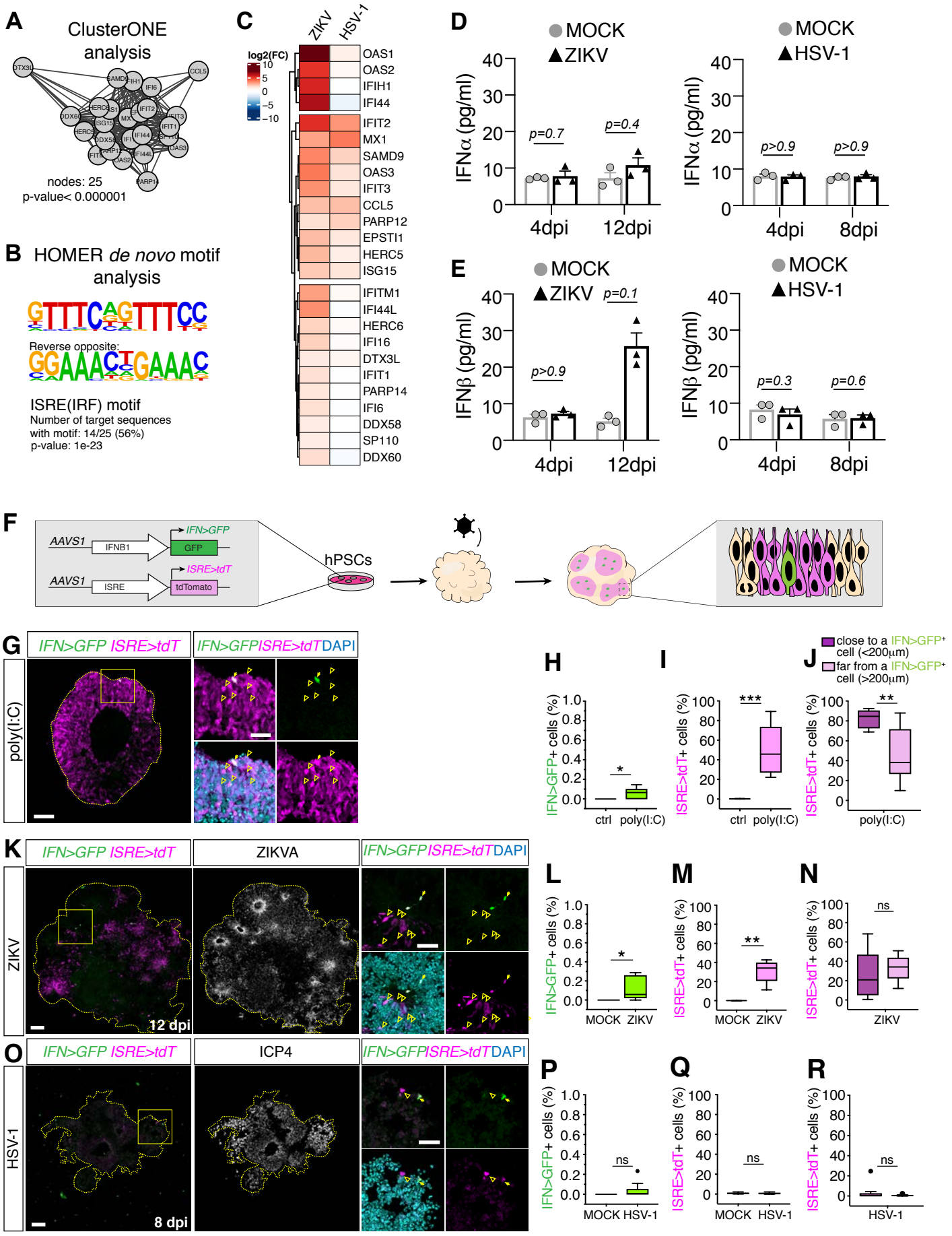
A
ClusterONE analysis
nodes: 25
p-value< 0.000001
B HOMER de novo motif analysis
Reverse opposite:
ISRE(IRF) motif
Number of target sequences with motif: 14/25 (56%)
p-value: 1e-23
C
ZIKV
HSV-1
log2(FC)
OAS1
OAS2
IFIH1
IFI44
IFIT2
MX1
SAMD9
OAS3
IFIT3
CCL5
PARP12
EPSTI1
HERC5
ISG15
IFITM1
IFI44L
HERC6
IFI16
DTX3L
IFIT1
PARP14
IFI6
DDX58
SP110
DDX60
D
MOCK
ZIKV
HSV-1
IFNα (pg/ml)
p=0.7
p=0.4
p>0.9
p>0.9
4dpi
12dpi
8dpi
E
IFNβ (pg/ml)
p>0.9
p=0.1
p=0.3
p=0.6
F
AAVS1
IFNB1
IFN>GFP
GFP
ISRE>tdT
tdTomato
hPSCs
G
IFN>GFP ISRE>tdT
IFN>GFP ISRE>tdT DAPI
poly(I:C)
H
IFN>GFP+ cells (%)
ctrl
poly(I:C)
I
ISRE>tdT+ cells (%)
J
close to a IFN>GFP+ cell (<200μm)
far from a IFN>GFP+ cell (>200μm)
K
ZIKVA
ZIKV
12 dpi
L
M
N
ns
O
ICP4
HSV-1
8 dpi
P
Q
R

Figure 4

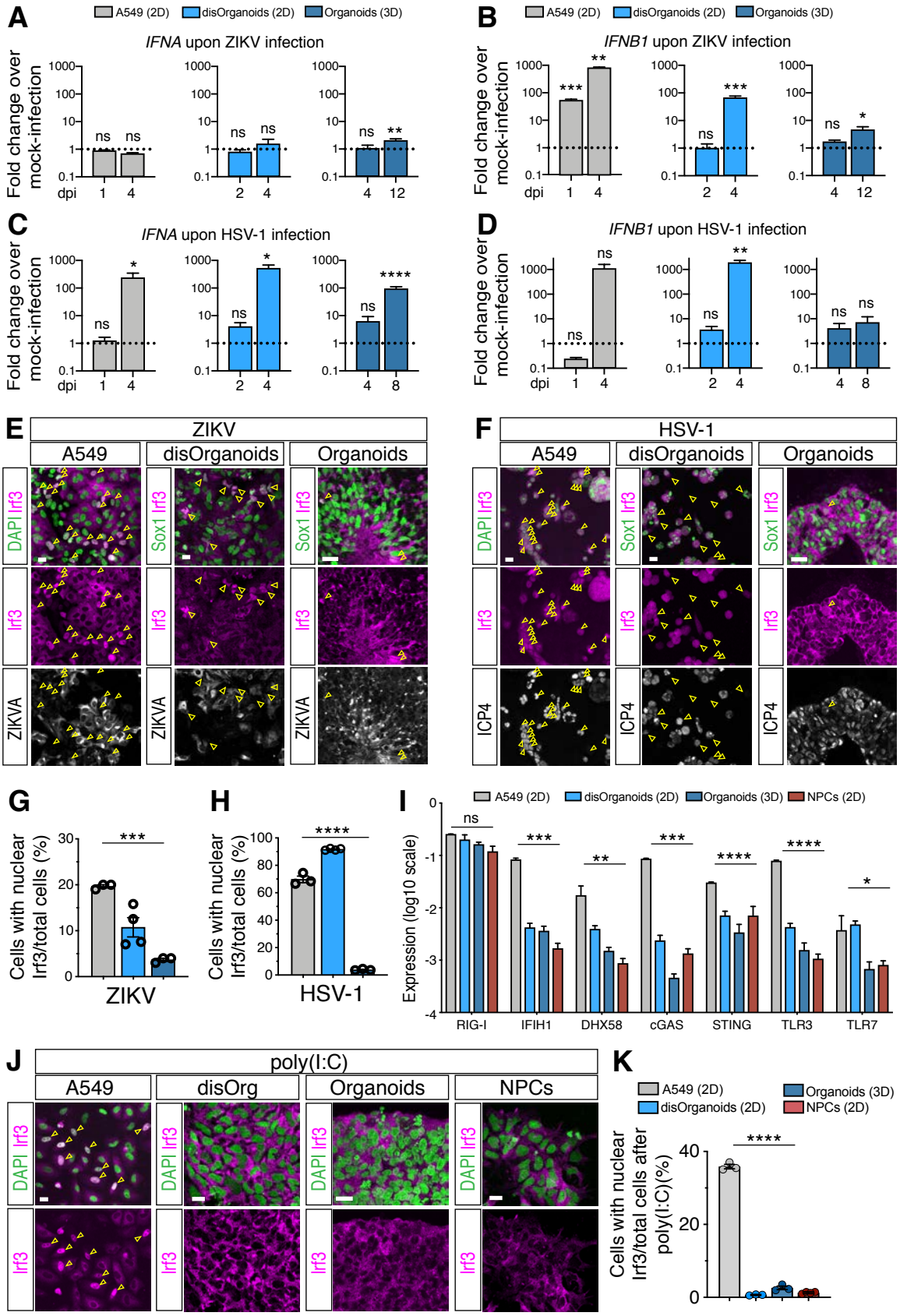
A
A549 (2D)
disOrganoids (2D)
Organoids (3D)
IFNA upon ZIKV infection
Fold change over mock-infection
dpi
B
IFNB1 upon ZIKV infection
C
IFNA upon HSV-1 infection
D
IFNB1 upon HSV-1 infection
E
ZIKV
A549
disOrganoids
Organoids
DAPI Irf3
Sox1 Irf3
Irf3
ZIKVA
F
HSV-1
ICP4
G
Cells with nuclear Irf3/total cells (%)
H
I
NPCs (2D)
Expression (log10 scale)
RIG-I
IFIH1
DHX58
cGAS
STING
TLR3
TLR7
J
poly(I:C)
disOrg
NPCs
K
Cells with nuclear Irf3/total cells after poly(I:C)(%)

Figure 5

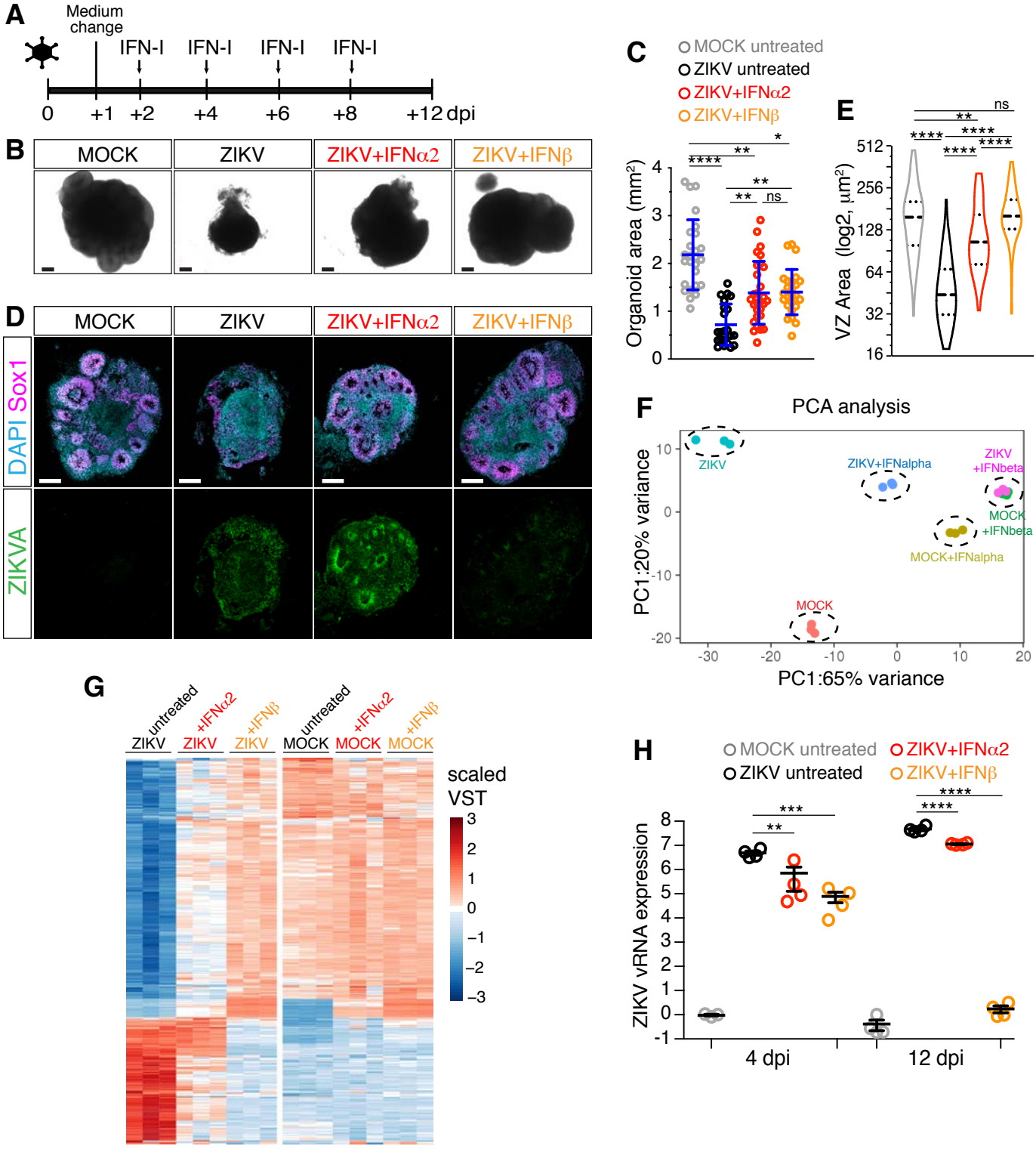
A
Medium change
IFN-I
IFN-I
IFN-I
IFN-I
0
+1
+2
+4
+6
+8
+12 dpi
B
MOCK
ZIKV
ZIKV+IFNα2
ZIKV+IFNβ
C
MOCK untreated
ZIKV untreated
ZIKV+IFNα2
ZIKV+IFNβ
Organoid area (mm²)
E
VZ Area (log2, µm²)
ns
D
MOCK
ZIKV
ZIKV+IFNα2
ZIKV+IFNβ
DAPI Sox1
ZIKVA
F
PCA analysis
PC1:20% variance
PC1:65% variance
ZIKV
ZIKV+IFNalpha
ZIKV +IFNbeta
MOCK +IFNbeta
MOCK+IFNalpha
MOCK
G
untreated
+IFNα2
+IFNβ
ZIKV
MOCK
scaled VST
H
MOCK untreated
ZIKV untreated
ZIKV+IFNα2
ZIKV+IFNβ
ZIKV vRNA expression
4 dpi
12 dpi

Figure 6

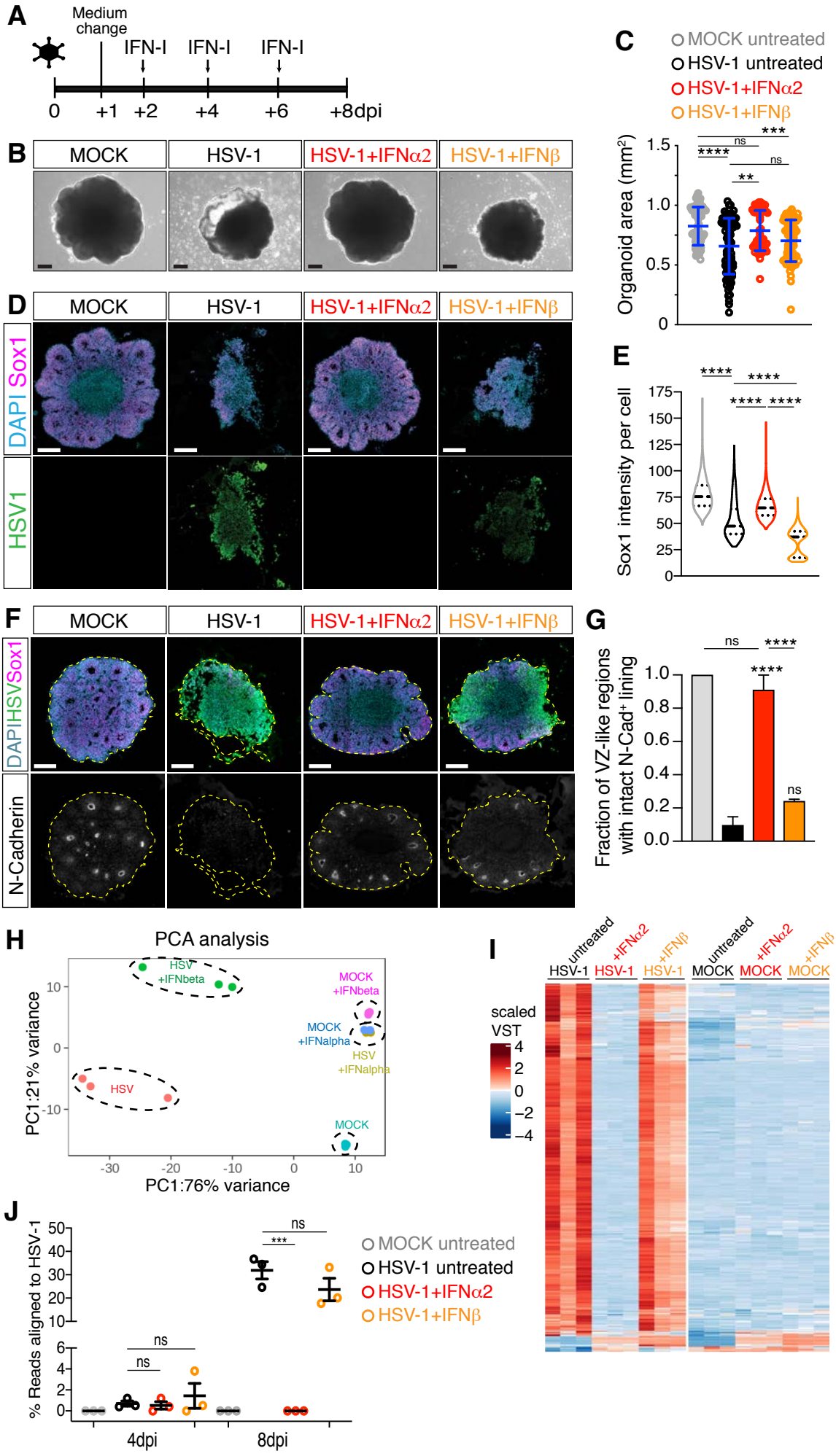
A
Medium change
IFN-I
IFN-I
IFN-I
0
+1
+2
+4
+6
+8dpi
B
MOCK
HSV-1
HSV-1+IFNα2
HSV-1+IFNβ
C
MOCK untreated
HSV-1 untreated
HSV-1+IFNα2
HSV-1+IFNβ
Organoid area (mm²)
D
DAPI Sox1
HSV1
E
Sox1 intensity per cell
F
DAPI HSV Sox1
N-Cadherin
G
Fraction of VZ-like regions with intact N-Cad⁺ lining
H
PCA analysis
PC1:21% variance
PC1:76% variance
HSV +IFNbeta
MOCK +IFNbeta
MOCK +IFNalpha
HSV +IFNalpha
HSV
MOCK
I
untreated
+IFNα2
+IFNβ
HSV-1
MOCK
scaled VST
J
% Reads aligned to HSV-1
4dpi
8dpi
MOCK untreated
HSV-1 untreated
HSV-1+IFNα2
HSV-1+IFNβ

Figure 7

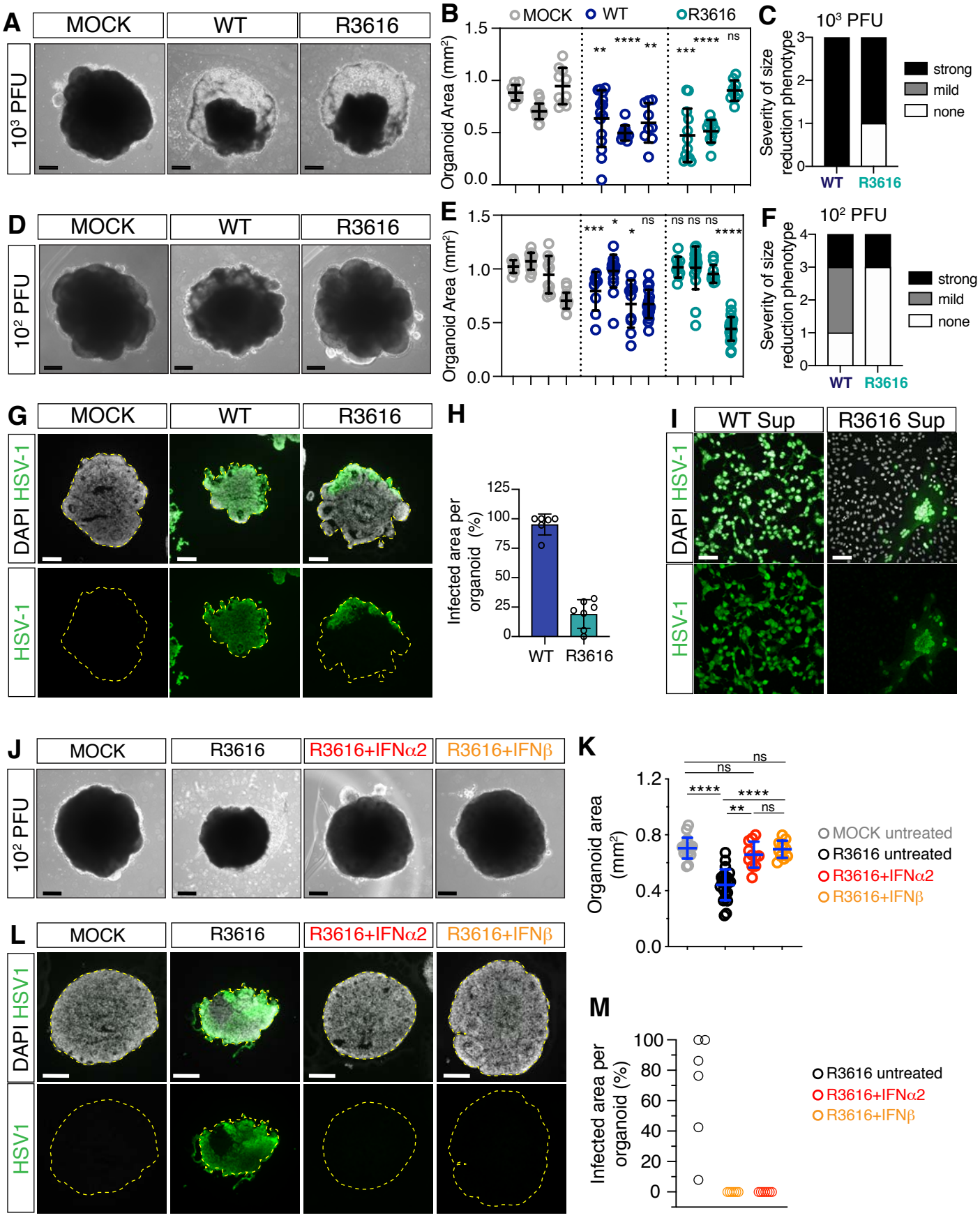
A
MOCK
WT
R3616
10³ PFU
B
MOCK
WT
R3616
Organoid Area (mm²)
C
10³ PFU
Severity of size reduction phenotype
strong
mild
none
WT
R3616
D
MOCK
WT
R3616
10² PFU
E
Organoid Area (mm²)
F
10² PFU
Severity of size reduction phenotype
strong
mild
none
WT
R3616
G
MOCK
WT
R3616
DAPI HSV-1
HSV-1
H
Infected area per organoid (%)
WT
R3616
I
WT Sup
R3616 Sup
DAPI HSV-1
HSV-1
J
MOCK
R3616
R3616+IFNα2
R3616+IFNβ
10² PFU
K
Organoid area (mm²)
MOCK untreated
R3616 untreated
R3616+IFNα2
R3616+IFNβ
L
MOCK
R3616
R3616+IFNα2
R3616+IFNβ
DAPI HSV1
HSV1
M
Infected area per organoid (%)
R3616 untreated
R3616+IFNα2
R3616+IFNβ

Figure S1

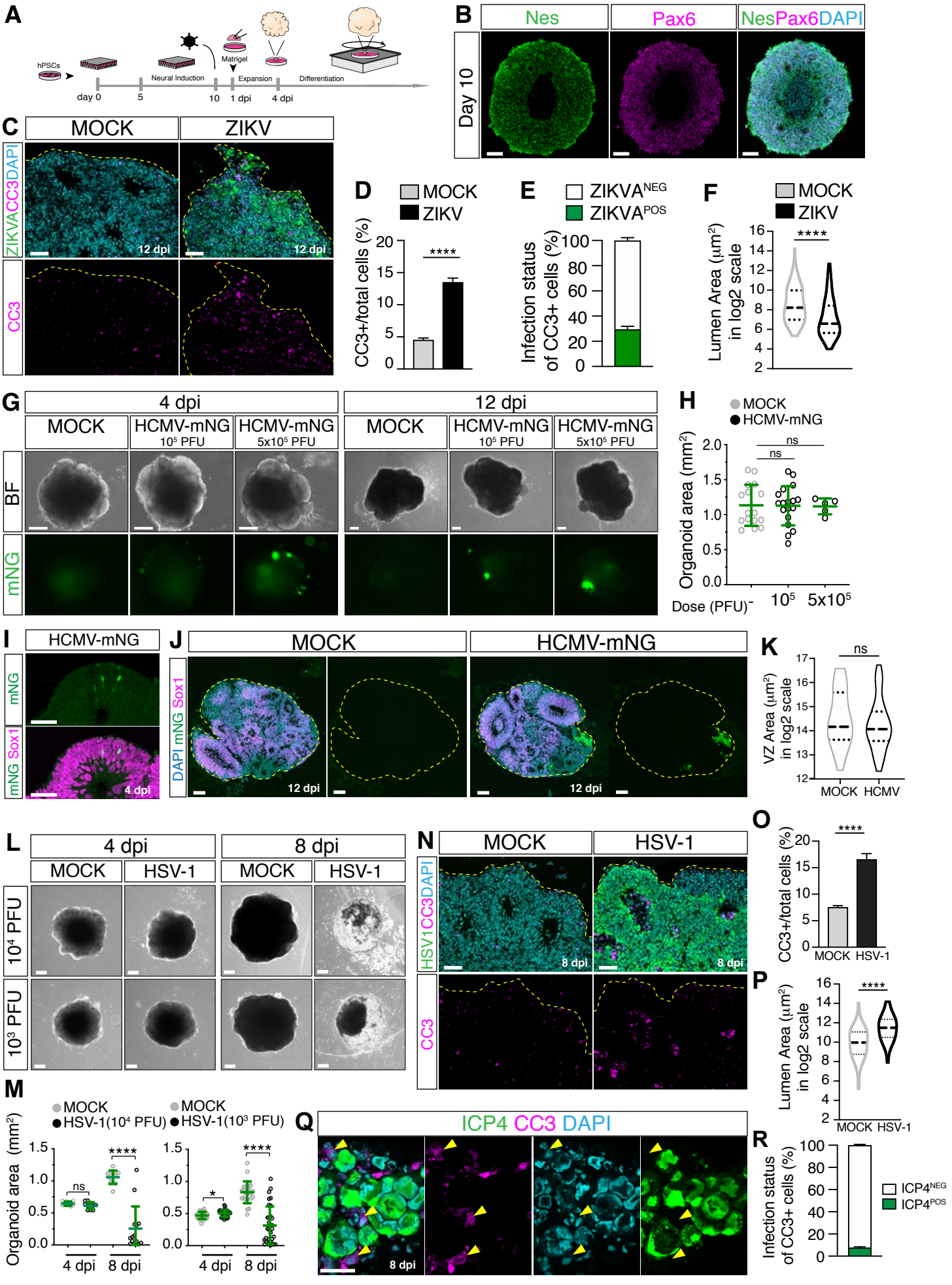
A
hPSCs
Neural Induction
Matrigel
Expansion
Differentiation
day 0
5
10
1 dpi
4 dpi
B
Nes
Pax6
NesPax6DAPI
Day 10
C
MOCK
ZIKV
ZIKVACC3DAPI
CC3
12 dpi
12 dpi
D
MOCK
ZIKV
CC3+/total cells (%)
****
E
ZIKVA^NEG
ZIKVA^POS
Infection status of CC3+ cells (%)
F
MOCK
ZIKV
Lumen Area (µm²) in log2 scale
****
G
4 dpi
12 dpi
MOCK
HCMV-mNG 10⁵ PFU
HCMV-mNG 5x10⁵ PFU
BF
mNG
H
MOCK
HCMV-mNG
Organoid area (mm²)
ns
ns
Dose (PFU)
10⁵
5x10⁵
I
HCMV-mNG
mNG
mNG Sox1
4 dpi
J
MOCK
HCMV-mNG
DAPI mNG Sox1
12 dpi
12 dpi
K
VZ Area (µm²) in log2 scale
ns
MOCK
HCMV
L
4 dpi
8 dpi
MOCK
HSV-1
MOCK
HSV-1
10⁴ PFU
10³ PFU
M
MOCK
HSV-1(10⁴ PFU)
MOCK
HSV-1(10³ PFU)
Organoid area (mm²)
ns
****
*
****
4 dpi
8 dpi
4 dpi
8 dpi
N
MOCK
HSV-1
HSV1CC3DAPI
CC3
8 dpi
8 dpi
O
CC3+/total cells (%)
****
MOCK
HSV-1
P
Lumen Area (µm²) in log2 scale
****
MOCK
HSV-1
Q
ICP4 CC3 DAPI
8 dpi
R
Infection status of CC3+ cells (%)
ICP4^NEG
ICP4^POS

Figure S2

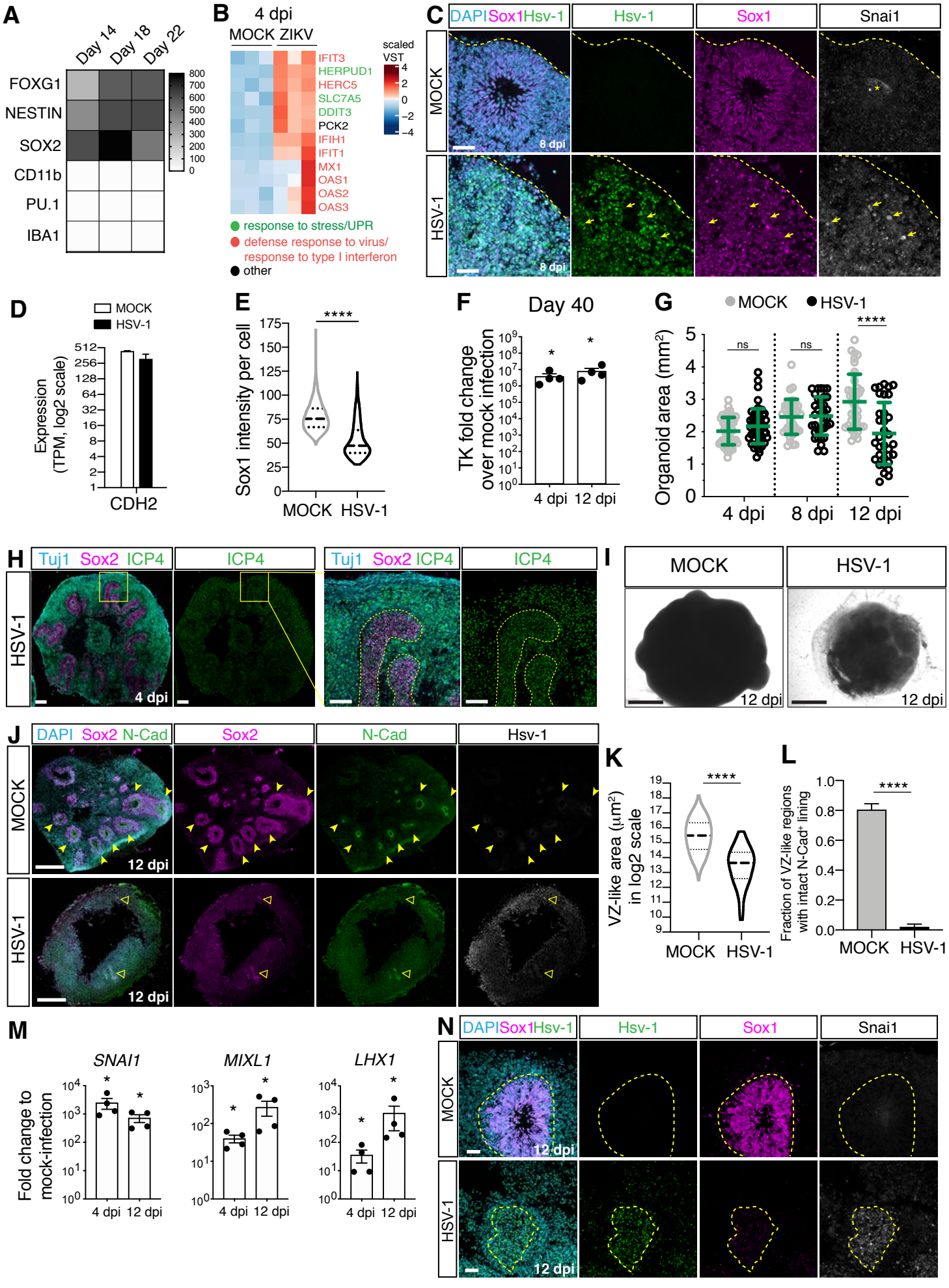
A
Day 14
Day 18
Day 22
FOXG1
NESTIN
SOX2
CD11b
PU.1
IBA1
800
700
600
500
400
300
200
100
0
B
4 dpi
MOCK ZIKV
scaled VST
4
2
0
−2
−4
IFIT3
HERPUD1
HERC5
SLC7A5
DDIT3
PCK2
IFIH1
IFIT1
MX1
OAS1
OAS2
OAS3
response to stress/UPR
defense response to virus/ response to type I interferon
other
C
DAPI Sox1 Hsv-1
Hsv-1
Sox1
Snai1
MOCK
HSV-1
8 dpi
8 dpi
D
MOCK
HSV-1
Expression (TPM, log2 scale)
512
256
128
64
32
16
8
4
2
1
CDH2
E
Sox1 intensity per cell
175
150
125
100
75
50
25
0
****
MOCK HSV-1
F
Day 40
TK fold change over mock infection
10^9
10^8
10^7
10^6
10^5
10^4
10^3
10^2
10^1
10^0
*
*
4 dpi 12 dpi
G
MOCK
HSV-1
Organoid area (mm^2)
5
4
3
2
1
0
ns
ns
****
4 dpi 8 dpi 12 dpi
H
Tuj1 Sox2 ICP4
ICP4
Tuj1 Sox2 ICP4
ICP4
HSV-1
4 dpi
I
MOCK
HSV-1
12 dpi
12 dpi
J
DAPI Sox2 N-Cad
Sox2
N-Cad
Hsv-1
MOCK
HSV-1
12 dpi
12 dpi
K
VZ-like area (μm^2) in log2 scale
19
18
17
16
15
14
13
12
11
10
9
****
MOCK HSV-1
L
Fraction of VZ-like regions with intact N-Cad+ lining
1.0
0.8
0.6
0.4
0.2
0.0
****
MOCK HSV-1
M
SNAI1
MIXL1
LHX1
Fold change to mock-infection
10^4
10^3
10^2
10^1
10^0
*
*
4 dpi 12 dpi
N
DAPI Sox1 Hsv-1
Hsv-1
Sox1
Snai1
MOCK
HSV-1
12 dpi
12 dpi

Figure S3

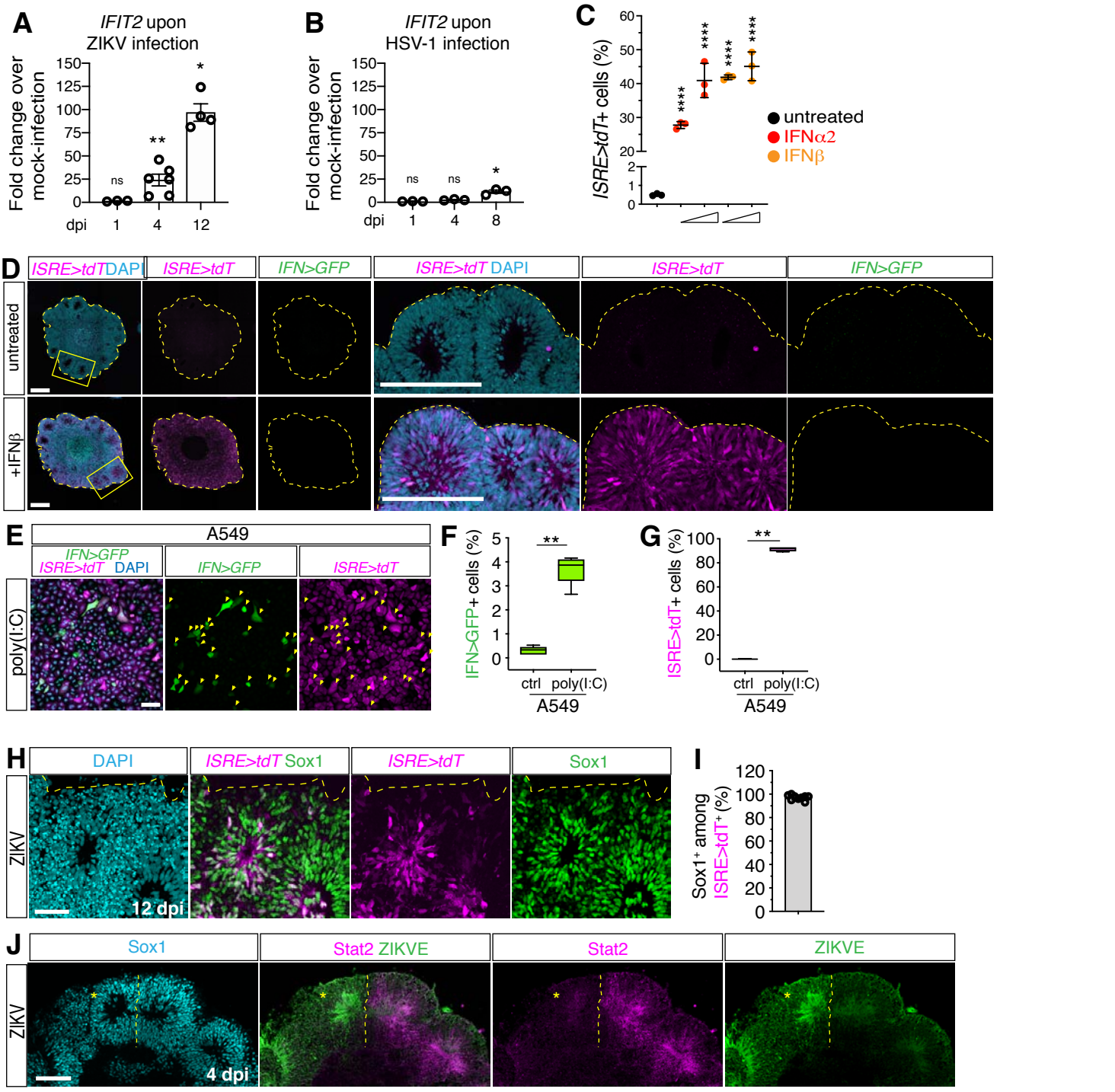
A
IFIT2 upon ZIKV infection
Fold change over mock-infection
ns
**
*
dpi 1 4 12
B
IFIT2 upon HSV-1 infection
Fold change over mock-infection
ns
ns
*
dpi 1 4 8
C
ISRE>tdT+ cells (%)
untreated
IFNα2
IFNβ
D
ISRE>tdT DAPI
ISRE>tdT
IFN>GFP
ISRE>tdT DAPI
ISRE>tdT
IFN>GFP
untreated
+IFNβ
E
A549
IFN>GFP ISRE>tdT DAPI
IFN>GFP
ISRE>tdT
poly(I:C)
F
IFN>GFP+ cells (%)
**
ctrl poly(I:C)
A549
G
ISRE>tdT+ cells (%)
**
ctrl poly(I:C)
A549
H
DAPI
ISRE>tdT Sox1
ISRE>tdT
Sox1
ZIKV
12 dpi
I
Sox1+ among ISRE>tdT+ (%)
J
Sox1
Stat2 ZIKVE
Stat2
ZIKVE
ZIKV
4 dpi

Figure S4

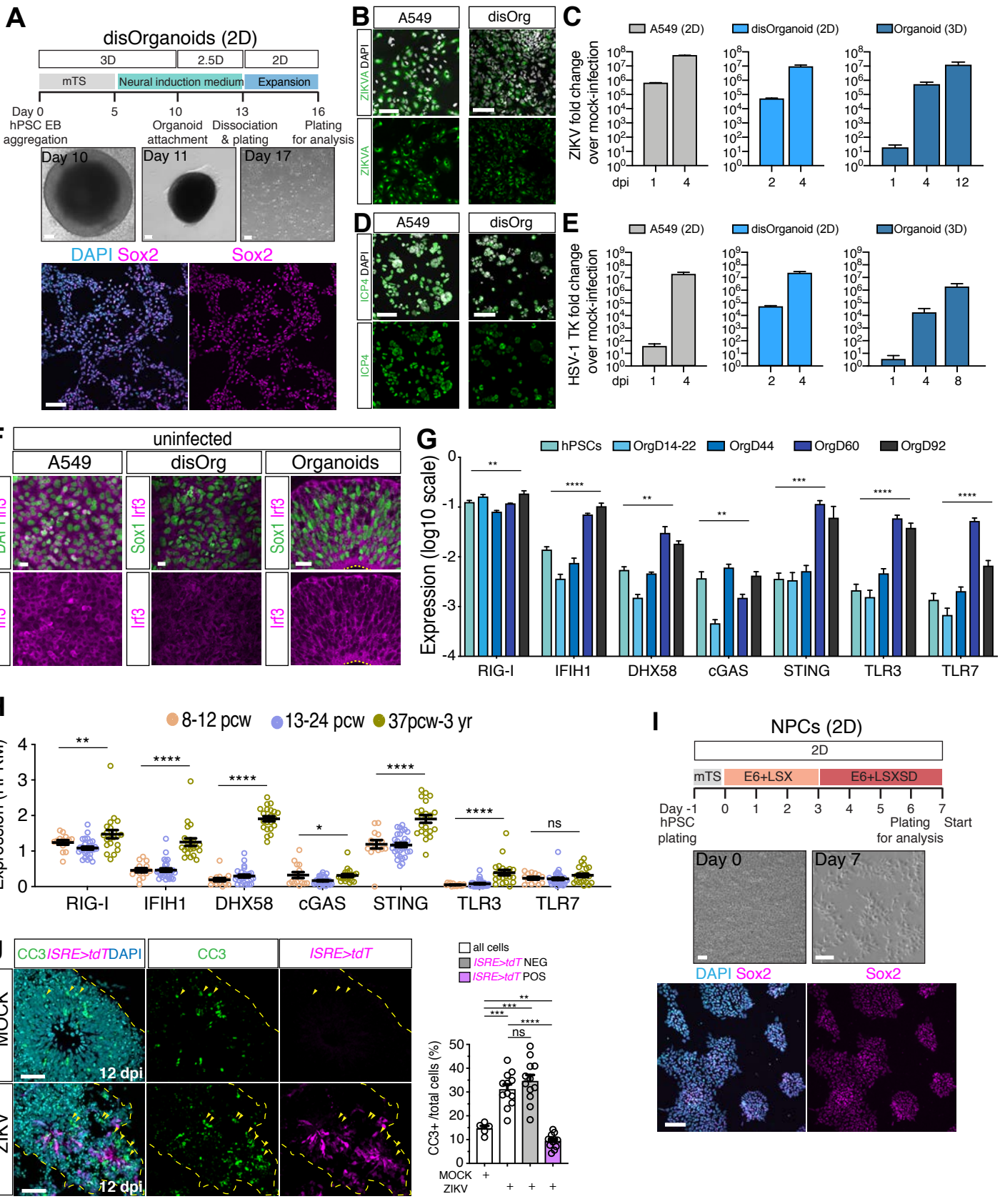
A
disOrganoids (2D)
3D
2.5D
2D
mTS
Neural induction medium
Expansion
Day 0 hPSC EB aggregation
5
10 Organoid attachment
13 Dissociation & plating
16 Plating for analysis
Day 10
Day 11
Day 17
DAPI Sox2
Sox2
B
A549
disOrg
ZIKVA DAPI
ZIKVA
C
A549 (2D)
disOrganoid (2D)
Organoid (3D)
ZIKV fold change over mock-infection
dpi
D
ICP4 DAPI
ICP4
E
HSV-1 TK fold change over mock-infection
F
uninfected
A549
disOrg
Organoids
DAPI Irf3
Sox1 Irf3
Irf3
G
hPSCs
OrgD14-22
OrgD44
OrgD60
OrgD92
Expression (log10 scale)
RIG-I
IFIH1
DHX58
cGAS
STING
TLR3
TLR7
H
8-12 pcw
13-24 pcw
37pcw-3 yr
Expression (RPKM)
ns
I
NPCs (2D)
2D
mTS
E6+LSX
E6+LSXSD
Day -1 hPSC plating
Plating for analysis
Start
Day 0
Day 7
DAPI Sox2
Sox2
J
CC3 ISRE>tdT DAPI
CC3
ISRE>tdT
MOCK
ZIKV
12 dpi
all cells
ISRE>tdT NEG
ISRE>tdT POS
CC3+ /total cells (%)
MOCK
ZIKV
ns

Figure S5

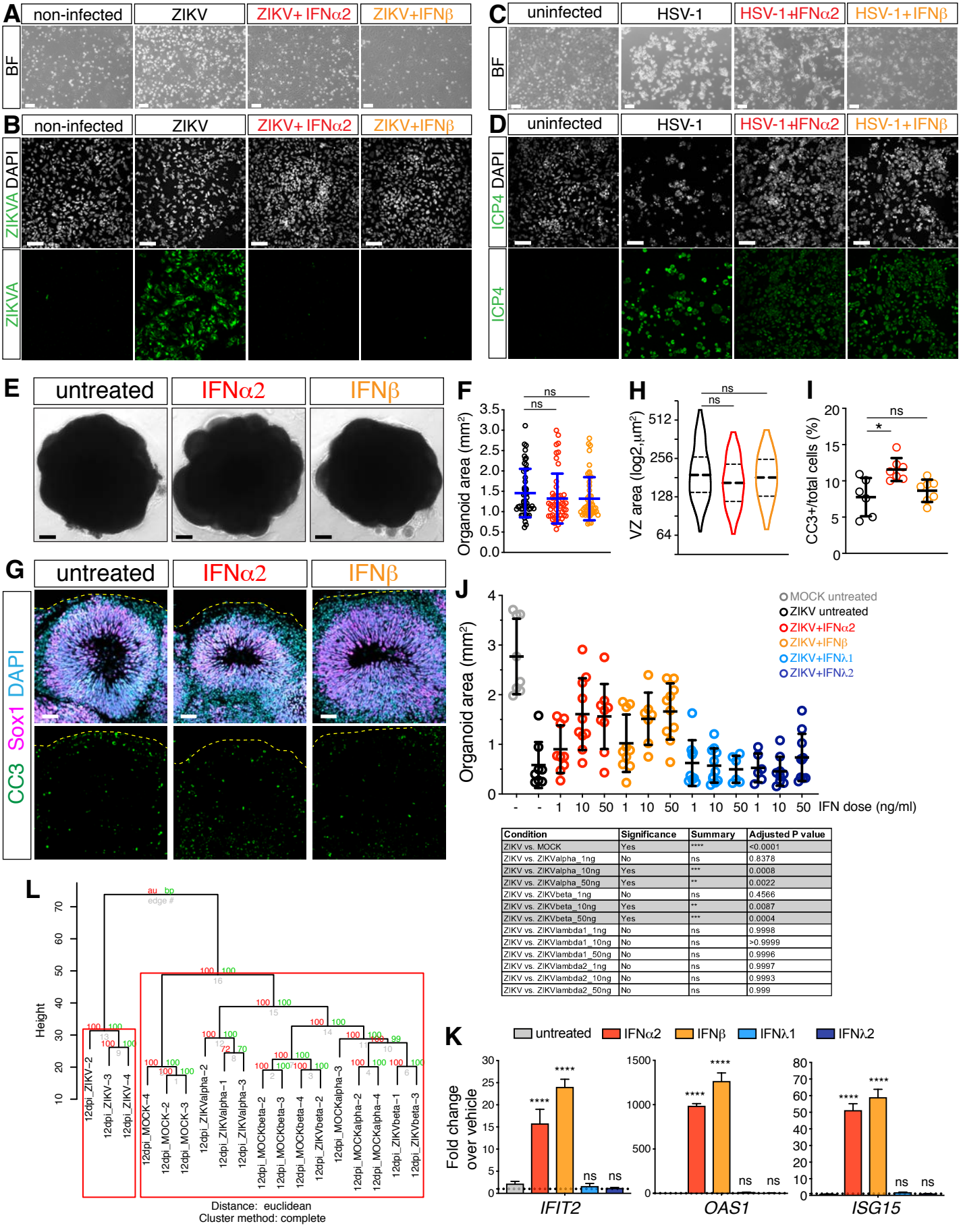

Condition	Significance	Summary	Adjusted P value
ZIKV vs. MOCK	Yes	****	<0.0001
ZIKV vs. ZIKValpha_1ng	No	ns	0.8378
ZIKV vs. ZIKValpha_10ng	Yes	***	0.0008
ZIKV vs. ZIKValpha_50ng	Yes	**	0.0022
ZIKV vs. ZIKVbeta_1ng	No	ns	0.4566
ZIKV vs. ZIKVbeta_10ng	Yes	**	0.0087
ZIKV vs. ZIKVbeta_50ng	Yes	***	0.0004
ZIKV vs. ZIKVlambda1_1ng	No	ns	0.9998
ZIKV vs. ZIKVlambda1_10ng	No	ns	>0.9999
ZIKV vs. ZIKVlambda1_50ng	No	ns	0.9996
ZIKV vs. ZIKVlambda2_1ng	No	ns	0.9997
ZIKV vs. ZIKVlambda2_10ng	No	ns	0.9993
ZIKV vs. ZIKVlambda2_50ng	No	ns	0.999

Figure S6

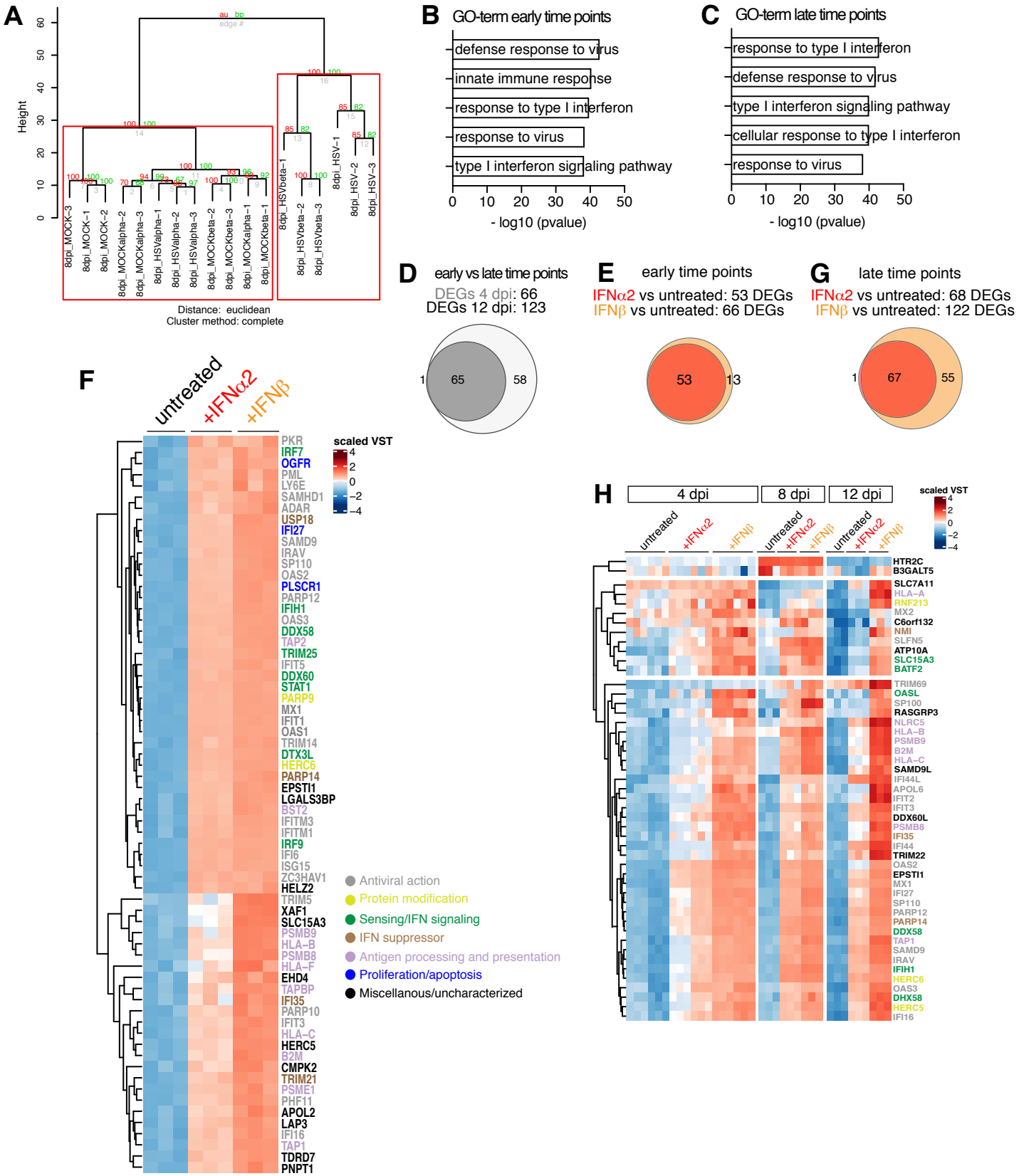
A
au bp
edge #
Height
8dpi_MOCK−3
8dpi_MOCK−1
8dpi_MOCK−2
8dpi_MOCKalpha−2
8dpi_MOCKalpha−3
8dpi_HSValpha−1
8dpi_HSValpha−2
8dpi_HSValpha−3
8dpi_MOCKbeta−2
8dpi_MOCKbeta−3
8dpi_MOCKalpha−1
8dpi_MOCKbeta−1
8dpi_HSVbeta−1
8dpi_HSVbeta−2
8dpi_HSVbeta−3
8dpi_HSV−1
8dpi_HSV−2
8dpi_HSV−3
Distance: euclidean
Cluster method: complete
B
GO-term early time points
defense response to virus
innate immune response
response to type I interferon
response to virus
type I interferon signaling pathway
- log10 (pvalue)
C
GO-term late time points
response to type I interferon
defense response to virus
type I interferon signaling pathway
cellular response to type I interferon
response to virus
- log10 (pvalue)
D
early vs late time points
DEGs 4 dpi: 66
DEGs 12 dpi: 123
1
65
58
E
early time points
IFNα2 vs untreated: 53 DEGs
IFNβ vs untreated: 66 DEGs
53
13
G
late time points
IFNα2 vs untreated: 68 DEGs
IFNβ vs untreated: 122 DEGs
1
67
55
F
untreated
+IFNα2
+IFNβ
scaled VST
PKR
IRF7
OGFR
PML
LY6E
SAMHD1
ADAR
USP18
IFI27
SAMD9
IRAV
SP110
OAS2
PLSCR1
PARP12
IFIH1
OAS3
DDX58
TAP2
TRIM25
IFIT5
DDX60
STAT1
PARP9
MX1
IFIT1
OAS1
TRIM14
DTX3L
HERC6
PARP14
EPSTI1
LGALS3BP
BST2
IFITM3
IFITM1
IRF9
IFI6
ISG15
ZC3HAV1
HELZ2
TRIM5
XAF1
SLC15A3
PSMB9
HLA−B
PSMB8
HLA−F
EHD4
TAPBP
IFI35
PARP10
IFIT3
HLA−C
HERC5
B2M
CMPK2
TRIM21
PSME1
PHF11
APOL2
LAP3
IFI16
TAP1
TDRD7
PNPT1
Antiviral action
Protein modification
Sensing/IFN signaling
IFN suppressor
Antigen processing and presentation
Proliferation/apoptosis
Miscellanous/uncharacterized
H
4 dpi
8 dpi
12 dpi
untreated
+IFNα2
+IFNβ
scaled VST
HTR2C
B3GALT5
SLC7A11
HLA−A
RNF213
MX2
C6orf132
NMI
SLFN5
ATP10A
SLC15A3
BATF2
TRIM69
OASL
SP100
RASGRP3
NLRC5
HLA−B
PSMB9
B2M
HLA−C
SAMD9L
IFI44L
APOL6
IFIT2
IFIT3
DDX60L
PSMB8
IFI35
IFI44
TRIM22
OAS2
EPSTI1
MX1
IFI27
SP110
PARP12
PARP14
DDX58
TAP1
SAMD9
IRAV
IFIH1
HERC6
OAS3
DHX58
HERC5
IFI16

Figure S7

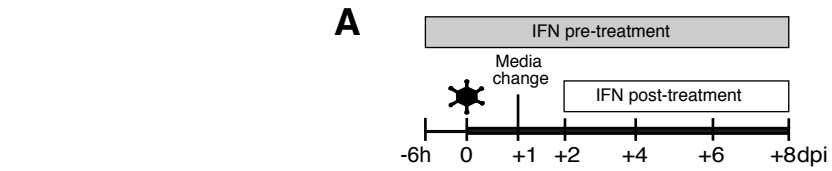

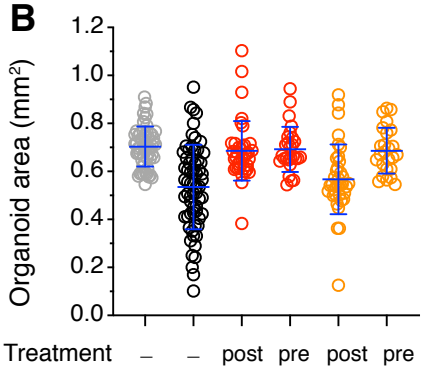

Comparison	Significance	adj P value
MOCK vs. HSV-1	***	<0.0001
MOCK vs. HSV-1+IFNα2 POST	ns	>0.9999
MOCK vs. HSV-1+IFNα2 PRE	***	<0.0001
MOCK vs. HSV-1 +IFNβ POST	***	<0.0001
MOCK vs. HSV-1+IFNβ PRE	ns	>0.9999
HSV-1 vs. HSV-1+IFNα2 POST	***	0.0002
HSV-1 vs. HSV-1+IFNβ POST	ns	>0.9999
HSV-1 vs. HSV-1+IFNα2 PRE	***	0.0002
HSV-1 vs. HSV-1+IFNβ PRE	***	0.0008
HSV-1+IFNα2 POST vs. HSV-1+IFNβ POST	**	0.0029
HSV-1+IFNα2 POST vs. HSV-1+IFNβ PRE	ns	>0.9999
HSV-1+IFNα2 POST vs. HSV-1+IFNα2 PRE	ns	>0.9999
HSV-1+IFNβ POST_vs. HSV-1+IFNβ PRE	**	0.0049
HSV-1+IFNβ POST vs. HSV-1+IFNα2 PRE	**	0.0014
HSV-1+IFNβ PRE vs. HSV-1+IFNα2 PRE	ns	>0.9999

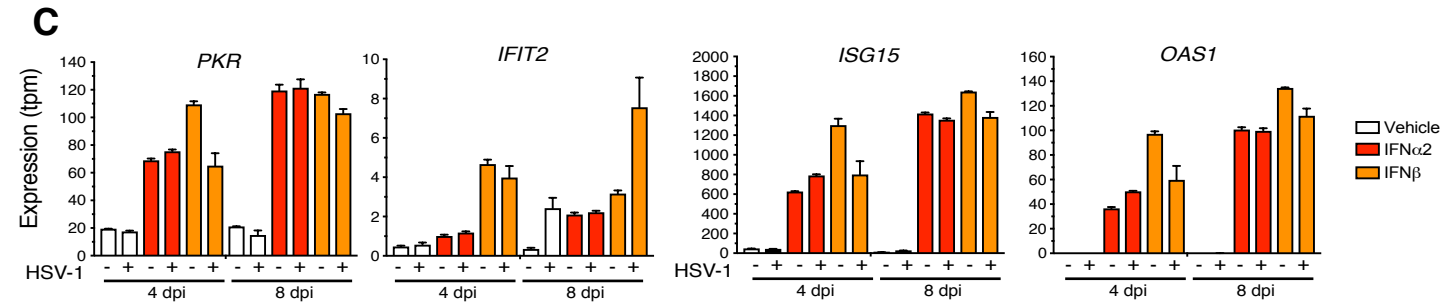

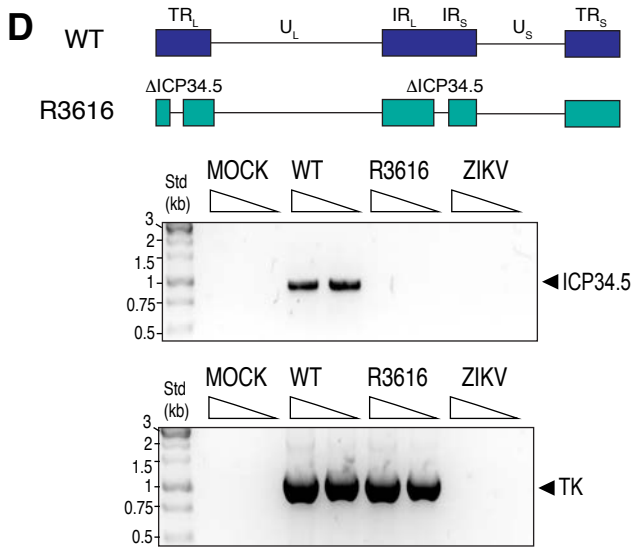

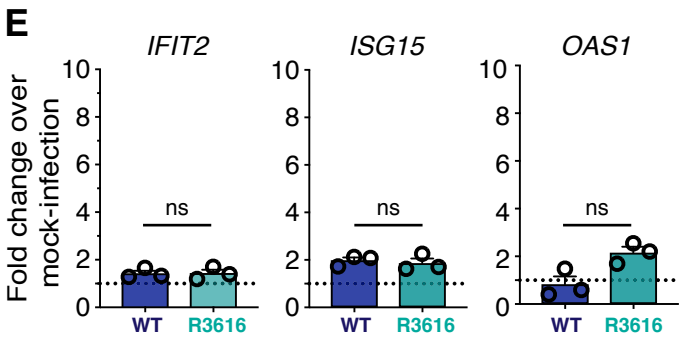

SUPPLEMENTAL FIGURE LEGENDS

Figure S1. ZIKV and HSV-1 infections impair organoid growth (related to Figure 1)

A) Schematic diagram of viral exposure of 10-days-old brain organoids used in this study. See STAR Methods for details.

B) Immunostaining (scale bars 100 μm) of 10-days-old organoids showing neuroectodermal identity.

C-F) Immunostaining (scale bars 50 μm) of organoids exposed to ZIKV or MOCK-treated. Dashed lines indicate organoid surface based on DAPI signal. Shown in D is the quantification of apoptosis measured by the fraction of cleaved caspase 3 (CC3) positive cells over total cells at 12 dpi. Shown in E is the quantification of infection status marked by Zika virus antigen (ZIKVA) of apoptotic cells (CC3+) in ZIKV-exposed organoids. Values represent mean ± SEM (n=3 experiments with 21 regions from 12 MOCK organoids, n=17 regions from 14 ZIKV organoids; **** is $p<0.0001$, Mann-Whitney test). Quantification of the lumen area is shown in F. Violin plots show median and quartiles (n=129 regions in MOCK organoids, n=110 regions in infected organoids from 3 experiments; **** is $p<0.0001$, Mann-Whitney test).

G-H) Images (scale bars 200 μm) and area quantification of organoids exposed to Human Cytomegalovirus-mNeonGreen (HCMV-mNG) or MOCK-treated. Values are mean ± SD and represent individual organoids ($p>0.9999$ for 10^5 PFU; $p=0.8417$ for 5×10^5 PFU; Mann-Whitney test).

I-K) Immunostaining (scale bars 50 μm in I, 100 μm in J) and quantifications of the ventricular zone (VZ)-like area of organoids exposed to HCMV-mNG (5×10^5 PFU) or MOCK-treated and analyzed at 12 dpi. Dashed lines indicate organoid contour based on DAPI signal. Violin plots show median and quartiles (n=40 regions from 3 MOCK organoids, n=79 from 3 HCMV-mNG organoids; $p=0.2375$; Mann-Whitney test).

L-M) Images (scale bars 200 μm) and area measurements of organoids exposed to HSV-1 (10^4 and 10^3 PFU). Values are mean ± SD and represent individual organoids ($p=0.1397$ 10^4 PFU 4 dpi; $p=0.0164$ 10^3 PFU 4 dpi; **** is $p<0.0001$, Mann-Whitney test).

N-R) Immunostaining (scale bar 50 μm in N, 20 μm in Q) of organoids exposed to HSV-1 or MOCK-treated. Dashed lines indicate organoid surface based on DAPI signal. Arrowheads in Q indicate CC3+ cells. Note the altered nuclear morphology and peripheral chromatin of ICP4 positive cells. Infected cell polypeptide 4 (ICP4) is an immediate-early viral protein produced during HSV-1 lytic infection. Values in O represent mean ± SEM (n=3 experiments with 18 regions from 12 MOCK organoids and 16 regions from 12 HSV-1 organoids; **** is $p<0.0001$, Mann-Whitney test). Violin plots in P represent median and quartiles (n= 35 regions from 4 MOCK organoids and n=35 from 9 HSV-1 organoids from 3 experiments; **** is $p<0.0001$; Mann-Whitney test). Shown in R is the quantification of infection status (marked by ICP4) in

organoids exposed to HSV-1. Values represent mean ± SEM (n=3 experiments with a total of 16 regions from 12 organoids).

Dpi, days post-infection; ns, non-significant. See also Table S2. Pos, positive; Neg, negative.

Figure S2. ZIKV and HSV-1 infections elicit distinct transcriptional responses (related to Figure 2)

A) Heatmap showing high expression (>100 transcripts per million, tpm) of the neural progenitor markers *FOXG1*, *NESTIN* and *SOX2* in MOCK-treated organoids measured by RNA-sequencing. Low expression of the microglia/macrophage progenitor markers *CD11b*, *PU.1* and *IBA1* (<10 tpm) is shown for comparison.

B) Expression (in scaled Variance Stabilizing Transformation or VST) of differentially expressed genes in ZIKV-exposed vs MOCK-exposed organoids.

C) Immunostaining (scale bars 50 μm) of organoids exposed to HSV-1 or MOCK-treated. Dashed lines indicate organoid surface based on DAPI signal. Arrows indicate nuclear Snai1 signal in infected organoids, while the asterisk marks apical Sna1 signal in mock-treated organoids.

D) Expression (in transcripts per million, tpm) of the N-cadherin gene *CDH2* measured by RNA-sequencing at 8 dpi. Values are mean ± SD (n=3).

E) Quantification of Sox1 mean intensity per cell at 8 dpi. Values are median and quartiles (n=7961 cells from 4 MOCK organoids, n=5316 cells from 5 HSV-1 organoids; **** is p<0.0001, Mann-Whitney test).

F) RT-qPCR analysis of HSV-1 thymidine kinase (TK) gene expression in 40-days-old organoids exposed to HSV-1 over MOCK-treated samples. Values are mean ± SEM (n=4 experiments, p=0.0286, Mann-Whitney test).

G) Area quantification of 40-days-old organoids infected with HSV-1 or MOCK-treated. Values are mean ± SD and represent individual organoids (p=0.1846 4 dpi; p=0.7137 8dpi; **** is p<0.0001 12 dpi; Mann-Whitney test).

H) Immunostaining of 40-days-old organoids exposed to HSV-1. Dashed lines indicate ventricular zone (VZ) contour. Scale bars are 200 μm and 100 μm (insets).

I-L) Images, immunostaining (scale bars 500 μm) and quantifications of 40-days-old organoids analyzed at 12 dpi. Arrowheads and triangles in J indicate normal and disrupted ventricular zone (VZ)-like regions in MOCK-treated and HSV-1-infected organoids respectively. Violin plots in K show median and quartiles (n=128 regions from 12 MOCK organoids and n=86 regions from 12 HSV-1 organoids from 3 experiments; **** is p<0.0001, Mann-Whitney test). Data in L are mean ± SEM (n=3 experiments for a total of 18 regions for MOCK and 23 regions for HSV-1 organoids; **** is p<0.000,; Mann-Whitney test).

M) RT-qPCR analysis showing upregulation of the epithelial-mesenchymal transition (EMT) gene *SNAI1* and early mesodermal genes *MIXL1* and *LHX1* in 40-days-old organoids exposed to HSV-1 over MOCK-treated samples. Values are mean ± SEM (n=4 experiments, p=0.0286 in all cases, Mann-Whitney test over age-matched MOCK controls).
N) Immunostaining (scale bars 50 μm) of 40-days-old organoids exposed to HSV-1 or MOCK-treated. Dashed lines indicate VZ-like regions.
Dpi, days post-infection.

Figure S3. ZIKV and HSV-1 infections differentially engage the IFN-I system (related to Figure 3)
A-B) RT-qPCR analysis of *IFIT2* expression in organoids after ZIKV or HSV-1 exposure relative to their MOCK counterparts. Values are mean ± SEM (ZIKV: p=0.7 1 dpi; p=0.0022 4 dpi; p=0.0286 12 dpi; HSV-1: p=0.4 1 dpi; p=0.7 4 dpi; p=0.0119 8 dpi; Mann-Whitney test comparisons over age-matched MOCK-treated counterparts).
C) Quantification of *ISRE>tdTomato (ISRE>tdT)* positive cells measured by flow cytometry in 12-days-old organoids carrying the dual reporter system and incubated with increasing doses of the indicated recombinant IFN-I (10 ng/ml and 50 ng/ml) for one day. Measurements are mean ± SD (n=3; **** is p<0.0001, one-way ANOVA multiple comparisons over untreated).
D) Immunostaining (scale bars 200 μm) of 14-days-old organoids carrying the dual reporter system and incubated for 48 hours with IFNβ. Dashed lines indicate organoid contour based on DAPI signal. Insets show a magnified view. Note the low expression of *IFN>GFP* and *ISRE>tdT* reporters in the untreated sample.
E-G) Immunostaining (scale bars 100 μm) and quantifications of A549 cells engineered with the dual reporter system and analyzed 24 hours after stimulation with poly(I:C). Arrowheads indicate *IFN>GFP* positive cells. Graphs are Tukey plots (n=5; p=0.0043 in F, p=0.0043 in G, Mann-Whitney tests). Ctrl, control transfection.
H-I) Immunostaining (scale bars 50 μm) and quantification of *ISRE>tdT* expressing cells in ZIKV-exposed organoids engineered with the dual reporter system. Dashed lines indicate organoid surface based on DAPI signal. Values are mean ± SD (n=9 regions from 3 organoids).
J) Immunostaining (scale bars 100 μm) of organoids exposed to ZIKV. Dashed lines separate the infected region (marked by an asterisk) from the uninfected area. ZIKVE, Zika virus Envelope protein.
dpi, days post-infection; ns, non-significant.

Figure S4. The IFN-I response in brain organoids is more attenuated than in 2D cultures (related to Figure 4)

A) Outline of the protocol used to generate 2D cultures of cells dissociated from organoids (disOrganoids) derived from human pluripotent stem cells (hPSCs). Immunostaining (scale bars 100 μm) at day 16 is shown at the bottom. mTS, mTeSR1; EB, embryoid body. See STAR Methods for details.

B-E) Immunostaining (scale bars 100 μm) of A549 cells and disOrganoid cultures (disOrg) exposed to ZIKV or HSV-1 and analyzed at 4 dpi. Shown in C and E are the quantifications of ZIKV vRNA and HSV-1 thymidine kinase (TK) expression levels by RT-qPCR showing a much faster kinetics of ZIKV and HSV-1 replication in 2D cultures compared to brain organoids. Values are mean ± SEM (n=3 for A549, n=4 disOrg, n≥3 Org; p values for ZIKV: p=0.1 A549 1 and 4 dpi; p=0.0286 disOrg 2 and 4 dpi; p=0.1 Org 1 dpi, p=0.0022 Org 4 dpi, p=0.0286 Org 12 dpi; p values for HSV-1: p=0.1 A549; p=0.0286 disOrg; p>0.9999 Org 1 dpi, p=0.4 Org 4 dpi, p=0.0079 Org 12 dpi; Mann-Whitney tests). Note that HSV-1 infection in 2D cultures induce the formation of multicellular structures.

F) Immunostaining (scale bars 20 μm) of uninfected cultures showing cytoplasmic Irf3 localization.

G) Expression of nucleic acid sensors measured by RT-qPCR in hPSCs and organoids at various stages. D, day; Org, organoids. Values are mean ± SEM (n=4 for hPSCs, OrgD44, OrgD60; n=5 OrgD14-22; n=3 OrgD92; p=0.0024 RIG-I, p=0.0040 DHX58, p=0.0017 cGAS, p=0.0006 STING, **** is p<0.0001, one-way ANOVA).

H) Expression of nucleic acid sensors (in Reads Per Kilobase of transcript, per Million mapped reads, RPKM) in human fetal brains. Data were retrieved from the BrainSpan dataset (Miller et al., 2014) and include measurements from dorsolateral, ventrolateral and medial prefrontal cortex isolated from brains at various developmental ages. Values are mean ± SEM (p=0.0016 RIG-I; p=0.0101 cGAS; p=0.1921 TLR7; **** is p<0.0001, one-way ANOVA). pcw, post conceptional week; yrs, years.

I) Outline of the protocol used to generate human neural progenitor cells (NPCs) via monolayer cultures. Immunostaining (scale bars 100 μm) at day 7 is shown at the bottom. See STAR Methods for details.

J) Immunostaining (scale bars 50 μm) and quantification of apoptosis in organoids carrying the dual reporter system, exposed to ZIKV or MOCK-treated. Dashed lines indicate organoid surface based on DAPI signal. Arrowheads indicate examples of tdTomato-negative CC3+ cells. CC3+ cells were scored regardless of their *ISRE>tdT* expression (all cells) or based on *ISRE>tdT* positive (POS) or negative (NEG) expression. Values are mean ± SEM and represent individual regions from 3 organoids for MOCK and 4 for ZIKV (p=0.0002 ZIKV all vs

MOCK all; p=0.0002 *ISRE>tdT* NEG vs MOCK all; p=0.003 *ISRE>tdT* POS vs MOCK all; p=0.003 *ISRE>tdT* POS vs MOCK all; p=0.3 *ISRE>tdT* NEG vs ZIKV all; p<0.0001 *ISRE>tdT* POS vs ZIKV all; unpaired t tests).
Dpi, days post-infection.

Figure S5. Effect of IFN-I in 2D and 3D cultures (related to Figure 5)

A-D) Images and immunostaining (scale bars 100 μm) of 2D cultures of cells dissociated from organoids (disOrganoids) infected with ZIKV or HSV-1, treated with IFN-I and analyzed at 4 dpi. IFN-I were administered at 2 and 48 hours after exposure.

E-I) Images (in E, scale bars 200 μm) and immunostaining (in G, scale bars 50 μm) of uninfected organoids treated with IFN-I as described in Figure 5A and analyzed at 12 dpi. Dashed lines mark the organoid surface according to DAPI signal. Data in F are mean ± SD and represent individual organoids (p=0.3296 IFNα2 vs untreated; p=0.5560 IFNβ vs untreated, Kruskal-Wallis multiple comparisons tests). Violin plots in H show median and quartiles (n=105 regions from 7 untreated organoids, n=103 from 7 IFNα2-treated organoids, n=119 from 9 IFNβ-treated organoids; p=0.0907 for IFNα2 vs untreated; p>0.9999 for IFNβ vs untreated, Kruskal-Wallis multiple comparisons test). Values in I represent mean ± SD (n=6 untreated regions, n=7 IFNα2-treated regions, n=7 IFNβ-treated regions, from 2 organoids per condition; p=0.0218 IFNα2 vs untreated, p>0.9999 IFNβ vs untreated, Kruskal-Wallis multiple comparisons tests). See also Table S2.

J) Area quantification of organoids exposed to ZIKV and treated with increasing doses of IFN-I and type III IFNs (IFNλ1 and IFNλ2) as described in Figure 5A. Organoids were analyzed at 12 dpi. Values are mean ± SD and represent individual organoids (one-way ANOVA with Dunnett's multiple comparisons tests).

K) Quantification of ISG gene expression by RT-qPCR in 12-days-old organoids after incubation with the indicated interferons (IFNs) for one day. Values are mean ± SEM (n=3; *IFIT2*: p=0.9977 IFNλ1, p=0.9832 IFNλ2; *OAS1*: p=0.9992 IFNλ1; p>0.9999 IFNλ2; *ISG15*: p=0.9992 IFNλ1; p>0.9999 IFNλ2; **** is p<0.0001, one-way ANOVA with Tukey's multiple comparisons test to the untreated condition).

L) Dendrogram showing hierarchical clustering of ZIKV-infected organoids analyzed by RNA-sequencing. AU and BP values (%) are shown on the edges of the clustering. Red boxes indicate the main clusters identified with AU larger than 95%. AU, approximately unbiased; BP, bootstrap probability.

Dpi, days post-infection; ns, non-significant.

Figure S6. IFNβ treatment fails to prevent HSV-1-induced organoid defects (related to Figure 6)

A) Dendrogram showing hierarchical clustering of HSV-1-infected organoids treated with interferons as described in Figure 6A and analyzed by RNA-sequencing. AU and BP values (%) are shown on the edges of the clustering. Red boxes indicate the main clusters identified with AU larger than 95%. AU, approximately unbiased; BP, bootstrap probability.

B-D) Analysis of differentially expressed genes (DEGs) combined from IFNα2-treated and IFNβ-treated samples vs untreated controls at early and late time points (corresponding to 4 and 12 dpi respectively). The top 5 GO-terms are shown.

E-G) Analysis of differentially expressed genes (DEGs) in IFNα2-treated and IFNβ-treated samples vs untreated controls at early and late time points. VST, variance stabilizing transformation.

H) Time-resolved expression of genes differentially expressed in IFNα2- or IFNβ-treated samples.

dpi, days post-infection.

Figure S7. HSV-1 selectively counteracts IFNβ activity (related to Figure 7)

A-B) Outline of IFN-I pre- and post-treatment experiments and area quantification of organoids at 8 dpi. Lines are mean ± SD and represent individual organoids (Kruskal-Wallis multiple comparisons tests). See also Table S2.

C) Expression of the ISGs *PKR*, *IFIT2*, *ISG15* and *OAS1* measured by RNA-sequencing. Values represent mean ± SEM (n=3).

D) Schematic diagram of a linearized DNA molecule of HSV-1 showing the relevant features of wild type (WT) HSV-1 and the deletion of both copies of the ICP34.5 gene in the R3616 mutant virus. HSV-1 genome consists of two covalently joined segments, L (long) and S (short), each comprising a unique region (U) flanked by a set of terminal and inverted repeats (TR and IR). Bottom panels show the PCR amplification products for ICP34.5 and thymidine kinase (TK) sequences from viral nucleic acids preparations and analyzed by electrophoresis. Std, size standards in kilobases (kb).

E) Expression of ISGs measured by RT-qPCR analysis in organoids infected with HSV-1 wild type or R3616 (10^2 PFU) at 8 dpi. Data are mean ± SEM (n=3; p>0.9999 *IFIT2*; p=0.7 *ISG15*; p=0.1 *OAS1*; Mann-Whitney test).

dpi, days post-infection; ns, non-significant.

SUPPLEMENTAL ITEMS

Table S1. Summary of TORCH infection experiments in early-stage organoids (related to Figure 1, S1 and 7)

TORCH agent (strain)	Family (subfamily)	Genome	Genome size (kb)	Target cell	Dose	Replication	Organoid growth phenotype
ZIKV (French Polynesian)	Flaviviridae	ssRNA(+)	10.7	hNPC	10^5 $TCID_{50}$	efficient	attenuated
HCMV (TB40/E)	Herpesviridae (Betaherpesvirinae)	dsDNA	235	hNPC	10^5 PFU	inefficient	none
					5×10^5 PFU	inefficient	none
HSV-1 (F)	Herpesviridae (Alphaherpesvirinae)	dsDNA	152	hNPC	10^4 PFU	efficient	severely attenuated
					10^3 PFU	efficient	severely attenuated
					10^2 PFU	efficient	attenuated
HSV-1 R3616 (F)	Herpesviridae (Alphaherpesvirinae)	dsDNA	152	hNPC	10^3 PFU	efficient	attenuated
					10^2 PFU	inefficient	very mildly attenuated

Table S2. Summary of organoids used in various experiments (related to Figure 1, S1, S2, 5, S5, 6, 7 and S7)

Figure	Experiment	No. viral particles per organoid	No. organoid batches (experiments)	Total no. organoids
1B	ZIKV infection	10^5 $TCID_{50}$ units	5	n=35 MOCK 4 dpi n=32 ZIKV 4 dpi n=42 MOCK 8 dpi n=28 ZIKV 8 dpi n=46 MOCK 12 dpi n=51 ZIKV 12 dpi
S1H	HCMV	10^5 PFU	3	n=16 MOCK 12 dpi n=18 HCMV 12 dpi
S1H	HCMV	5×10^5 PFU	1	n=6 MOCK 12 dpi n=5 HCMV 12 dpi
S1M	HSV-1 infection	10^4 PFU	2	n=9 MOCK 4 dpi n=10 HSV-1 4 dpi n=13 MOCK 8 dpi n=14 HSV 8 dpi
S1M	HSV-1 infection	10^3 PFU	2	n=29 MOCK 4 dpi n=37 HSV-1 4 dpi n=25 MOCK 8 dpi n=32 HSV-1 8 dpi
1I	HSV-1 infection	10^2 PFU	3	n=58 MOCK 4 dpi n=74 HSV-1 4 dpi n=72 MOCK 8 dpi n=87 HSV-1 8 dpi
S2G	HSV-1 infection (day 40)	6×10^2 PFU	5	n=52 MOCK 4 dpi n=51 HSV-1 4 dpi n=40 MOCK 8 dpi n=35 HSV-1 8 dpi n=40 MOCK 12 dpi n=33 HSV-1 12 dpi
5C	IFN-I treatment against ZIKV	10^5 $TCID_{50}$ units	3	n=26 MOCK 12 dpi n=22 ZIKV 12 dpi n=29 ZIKV+IFNα2 12 dpi n=25 ZIKV+IFNβ 12 dpi
S5F	IFN-I treatment	none	5	n=49 untreated n=50 IFNα2 n=50 IFNβ
6C	IFN-I treatment against HSV-1	10^2 PFU	3	n=72 MOCK 8 dpi n=87 HSV-1 8 dpi n=54 HSV-1+IFNα2 8 dpi n=68 HSV-1+IFNβ 8 dpi
7K	IFN-I treatment against HSV-1 R3616	10^2 PFU	1	n=17 MOCK 8 dpi n=22 R3616 8 dpi n=11 R3616+IFNα2 8 dpi n=11 R3616+IFNβ 8 dpi
S7B	IFN-I pre and post treatment against HSV-1 WT	10^2 PFU	5	n=97 MOCK 8 dpi n=107 HSV-1 8 dpi n=40 HSV-1+postIFNα2 8 dpi n=44 HSV-1+preIFNα2 8 dpi n=37 HSV-1+postIFNβ 8 dpi n=41 HSV-1+preIFNβ 8 dpi

Table S3. Differential gene expression in infected versus MOCK organoids (related to Figure 2 and S2)

A-B) Differentially expressed genes (DEGs) in ZIKV-exposed versus MOCK-exposed organoids at 12 days post-infection (dpi, A) and in HSV-1-exposed versus MOCK-exposed organoids at 8 dpi (B).

Table S4. Primer sequences used for RT-qPCR (related to STAR Methods)

Target and sequences	SOURCE	IDENTIFIER
Primers TBP: forward 5->3 GGGCACCACTCCACTGTATC reverse 5->3 CGAAGTGCAATGGTCTTTAGG	This study	N/A
Primers IFNA: Forward 5->3 CGATGGCCTCGCCCTTTGCTTTA Reverse 5->3 GGGTCTCAGGGAGATCACAGCCC	(Paijo et al., 2016)	N/A
Primers IFNB1: Forward 5->3 TGTGGCAATTGAATGGGAGGCTTGA Reverse 5->3 TCAATGCGGCGTCCTCCTTCTG	(Paijo et al., 2016)	N/A
Primers ISG15: Forward 5->3 TGTCGGTGTCAGAGCTGAAG Reverse 5->3 AGAGGTTCGTCGCATTTGTC	This study	N/A
Primers IFIT2: Forward 5->3 CAGCTGAGAATTGCACTGCAA Reverse 5->3 CGTAGGCTGCTCTCCAAGGA	This study	N/A
Primers OAS1: Forward 5->3 TGACTGGCGGCTATAAACC Reverse 5->3 TGGGCTGTGTTGAAATGTGT	This study	N/A
Primers RIG-I: Forward 5->3 AGTGAGCATGCACGAATGAA Reverse 5->3 GGGATCCCTGGAAACACTTT	(Hamel et al., 2015)	N/A
Primers IFIH1: Forward 5->3 GCCATTGCAGATGCAACCAG Reverse 5->3 TTGCGATTTCCTTCTTTTGCAG	(Hamel et al., 2015)	N/A
Primers DHX58: Forward 5->3 GCCCTCGGGGTATCATCTTC Reverse 5->3 CCCGGATGTCCACAGTCTG	Primer Bank	149408121c3
Primers TLR3: Forward 5->3 TTGCCTTGTATCTACTTTTGGGG Reverse 5->3 TCAACACTGTTATGTTTGTGGGT	Primer Bank	19718735c1
Primers TLR7: Forward 5->3 TCCTTGGGGCTAGATGGTTTC Reverse 5->3 TCCACGATCACATGGTTCTTTG	Primer Bank	67944638c1
Primers cGAS: Forward 5->3 CCCAAGCATGCAAAGGAAGG Reverse 5->3 ACAATCTTTCCTGCAACATTTCT	(Paijo et al., 2016)	N/A
Primers STING: Forward 5->3 CACCTGTGTCCTGGAGTACG Reverse 5->3 CATCTGCAGGTTCCTGGTAGG	(Paijo et al., 2016)	N/A
Primers TK: Forward 5->3 ACCCGCTTAACAGCGTCAACA Reverse 5->3 CCAAAGAGGTGCGGGAGTTT	(Ferenczy and DeLuca, 2009)	N/A
Primers ACTIN: Forward 5->3 AAATCTGGCACCACACCTTC Reverse 5->3 AGAGGCGTACAGGGATAGCA	(Lancaster et al., 2013)	N/A
Primers SNAI1: Forward 5->3 TCGGAAGCCTAACTACAGCGA Reverse 5->3 AGATGAGCATTGGCAGCGAG	Primer Bank	301336132c1
Primers MIXL1: Forward 5->3 GGCGTCAGAGTGGGAAATCC Reverse 5->3 GGCAGGCAGTTCACATCTACC	Primer Bank	13994334c1
Primers LHX1: Forward 5->3 CCTGGACCGCTTTCTCTTGAA Reverse 5->3 ACCGAAACACCGGAAGAAGTC	Primer Bank	314122156c1
Primers ZIKV: ZIKA835 5->3 TTGGTCATGATACTGCTGATTGC ZIKA911c 5->3 CCTTCCACAAAGTCCCTATTGC	(Lanciotti et al., 2008)	N/A

Click here to access/download

Supplemental Videos and Spreadsheets

Table S3.xlsx